Migration and aggregation of ruthenium implanted in glassy carbon

BY

TASABEEH ALABID OSMAN JAFER

Submitted in partial fulfilment of the requirements for the degree of

DOCTOR OF PHILOSOPHY (PhD) IN PHYSICS

In the Faculty of Natural and Agricultural Sciences at University of Pretoria

December…….. 2023

Supervisor/Promoter: Prof J. B. Malherbe

Co- supervisor: Dr T. T. Thabethe

Co- supervisor: Dr. O. S. Odutemowo

UNIVERSITEIT VAN PRETORIA
UNIVERSITY OF PRETORIA
YUNIBESITHI YA PRETORIA

DECLARATION

I, Tasabeeh Alabid Osman Jafer, declare that the dissertation, which I hereby submit for the degree of PhD in University of Pretoria, is my own work and has not been submitted by me for a degree at this or any other tertiary institution.

Signature: ……

Date: ……

SUMMARY

Migration and aggregation of ruthenium implanted in glassy carbon

BY

Tasabeeh Alabid Osman Jafer

Submitted in partial fulfillment of the requirements for the degree of (PhD) in Physics in the Faculty of Natural and Agricultural Science, University of Pretoria

Supervisor/Promoter: Prof. J. B. Malherbe

Co- supervisor: Dr. T. T. Thabethe

Co- supervisor: Dr. O. S. Odutemowo

Glassy carbon is a continuous, isotropic and non-graphitizing carbon that combines the properties of glass and ceramic with those of graphite. It has excellent properties such as high tensile strength, high hardness, good thermal and electrical conductivity, and combined resistance to high temperatures, wear, and corrosion. Glassy carbon is also highly impermeable to gases and liquids. These outstanding properties of glassy carbon make it a good choice for nuclear applications.

Glassy carbon has been proposed as a containment material for radioactive fission products. For glassy carbon to be considered a suitable candidate for fission products containment, it must be an effective diffusion barrier for fission products, such as ruthenium (Ru), and its microstructure should not change dramatically under ion bombardment and extreme heat conditions.

In this study, 150 keV Ru ions were implanted into glassy carbon at room temperature and 200 ˚C to a fluence of 1×10^{16} cm^{-2}. The as-implanted samples were annealed at two temperature regimes (from 500 to 1000 °C and from 1000 to 1300 °C – in steps of 100 °C) for 5 h under vacuum. This study investigates the structural modifications and surface characteristics of glassy carbon under the influence of Ru ion implantation and subsequent heat treatment. Ru migration in glassy carbon was also investigated. Moreover, several techniques, including Raman spectroscopy, X-ray diffraction (XRD), atomic force microscopy (AFM), and scanning electron microscopy (SEM), have been used to examine the microstructure and

surface topography of glassy carbon before and after ion implantation and heat treatment. Moreover, secondary ion mass spectrometry (SIMS) and Rutherford backscattering spectrometry (RBS) were used to study Ru migration in glassy carbon.

Raman spectroscopy was utilized to monitor the structural variations in glassy carbon resulting from Ru implantation and heat treatment. The study involved analyzing the Raman spectra through baseline correction, fitting with Gaussian and Breit-Wigner-Fano functions, and deriving key parameters such as peak intensity, FWHM (full width at half maximum), and peak position. Variations in these parameters were used to assess glassy carbon structures, especially defects, crystal size, and residual stress. The study identified that the D and G bands in the Raman spectrum, associated with disordered sp^3 bonds and sp^2 vibrations of graphite, provided insights into the presence of graphitic crystallites in glassy carbon. Furthermore, it was observed that Ru implantation led to the merging of D and G peaks into a single broadband. This indicates the amorphization of graphitic crystallites in glassy carbon. However, a broader G peak was present in the Raman spectrum of the as-implanted samples at room temperature compared to those implanted at 200 °C which indicated that the magnitude of radiation damage in the room temperature implanted sample is more than in the 200 °C implanted sample.

Annealing at 500 °C resulted in initiated partial recrystallization, while higher annealing temperatures of 600 to 1300 °C led to enhanced recovery of the glassy carbon structure. However, even after annealing at 1300 °C, the glassy carbon structure did not fully return to its virgin state, indicating the persistence of some damage introduced by Ru ion implantation.

The positions of the G peaks were found to shift after implantation, and the nature of this shift was attributed to stress. Tensile stress was associated with shifts to lower wavenumbers, while shifts to higher wavenumbers indicated compressive stress. The study showed that Ru implantation induced tensile stress in glassy carbon, while annealing reduced tensile stress. However, at temperatures above 900 °C, compressive stress was introduced, consistent with findings from previous studies which correlated residual stress to glassy carbon density. As confirmed by Raman measurements, XRD analysis of glassy carbon samples revealed an increase in tensile strain following Ru implantation, while annealing at temperatures over 900 °C resulted in an increase in compressive strain.

RBS and SIMS were used to monitor the migration behaviour of Ru in glassy carbon after annealing at both low and high temperatures. Annealing the as-implanted samples at

temperatures ranging from 500 to 1300 °C had distinct effects on the Ru depth profiles. Annealing from 500 to 800 °C showed no significant change in the Ru depth profiles, indicating the non-diffusivity of Ru in glassy carbon at these lower temperatures. However, annealing at temperatures above 900 °C led to noticeable changes in the depth profiles. These changes included an increase in the maximum depth profile peak, a shift towards the surface, and a decrease in the FWHM. These changes suggested Ru aggregation at these higher temperatures, forming nanoparticles within the glassy carbon. In addition, more Ru aggregation was observed in room temperature implanted samples compared to those implanted at 200 °C. This discrepancy could be attributed to the higher concentration of defects in room temperature implanted samples, which may promote Ru aggregation and cluster formation. It aligns with the idea that impurity clusters are more likely to form in regions with high defect concentrations.

The aggregation of Ru was accompanied by a shift of depth profiles towards the glassy carbon surface. This shift was attributed to a stress field that resulted in the migration of the profiles as a whole. The Raman and XRD results indicated the introduction of high levels of stress in the implanted region due to Ru implantation and annealing, which contributed to the observed depth profile shift. Moreover, the Ru peak shift toward the surface was lower in the room temperature implanted samples than in the 200 °C implanted samples. This was due to increased Ru aggregation within the room temperature implanted samples. This caused Ru clusters to grow larger, causing Ru to migrate more slowly toward the surface compared to the 200 °C implanted samples which showed less Ru aggregation. In addition to that, the high concentration of defects in the room temperature implanted sample played a role in trapping the majority of the Ru atoms in the high radiation damage region which restricted its migration towards the surface. Importantly, annealing at both low and high temperatures did not result in a noticeable loss of the Ru implanted in glassy carbon. This was likely due to Ru aggregation forming clusters inside the glassy carbon, preventing Ru out-surface diffusion. In light of this, the glassy carbon material may serve as an effective container for Ru fission product.

The study conducted SEM and AFM analyses to assess surface changes in glassy carbon substrates following Ru implantation and heat treatment. After Ru implantation, surface roughness decreased substantially, with the R_q (root mean square roughness) values dropping from 1.45±0.05 nm for virgin glassy carbon to 0.40±0.05 nm for room temperature implanted samples and 0.37±0.05 nm for 200 °C implanted samples. This decrease was attributed to Ru

bombardment. However, annealing at 1000 °C led to a significant increase in R_q values, reaching 1.10±0.12 nm for 200 °C implanted samples and 1.15±0.12 nm for room temperature implanted samples. This increase was primarily due to the aggregation of Ru atoms, possibly forming Ru nanoparticles near the surface. Subsequent annealing at temperatures between 1100 °C and 1200 °C reduced R_q surface roughness for room temperature implanted samples. This decrease was attributed to the surface diffusion of substrate atoms, causing them to shift from the peaks to valley positions on the sputter-roughened surface. Consequently, the initial polishing marks became less pronounced. No change in R_q surface roughness was observed for 200 °C implanted samples after annealing at 1100 °C and 1200 °C, potentially due to a shift in the depth profile toward the surface. Annealing at 1300 °C resulted in an increase in R_q surface roughness, with values reaching 2.25±0.27 nm for room temperature implanted samples and 2.75±0.27 nm for 200 °C implanted samples. This increase was linked to the formation of large carbon island clusters on the surface.

In summary, Ru implantation and heat treatment significantly influenced glassy carbon substrate R_q surface roughness. The observed variation in response to annealing at higher temperatures could be attributed to Ru migration, cluster formation, and substrate atom diffusion.

Acknowledgements

I would like to express my sincere gratitude to the following individuals and institutions for their unwavering support and invaluable contributions to the successful completion of my study:

- Professor J. B. Malherbe, my academic supervisor, and my co-supervisors, Dr. T. T. Thabethe and Dr. O. S. Odutemowo, for their exceptional guidance, unwavering support, and insightful discussions throughout the course of my research.
- Professor C. C. Theron, the head of the Physics department, for granting me the opportunity to work within the department of Physics.
- Professors Thulani Hlatshwayo and Dr. Eric Njoroge, along with Mr. J. Smith, for their invaluable assistance with the accelerator, which significantly contributed to the success of my study.
- My friends within the Physics department, with special recognition to my colleagues in the Nuclear Materials Research Group, particularly Dr. Hesham Abdelbagi and Dr. Zaki Abdalla, for their camaraderie and support.
- To my beloved husband, who is the king of my heart, I extend my deepest appreciation for his boundless love, patience, unwavering support, constant encouragement, and heartfelt prayers.
- My parents, siblings, and family members, whose unwavering support during my academic journey and in life has been an endless source of strength and motivation.
- I am grateful for the financial assistance provided by the OWSD, and I acknowledge their support. It is important to note that the opinions expressed, and conclusions drawn in this work are solely those of the author and do not necessarily reflect the views of the OWSD.

LIST OF ABBREVIATIONS.

AFM – Atomic Force Microscopy
BSE – Backscattered Electrons
CCD - Charged Coupled Devices
CFE - Cold Field Emitter
EBSD - Electron Backscatter Diffraction
EDS – Energy dispersive X-rays spectroscopy
FESEM- Field Emission Scanning Electron Microscope
FPs - Fission Products
FWHM- Full Width at Half Maximum
GC – Glassy Carbon
He – Helium
HLW - High level nuclear wastes.
ILW - Intermediate level nuclear wastes.
keV – Kilo Electron Volt
LLW - Low-level nuclear wastes.
MCA - Multi-channel analyser
RBS- Rutherford Backscattering spectrometry
Ru – Ruthenium
SE - Secondary Electrons
SEM - Scanning electron microscopy
SIMS- Secondary Ions Mass Spectroscopy.
SRIM - Stopping and Range of Ions in Matter
XRD- X-ray Diffraction
UP – University of Pretoria

TABLE OF CONTENTS

TABLE OF FIGURES.

LIST OF TABLES.

CHAPTER 1
INTRODUCTION

Over the past few decades, the increased reliance on fossil fuels for electricity production has resulted in a significant rise in greenhouse gas emissions, exacerbating the issue of global climate change. To combat this problem, both the Kyoto Protocol and the Paris Agreement have strongly recommended a shift towards alternative methods of power generation that emit fewer greenhouse gases. Among these alternatives, nuclear power has emerged as a viable solution due to its low carbon footprint, accounting for approximately 17% of the world's total electrical energy.

In light of the growing concerns about greenhouse gases and carbon footprints, an increasing number of countries are considering the expansion of nuclear power as an attractive alternative. However, there exists a significant hurdle in public perception. Nuclear power is often viewed negatively by the general public, primarily due to fears surrounding potential high-level radioactive nuclear waste leakage into the environment during reactor accidents like those witnessed at Three Mile Island, Chernobyl, and Fukushima. It is worth noting that radioactive waste is generated not only by nuclear facilities but also through sealed radioactive sources in various industries, as well as human-made radionuclides in hospitals and laboratories. Nonetheless, the three primary sources of radioactive waste are nuclear fuel cycle activities, nuclear power plant operations, and nuclear research activities.

The radioactive waste generated from these activities varies considerably in terms of its physical, chemical, and radiological characteristics. Therefore, it becomes crucial to manage radioactive waste effectively to safeguard both human health and the environment, while also minimizing future burdens associated with such waste. By implementing sound waste management practices, we can ensure that radioactive waste is handled in a manner that minimizes potential risks and maximizes the protection of human health and the environment.

1.1 Ruthenium as radioactive waste

In nuclear reactors, neutrons play a crucial role in inducing the fission of heavy elements such as uranium and plutonium, leading to the release of energy. A heavy and light fission product is produced after each fission, with masses of 140 (+/- 15) u, and 95 (+/- 15) u,

respectively [Cea08, Reu12]. As an example, the fission of plutonium-239 produces tin-134, ruthenium-103, and three free neutrons that can cause further fission reactions:

$$^{239}_{94}Pu + ^{1}_{0}n \rightarrow ^{103}_{44}Ru + ^{134}_{50}Sn + 3^{1}_{0}n \quad (1)$$

In nuclear fuel, numerous different elements can be formed due to variations in the mass of fission products. Figure 1.1 shows all the possible elements (fission products) formed by nuclear fission. Several factors determine the abundance of each individual fission product, including the fissile nucleus and the impacting neutron's energy [Reu12]. Several factors determine the abundance of each individual fission product, including the fissile nucleus and the impacting neutron's energy [Reu12]. The higher the neutron impact energy, the smaller the difference between the heavy and light fission product. This leads to an increase in the abundance of fission products with masses between 105 and 125 u, as shown in Figure 1.2 (a). Moreover, when compared to uranium-235, plutonium-239 and -241 produce more fission products with masses between 100 and 110 u, as shown in Figure 1.2 (b).

It is known that spent nuclear fuel can contain radioactive forms of the platinum group metal ruthenium since it is a fission product. Ruthenium isotopes found in spent nuclear fuel have masses between 100 and 110 u. Table 1.1 shows all stable and radioactive ruthenium isotopes found in spent nuclear fuel or in nature.

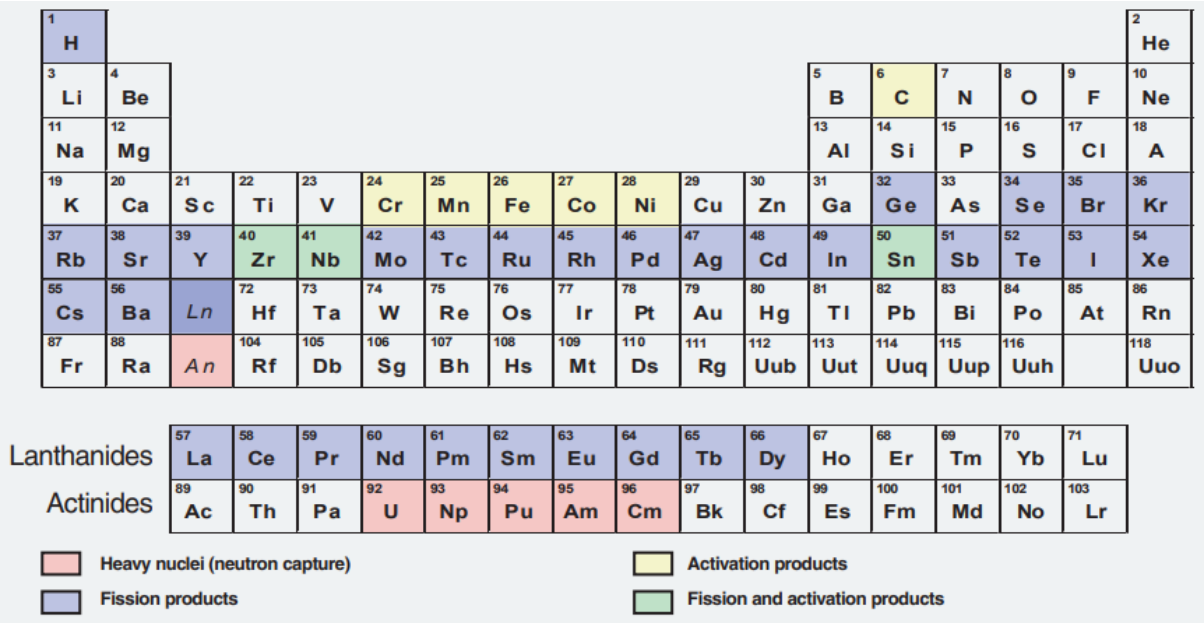

Figure 1.1: *Different groups of elements (shown in different colours), including elements that can be formed in a nuclear fission reactor [Cea08].*

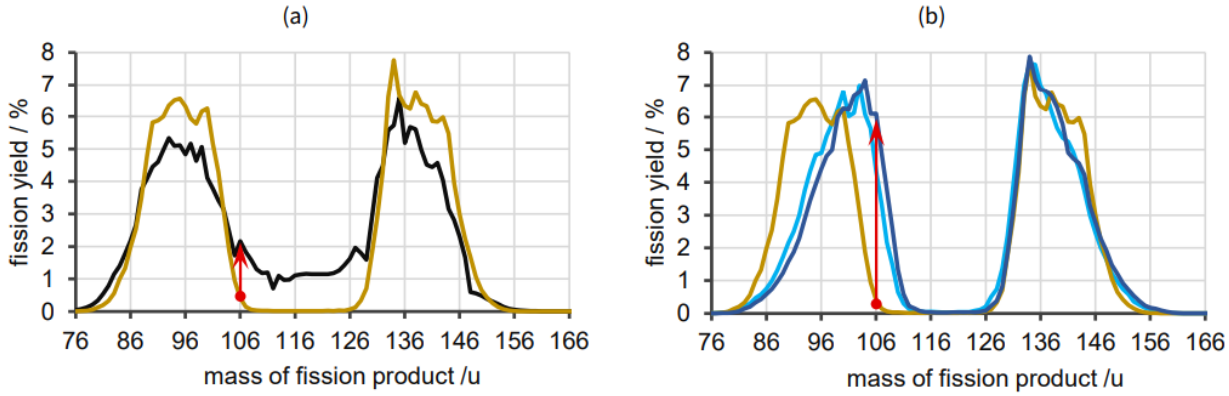

Figure 1.2: *(a) The yield of fission products from uranium-235 with thermal neutrons at 25 meV (yellow) compared to fast neutrons at 14 MeV (black), (b) using thermal neutrons at 25 meV, the fission product yields for uranium-235, plutonium-239, and plutonium-241 are shown in yellow, light blue and blue, respectively [Www1]. A red arrow indicates the relative amount of ruthenium-106 fission products and isobar fission products.*

Table 1.1: *Radioactive and stable Ruthenium isotopes [Mag15].*

Isotope	*^{96}Ru*	*^{97}Ru*	*^{98}Ru*	*^{99}Ru*	*^{100}Ru*	*^{101}Ru*	*^{102}Ru*	*^{103}Ru*	*^{104}Ru*	*^{105}Ru*	*^{106}Ru*	*^{107}Ru*
Natural abundance /%	*5.5*	-	*1.9*	*12.7*	*12.7*	*17.0*	*35.5*	-	*18.8*	-	-	-
Half-life	-	*3 d*	-	-	-	-	-	*39 d*	-	*4.5 d*	*374 d*	*4 min*

Considering Table 1.1 and Figure 1.2, all stable ruthenium isotopes fall within the mass range of the light fission products (between 80 and 105 u). Moreover, ruthenium is one of the main fission products in uranium oxide (UOX) and mixed oxide (MOX) fuels used in thermal and fast reactors. However, in a similar burnup, MOX fuels contain more ruthenium (compared to UOX fuel) due to a higher number of plutonium fissions and a faster neutron spectrum [Reu12, Car00]. Most ruthenium radioisotopes have half-lives shorter than a week (see Table 1.1), so after a few weeks, such isotopes do not contribute significantly to the radioactive inventory of spent fuel. However, some ruthenium radioactive isotopes, such as ruthenium-103 and ruthenium-106, can contribute to spent fuel radiation levels for several years, as shown in

Figure 1.3. Only a very small fraction of ruthenium-103 ($T_{1/2} \approx 39$ days) remains in the spent fuel after it has been reprocessed for five years (i.e., 5 years after discharged from the reactor). This small fraction of ruthenium-103 contributes slightly to the total γ-activity of the spent fuel [Cea08]. On the other hand, a larger fraction of ruthenium-106 ($T_{1/2} \approx 374$ d) remains more pronounced and contributes significantly to the total γ-activity. Moreover, due to the fact that uranium-235 fission does not produce high yields of ruthenium-106, spent UOX fuel has an acceptable level of γ-activity [Cea08]. In contrast, ruthenium-106 is formed more frequently by the fission of plutonium-239 and -241, as shown with the red arrow in Figure 1.2 (b). Consequently, MOX fuels contain a higher ruthenium-106 concentration due to higher fission yields. The presence of high concentrations of ruthenium-106 in spent fuel causes higher γ-activities, and this is difficult to manage in the process of treatment and recycling of spent nuclear fuel.

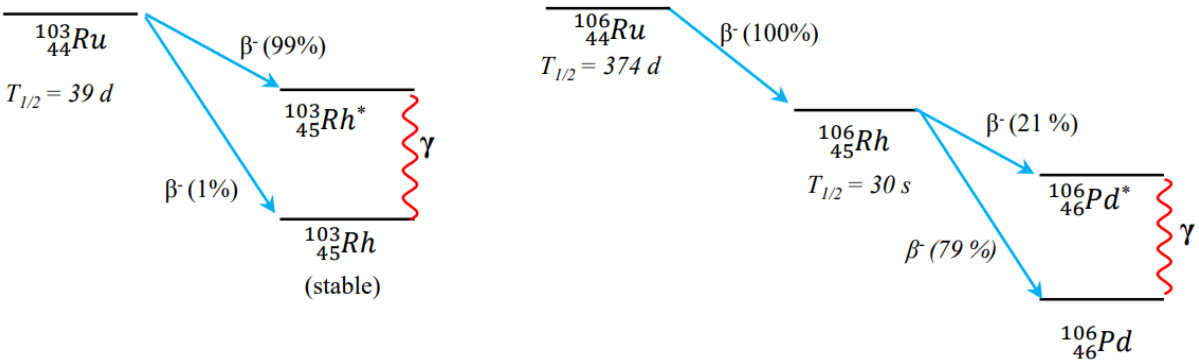

Figure 1.3: *Schematic diagram of the decay of ruthenium-103 and –106 [Www1].*

1.2 Classification of nuclear wastes

Nuclear waste is categorized into three distinct levels according to its activity level and the half-life of its radioactive elements. These levels are commonly referred to as low-level, intermediate-level, and high-level nuclear waste. For more comprehensive information regarding the various levels of nuclear waste, please refer to Sections 1.2.1, 1.2.2, and 1.2.3 of the sources [Rah06] [Www3].

1.2.1 Low-level nuclear wastes (LLW)

Low-level nuclear waste primarily originates from the nuclear industry, along with a limited amount produced by medical facilities and research laboratories. To store low-level waste, a viable option is utilizing a sewage system, while solid waste can be transported to a landfill or an incineration plant, as long as the activity remains below nuclide-specific limits, determined by annual limit on intake values. During interim storage, waste packages are securely stored within concrete containers, each with a volume of 5 m^3. In the majority of cases, low-level radioactive waste is promptly disposed of through land-based disposal methods after being appropriately packaged to ensure long-term management.

1.2.2 Intermediate level nuclear wastes (ILW)

ILW typically arises from various sources, including nuclear power plants, research institutions, and medical facilities.

Due to the higher radioactivity levels, ILW necessitates more stringent handling, storage, and disposal measures. Commonly, ILW is packaged in robust containers, such as stainless steel drums or concrete casks, to ensure containment and prevent leakage or dispersion of radioactive materials.

1.2.3 High level nuclear wastes (HLW)

Spent nuclear fuel, which is removed from nuclear power plants after being utilized for power generation, is considered high-level waste. This category also includes highly radioactive waste resulting from the reprocessing of spent fuel. Some nuclear wastes within spent fuel experience rapid decay in radioactivity due to their short half-lives, such as iodine-131, which has a half-life of 8 days. However, a majority of the nuclear wastes found in spent fuel possess long half-lives, such as plutonium-239 and plutonium-240, which have half-lives of 24,000 and 6,800 years, respectively.

Given the lengthy half-lives of these radioactive elements, it is imperative to store spent fuel in specially designed waste containers. Failure to do so can lead to health issues like cancer,

elevated environmental temperatures, and increased radiation exposure resulting from high-level nuclear waste.

To mitigate these risks, appropriate waste storage containers are crucial. They ensure the safe containment and isolation of high-level nuclear waste. These containers are specifically engineered to prevent leakage, dispersion, and any potential interaction with the environment or living organisms.

The potential health hazards associated with high-level waste necessitate stringent protocols and safety measures throughout its handling, storage, and disposal. Proper management and long-term storage of high-level nuclear waste are essential to safeguard human health, protect the environment, and mitigate the risks posed by radioactivity.

1.3 Storage of nuclear wastes

High-level nuclear waste should be stored segregated so it can be retrieved later for further treatment or transferred to an alternative storage facility or disposed of. Moreover, waste isolation reduces exposure risks and limits reactor accident consequences. There are a number of reasons why storing radioactive waste for varying periods of time is appropriate, including [Iae06]:

- Allowing short-lived radionuclides to decay so that radioactive wastes can be released, discharged, or recycled.
- A sufficient amount of radioactive waste should be collected and accumulated before being transferred to another facility for treatment and conditioning.
- Collection and accumulation of radioactive waste prior to disposal.
- The rate of heat generation from high-level radioactive wastes must be reduced prior to disposal and, in some cases, during predisposal management.
- Providing long-term storage of nuclear waste in areas without suitable disposal facilities.

1.3.1 The wastes storage method

The two main methods of storing nuclear waste are the wet storage and the dry storage method [Nrc02] [Nrc13]. These two methods are discussed below.

1.3.1.1 Wet storage method

Most spent nuclear fuel is currently reprocessed at individual nuclear reactor sites and segregated in special pools designed specifically for this purpose. Figure 1.4 (a) illustrates the wet storage method of storing spent fuel in rods under water at least 20 feet deep. This provides adequate radiation shielding near the pool site. Most pools were typically designed to store spent fuel for several years. Moreover, most pools were designed to accommodate a large number of spent fuel rods due to delays in developing disposal facilities.

1.3.1.2 Dry storage method

A dry storage system is one of the alternative options for storing spent nuclear fuel when pool capacity fills up. This method involves the use of an inert gas that surrounds spent fuel within a container, also known as a cask (see Figure 1.4 (b)). Various metals are used to manufacture casks, including stainless steel, iron, copper, titanium alloys, and nickel-based alloys or concrete. The use of some of these casks is not limited to long-term storage but can also be used during nuclear waste transport. Dry storage is the most common method of storing spent fuel in nuclear power plants.

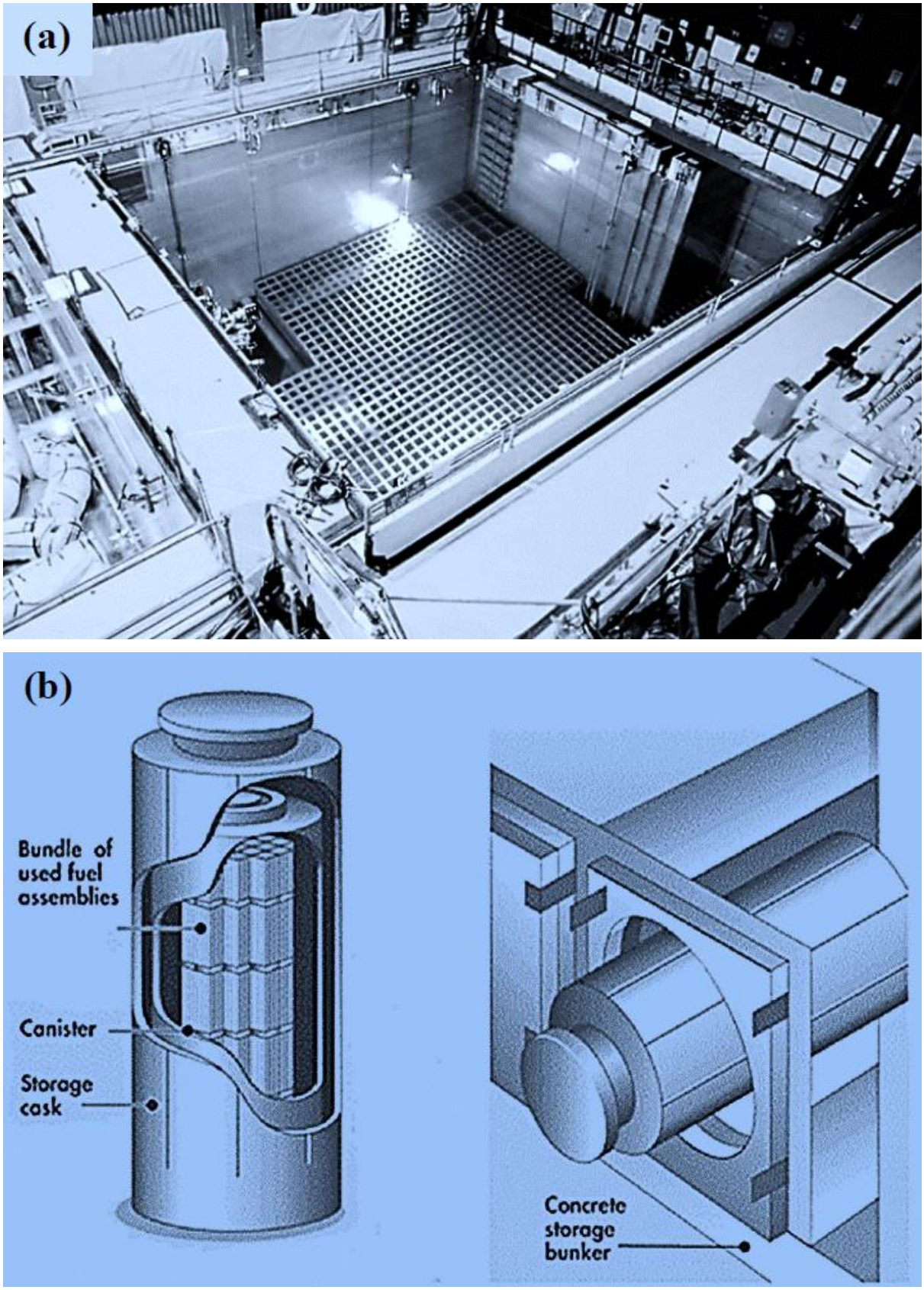

Figure 1.4: *A configuration for storing spent fuel waste in two methods: (a) Wet storage and (b) Dry storage [Www3, Nrc13].*

1.4 Research Motivation

Storing radioactive waste in a manner that safeguards both human health and the environment, both presently and in the future, is crucial. During the entire waste management process, the performance of the materials used in nuclear waste storage is crucial. Thus, the development of highly durable waste containers (including the cask and surrounding container barriers) is critical to ensuring the long-term stability of materials and the isolation of radioactive waste. A wide variety of metal materials are commonly used to fabricate casks, including copper, iron, stainless steels, titanium alloys, and nickel-based alloys. In addition to these materials, certain ceramics and graphite may also be considered for cask fabrication [Yim00]. While copper is one of the few metals that have good environmental durability, it has poor performance in brine and radiation environments [Hal21]. Compared to other materials, iron steel has high predictability due to the extensive knowledge available about its properties and behavior. Despite its lack of corrosion resistance, iron steel is less prone to catastrophic failures. Although titanium alloys are mechanically strong and corrosion resistant, they can experience brittle failure with the uptake of hydrogen. As with titanium, nickel-based alloys, such as Incoloy and Hastelloy, resist corrosion well. Nickel-based alloys are easier to weld than titanium, but they are more expensive. Although stainless steels possess good mechanical properties and are very corrosion resistant, they can fail catastrophically through stress-corrosion cracking in addition to being very expensive [Yim00]. Graphite and silicon carbide, which are ceramic materials, are corrosion-resistant and more abundant than other materials, but graphite lacks mechanical strength [Zha13], while silicon carbide loses its integrity when exposed gaseous fission products [Mts23, Mok23]. Glassy carbon has high corrosion resistance, high mechanical strength, and impermeable to gases. Because of these properties, glassy carbon has been proposed as a containment material for radioactive fission products. The applicability of glassy carbon as a diffusion barrier against some radioactive fission products (Sr, Ag, Se, Xe) has been studied [Ade20, Ism18, Odu20]. However, the migration behaviour of a significant fission product, such as Ru, in glassy carbon has not been thoroughly investigated. ^{106}Ru (half-life of 373.59 days) is the most stable isotope of ruthenium and it is an important fission product of nuclear fuel or reprocessed nuclear fuel [Mas19]. It can also be obtained by the nuclear transmutation of Technetium-99 (99Tc) [Kon99]. Ruthenium fission product is very toxic, and it causes cancer.

1.5 Research objective

In this study, the major objective is to investigate the feasibility of using glassy carbon to build nuclear waste storage casks. For this purpose, one of the significant fission products, namely Ru ions, was implanted into glassy carbon. The main problem with dry nuclear storage is that the casks degrade over time due to heat. Another legacy problem in nuclear storage is that nuclear waste can diffuse out of nuclear containers. As a result, the glassy carbon was annealed at various temperatures to determine whether it retained its thermal resistance and the ability to retain Ru fission product. Moreover, glassy carbon has outstanding properties such as low reactivity and gas impermeability due to its unique structure (discussed in detail in chapter 2), therefore, it's imperative to retain its structure after ion bombardment and heat treatment. In this study, using Raman spectroscopy and X-ray diffraction (XRD), the structure of glassy carbon was studied after ion bombardment (with Ru ions) and heat treatment at different temperatures. In addition to investigating the migration behaviour of Ru ions in glassy carbon, changes in the surface morphology and roughness of glassy carbon were also investigated in this study.

1.6 The outlay of the thesis

This thesis consists of nine chapters and is organized as follows:

Chapter 1 serves as the introduction and provides a comprehensive overview of nuclear power, nuclear waste, and various methods of nuclear waste storage.

Chapter 2 delves into the discussion of carbon materials and their allotropes, including an exploration of their structures, properties, and applications.

Chapter 3 focuses on the general concept of ion implantation, offering insights into its principles and applications.

Chapter 4 centers around diffusion and diffusion theory, presenting a detailed examination of these phenomena and their significance in the context of the study.

In Chapter 5, several analytical techniques employed during the research are discussed, including Rutherford backscattering spectrometry (RBS), X-ray diffraction (XRD), and Raman spectroscopy.

Chapter 6 describes the experimental procedures and outlines the annealing processes undertaken during the study.

Chapter 7 presents the results and facilitates a comprehensive discussion of the findings.

Chapter 8 encompasses the conclusions drawn from the results obtained and provides recommendations for future research endeavors.

Lastly, Chapter 9 showcases the research outputs, presenting them in a detailed manner.

By following this structured framework, the thesis aims to provide a comprehensive and organized presentation of the research and its findings.

References

[Ade20] S.A. Adeojo, J.B. Malherbe, E.G. Njoroge, M. Mlambo, O.S. Odutemowo, T.T. Thabethe, Z.A.Y. Abdalla, T.T. Hlatshwayo, *Effect of sequential isochronal annealing on the structure and migration behaviour of selenium-ion implanted in glassy carbon*, Vacuum 182 (2020) 109689.

[Cea08] *Nuclear Energy Division Monograph, treatment and recycling of spent nuclear fuel*. Paris: CEA, 2008.

[Car00] V. Carron, *Etude du mecanisme d'oxydation des formes dissoutes du ruthénium dans les solutions d'acide nitrique-application a l'elimination du ruthenium des solutions de dissolution des combustibles nucléaires irradies*, PhD thesis, Grenoble 1, 2000.

[Giu07] G. Giuliani, A. De Bono, S. Kluser, P. Peduzzi, *Environment Alert Bulletin*, UNEP, Europe, 2007.

[Hal21] D.S Hall, M. Behazin, W.J. Binns, P.G. Keech, *An evaluation of corrosion processes affecting copper-coated nuclear waste containers in a deep geological repository*, Progress in Materials Science. 118 (2021) 100766.

[Iae06] IAEA, *safety standards: Storage of radioactive waste*, Vienna, 2006.

[Iae06'] IAEA, *Development of Specifications for Radioactive Waste Packages*, Vienna, 2006.

[Ism18] M.Y.A. Ismail, J.B. Malherbe, O.S. Odutemowo, E.G. Njoroge, T.T. Hlatshwayo, M. Mlambo, E. Wendler, *Investigating the effect of heat treatment on the diffusion behaviour of xenon implanted in glassy carbon*, Vacuum 149 (2018) 74–78.

[Kon99] R.J.M. Konings, R. Conrad, Transmutation of technetium - results of the EFTTRA-T2 experiment, J. Nucl. Mater. 274 (1999) 336–340.

[Mag15] J. Magill, Karlsruher Nuklidkarte, Nuclear Data Chart, 2015.

[Mal18] J.B. Malherbe, O.S. Odutemowo, E.G. Njoroge, D.F. Langa, T.T. Hlatshwayo, C.C. Theron, *Ion bombardment of glassy carbon*, Vacuum 149 (2018) 19 – 22.

[Mas19] O. Masson, G. Steinhauser, D. Zok, O. Saunier, H. Angelov, D. Babić, V. Bečková, J. Bieringer, M. Bruggeman, C.I. Burbidge, S. Conil, A. Dalheimer, L.E. De Geer, A. De Vismes Ott, K. Eleftheriadis, S. Estier, H. Fischer, M.G. Garavaglia, C. Gasco Leonarte, K. Gorzkiewicz, D. Hainz, I. Hoffman, M. Hýža, K. Isajenko, T. Karhunen, J. Kastlander, C. Katzlberger, R. Kierepko, G.J. Knetsch, J. Kövendiné Kónyi, M. Lecomte, J.W. Mietelski, P. Min, B. Møller, S.P. Nielsen, J. Nikolic, L. Nikolovska, I. Penev, B. Petrinec, P.P. Povinec, R. Querfeld, O. Raimondi, D. Ransby, W. Ringer, O. Romanenko, R. Rusconi, P.R.J. Saey, V. Samsonov, B. Šilobritiene, E. Simion, C. Söderström, M. Šoštarić, T. Steinkopff, P. Steinmann, I. Sýkora, L. Tabachnyi, D. Todorovic, E. Tomankiewicz, J. Tschiersch, R. Tsibranski, M. Tzortzis, K. Ungar, A. Vidic, A. Weller, H. Wershofen, P. Zagyvai, T. Zalewska, D. Zapata García, B. Zorko, Airborne concentrations and chemical considerations of radioactive ruthenium from an undeclared major nuclear release in 2017, Proc. Natl. Acad. Sci. U. S. A. 116 (2019) 16750–16759.

[Mts23] S.Z. Mtsi, A. Sohatsky, Z.A.Y. Abdalla, E.G. Njoroge, V.A. Skuratov, S.V. Motloung, J.B. Malherbe, T.T. Hlatshwayo, Effects of helium (He) bubbles and annealing on the structural evolution and migration behavior of silver (Ag) implanted into polycrystalline SiC at 350° C, Vacuum. 218 (2023) 112621.

[Mok23] T. Mokgadi, Z. Abdalla, H. Abdelbagi, M. Msimanga, C. Maepa, V. Skuratov, T. Hlatshwayo, Helium and strontium co-implantation into SiC at room temperature and isochronal annealing: Structural evolution of SiC and migration behaviour of strontium, Materials Chemistry and Physics. 294 (2023) 126998.

[Nrc02] US Nuclear regulatory commission, *Radioactive Waste: Production, Storage, Disposal*, NRC, Washington, DC, 2002.

[Nrc13] U.S. Nuclear Regulatory Commission, *Dry Cask Storage of Spent Nuclear Fuel*, NRC, USA, 2013.

[Odu20] O.S. Odutemowo, M.S. Dhlamini, E. Wendler, D.F. Langa, M.Y.A. Ismail, J.B. Malherbe, *Effect of heat treatment on the migration behaviour of Sr and Ag CO-implanted in glassy carbon*, Vacuum 171 (2020) 109027.

[Rah06] T. Rahola, M. Markkanen, *Storage of low-level radioactive waste and regulatory control of sealed sources in Finland*, STUK - Radiation and Nuclear Safety Authority, Finland, 2006.

[Reu12] P. Reuss. *Neutron Physics*, 1st ed. Les Ulis Cedex A, France: EDP sciences, 2012.

[Wer92] L. Werme, P. Sellin, N. Kjellbert, *Copper canisters for nuclear high level waste disposal. Corrosion aspects*, Swedish Nuclear Fuel and Waste Management Co., 1992.

[Www1] Evaluated Nuclear Data File, Rosfond Database, Nuclear Fission Yield. Ed. by V. Zerkin. 2010. URL: https://www-nds.iaea.org/exfor/endf.htm (visited on 26/08/2020).

[Www2] Evaluated Nuclear Data File. 2018. URL: https://www-nds.iaea.org/exfor/endf.htm (visited on 19/03/2018).

[Www3] Radioactive waste management, Thematic series, IRSN, France, 2013. URL: www.irsn.fr (visited on 26/11/2021).

[Yim00] M. Yim, K.L. Murty, *Materials issues in nuclear waste management*, Journal of the Minerals, Metals & Materials Society 52 (2000) 26 – 29.

[Zha13] Y. Zhao, J. Shi, H. Wang, Z. Tao, Z. Liu, Q. Guo, L. Liu, *A sandwich structure graphite block with excellent thermal and mechanical properties reinforced by in-situ grown carbon nanotubes*, Carbon. 51 (2013) 427-430.

CHAPTER 2
THE CARBON MATERIAL AND ITS ALLOTROPES

Carbon is readily found in nature. It consists of six electrons and is represented by the symbol C (i.e., ^{12}C). Carbon also consists of a wide range of allotropes [Hir10], but only allotropes of carbon found in nature namely such as amorphous carbon, diamond and graphite. All carbon atoms have four valence electrons, which allows them to easily bond with one another to form long chains or rings [Fal07].

The structure of carbon materials varies due to the three types of bonding, also known as hybridization. These three types of hybrid bonding in carbon are depicted in Figure 2.1: sp^1 (linear coordination), sp^2 (triangular coordination), and sp^3 (tetrahedral coordination). Diamond exhibits a pure sp^3 hybridization, graphite has a pure sp^2 hybridization, while amorphous carbon has an sp^2 hybridization with a certain fraction of sp^3 hybridization [Miy98].

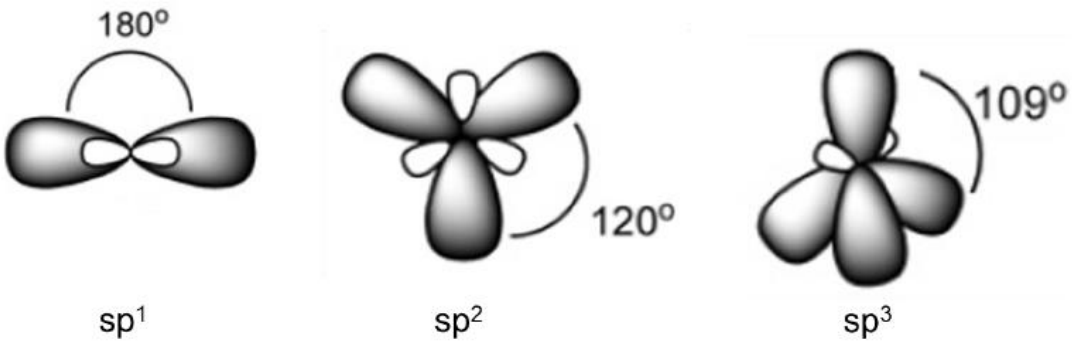

Figure 2.1: *Hybridization types and hybrid orbitals [Kru10].*

Two of the four hybrid orbitals in the sp^1 configuration bond together and form an angle of 180°, resulting in a linear molecule – see Figure 2.1 [Kru10]. Therefore, alpha (σ) bonds form along the *x*-axis of the sp^1 bond, with the remaining two electrons entering the Pi (π) orbitals on the *y*- and the *z*-axis, respectively.

Three of the four hybrid orbitals are combined together in a sp^2 configuration (one s orbital and two p orbitals), creating a trigonal sp^2 orbital with the neighbouring atoms at 120°, similar to graphite structure (see Figure 2.1) [Pie93]. In the $p\pi$ orbital, the free valence electron (*pz*) lies perpendicular to the sp^2 hybrid orbitals. In the sp^2 configuration, a weak bond can form between carbon atoms. This is due to the fact that the π orbital forms a weak bond with a π

orbital on one or more neighbouring atoms [Ans06]. Just like in the diamond structure, the four hybrid orbitals are tetrahedrally oriented toward the sp^3 orbital, which forms a strong σ-bond to an adjacent angle [Lin11], as shown in the sp^3 configuration in Figure 2.1.

2.1 Carbon's allotropes

Carbon allotropes are classified in two forms, natural (i.e., amorphous carbon, diamond, and graphite) and artificial (fullerenes and nanotubes and carbynes), as shown in Figure 2.2.

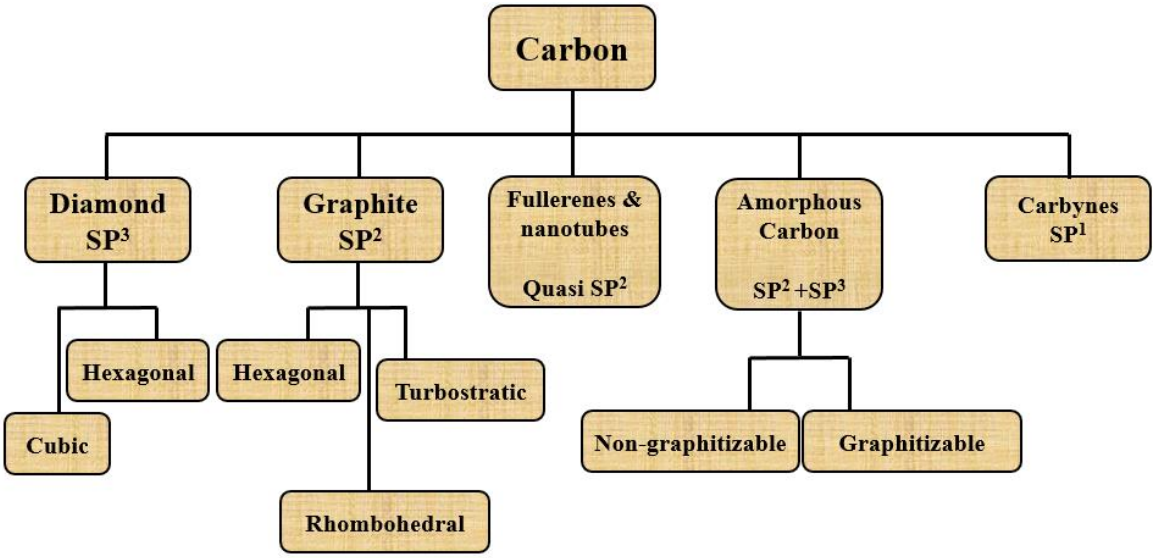

Figure 2.2: *An illustration of the different forms of carbon found in nature and in artificial products.*

2.1.1 Graphite

In graphite, there are nearly infinite graphene layers, spaced parallel to each other. Moreover, due to sp^2 hybridization (in graphene), each carbon atom bonds to three others to form a planar hexagon. These graphene sheets (planar hexagons) are bonded by Van der Waals bonds to form a graphite crystal, which can be hexagonal, rhombohedral, or turbostratic. The hexagonal graphite structure is created by stacking ABAB, which is the most common graphite form – see Figure 2.3. However, rhombohedral graphite, created by stacking ABCABC, is an uncommon form of graphite. The rhombohedral graphite structure can be transformed into a hexagonal structure once heated above 1300 °C. Turbostratic graphite has a disordered structure. It has been demonstrated that graphene layers are often rotated randomly within turbostratic structures, which results in stacking faults [Kru10, Fal07, Pie93, Pau66, Li07]. Figure 2.3 shows the hexagonal, rhombohedral and turbostratic structures of graphite.

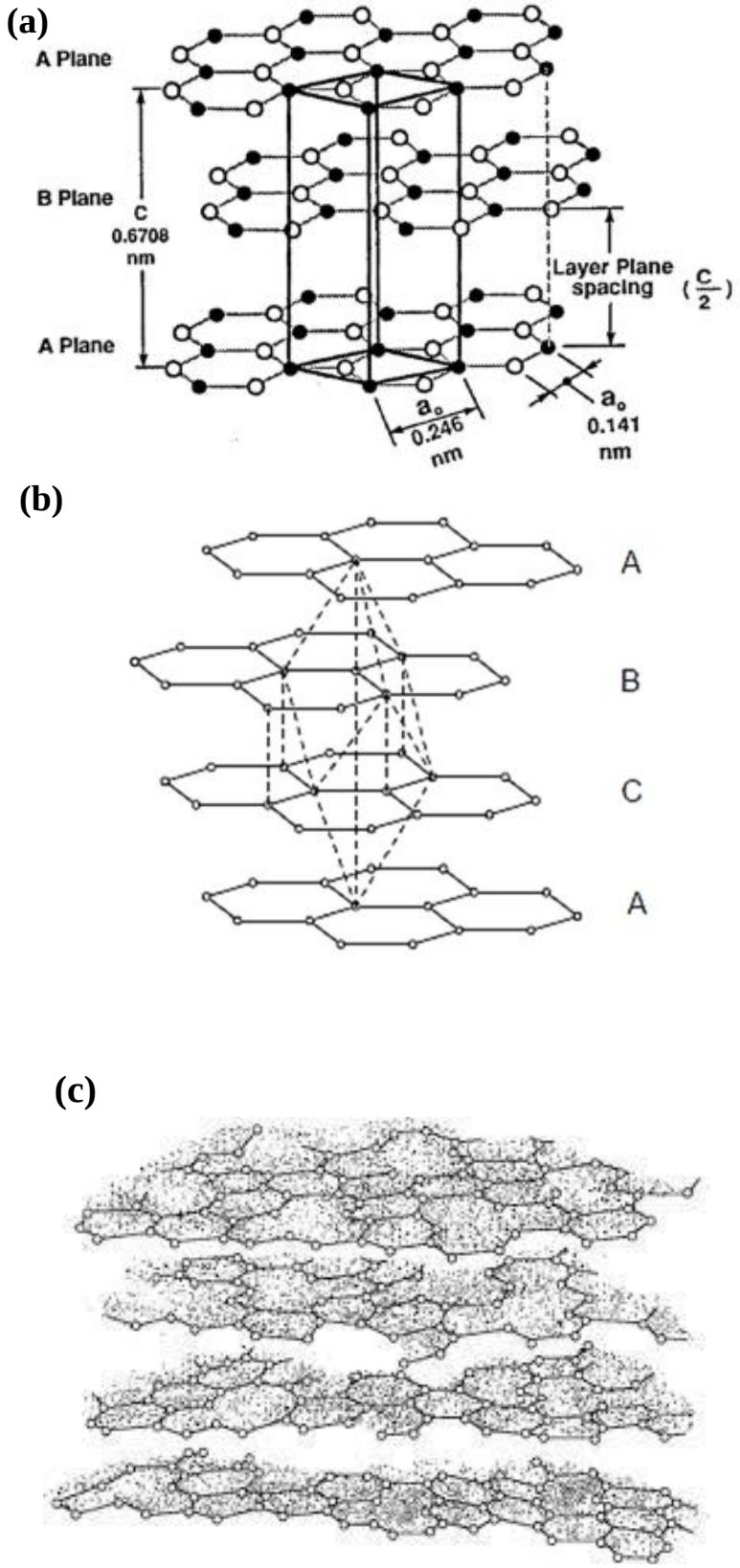

Figure 2.3: *A schematic illustration of the structure of different types of graphite showing the stacking sequences of (a) hexagonal, (b) rhombohedral, and (c) turbostratic [Pie93, Zha17].*

2.1.1.1 Properties of graphite

The Van der Waals force between graphene layers and the arrangement of carbon atoms within the layers determine graphite properties. (i.e., the layered structure) [Fal07]. The rhombohedral graphite structure exhibits less stability than the hexagonal structure. Therefore, when rhombohedral graphite is heated or treated with acids, its layers shift into a two-sequence layer [Pau66]. The properties of GC are tabulated table 2.1 below.

Table 2.1. *A summary of graphite's physical properties.*

Property	**Value**
The form of crystals	hexagonal and rhombohedral
Hexagonal lattice parameters	a_0 = 0.246 nm c_0 = 0.671 nm
Colour	Black
Atomic number density	1.14×10^{23}
Density (in 1 atm and at room temperature)	2.26 g/cm^3
Atomic volume	5.315 cm^3/mol
Compression strength	0.065-0.089 GPa
Melting point (in 100 atm)	4200 K
Boiling point	4560 K
Sublimation point	4000 K
Carbon-carbon bond distance	0.1421 nm
Heat of vaporization to monoatomic gas	716.9 kJ/mol
Thermal conductivity at 23 °C	Pyrolytic graphite: ab directions 190-398 W/m.°C

	c direction 1-3 W/m.°C
Pauling electronegativity	2.5
Magnetic susceptibility	0.141×10^{-6} cm^3/g
Specific heat capacity at 23 °C	0.690-0.719 kJ/kg.K
Binding energy	7.4 eV/C atom
Band gap	-0.04 eV

Aside from its low density, hexagonal graphite has a low friction coefficient, high chemical stability (at room temperature), low thermal expansion coefficient, and high thermal and electrical reactivity [Pie93].

2.1.1.2 Graphite applications:

Graphite is a versatile material with a wide range of allotrope properties, which has led to its extensive use in various applications [Pie93, Ter10]. Some of these applications are listed below:

- Graphite nanoribbons are commonly used in chemical and biosensors due to their low capacitance.
- Graphite is an effective filler material in developing robust polymer composites.
- Hexagonal graphite, owing to its excellent conductivity, is used in developing highly conducting transparent films and thermally conductive polymers.
- Graphite is a popular choice for use as electrodes in Li-ion batteries, owing to its ability to embed both positive and negative ions electromechanically.

Graphite nanoribbons are employed in various chemical processes, including catalytic reactions, assembling heavy metal filters, and drug delivery.

2.1.2 Diamond

In terms of hardness, diamonds are one of the hardest solid materials (with a value of 10 on the Mohs hardness scale). They can have a cubic or hexagonal structure (lonsdaleite). However, diamonds with hexagonal shapes are rare in nature. A cubic diamond is formed by ABCABC stacking, whereas a hexagonal diamond is formed by ABAB stacking, as shown in Figure 2.4. Interconversion between these two forms of diamond is possible only under special circumstances. Moreover, each carbon atom in these two forms has sp^3 hybridization which allows it to bond strongly with four neighbours of another carbon atom. As a result, it forms a tetrahedral network (see Figure 2.5) [Kru10, Fal07]. This gives the diamond a three-dimensional shape.

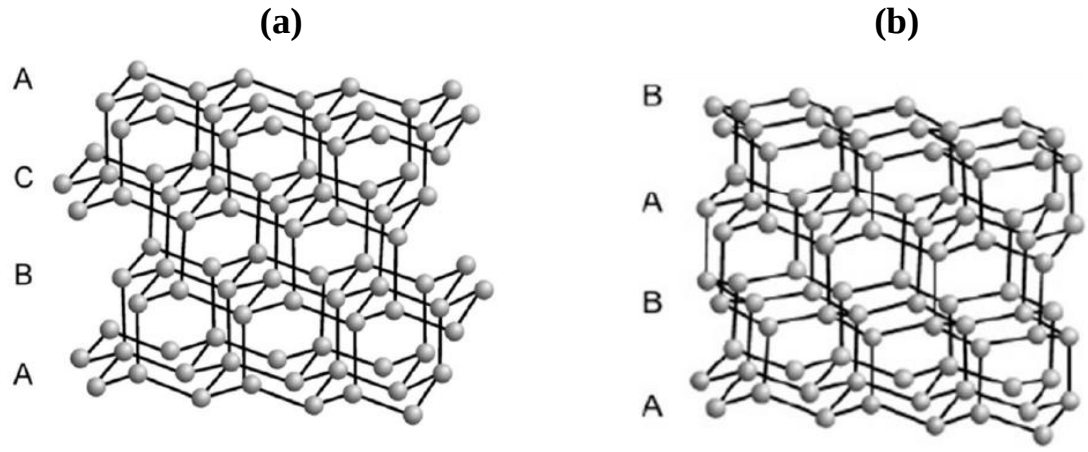

Figure 2.4: *Diamond structures (a) hexagonal and (b) cubic. Taken from [Kru10].*

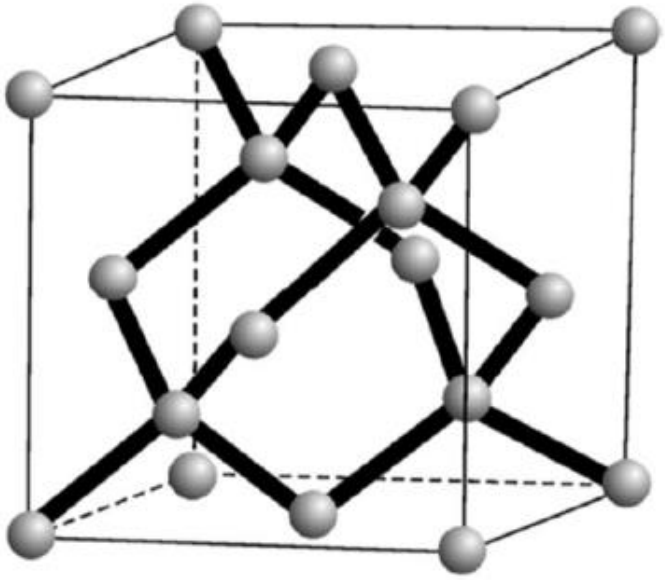

Figure 2.5: *Diamond lattice structure with sp^3 covalent bonding. Taken from [Miy98].*

Under certain conditions, diamonds can be thermodynamically transformed into graphite. The conditions for this transformation include high temperatures (above 1500 °C), low pressure, and a specific atmosphere (such as a vacuum or inert gas atmosphere). However, hexagonal and cubic diamonds can be formed from graphite at very high temperatures (500°C - 1700°C) and high pressures (more than 15 GPa) [Fal07, Pie93, Niu12].

2.1.2.1 Diamond properties

In terms of material stability, diamond (lonsdaleite) in both hexagonal and cubic structural forms is extremely stable. Moreover, due to sp^3 hybridization, each carbon atom in diamond is bonded to four neighbouring carbon atoms, resulting in high hardness and high thermal conductivity. In addition to being an excellent electrical insulator, diamond can also be used as a wide bandgap semiconductor when doped with nitrogen, boron, etc. [Kru10]. Additionally, it is highly resistant to neutron radiation. It also has a high refraction index which enables it to be used in a wide variety of industries [Pie93]. Below is a list of some of the physical properties of diamond [Kru10, Miy98, Ume10, Zhu11].

Table 2.2. *Diamonds' physical properties*

Property	**Value**
The form of crystals	Cubic and hexagonal
Density	3.52 g/cm^3 (Both structures have the same theoretical density) [Bun67]
Lattice constants: A. In face-central cubic (fcc) structure B. In hexagonal structure	A. 356.68 pm B. a_0 = 252 pm, and c_0 = 412 pm
Band gap	about 5.5 eV
Bond length (C-C)	154.45 pm
In a hexagonal structure, the interplanar distance is	205 pm

At room temperature, the coefficient of thermal expansion is	1.06×10^{-6} °C^{-1}
The thermal conductivity at room temperature is	2000 W/m.K
Compressing strength	8.68-16.53 GPa
Hardness	5700-10400 kg/mm^2 or 10 Mohs
Resistivity	higher than 10^{18} Ω.m
Friction coefficient A. In vacuum B. In air	A. about 1 B. 0.05-0.1

2.1.2.2 Diamond applications

Diamond possesses remarkable properties that make it a highly valuable material in various technological applications. Some of these applications are listed below:

- Diamond is an excellent heat sink for semiconductor lasers, owing to its high carrier mobility and exceptional thermal conductivity. This property is also crucial for high-power transistors [Bar14, Har04].
- Due to its exceptional hardness and thermodynamic stability, diamond is a suitable material for abrasive devices and tribological applications [Fal07, Miy98].
- Diamond's chemical and thermal inertness, as well as its transparency, make it an ideal material for protective coatings on electronic, biomedical, optical, mechanical, and aerospace components [Lin11].
- Owing to its hardness and chemical stability, diamond finds extensive use in applications such as cutting and grinding tools, oil drilling bits, and ceramic polishing.

2.1.3 Fullerene

In 1985, Smalley and Kroto [Sma85] observed clusters of carbon atoms in the molecular range of C_{30}-C_{100}, which led to the discovery of fullerene. It is theoretically possible to build

fullerene structures with hundreds of carbon atoms. However, to date, only five fullerene structures have been identified, namely C_{60}, C_{70}, C_{76}, C_{78}, and C_{84} (see Figure 2.6). In the C_{60} molecule, sixty carbon atoms are arranged in twenty hexagons and twelve pentagons. C_{60} molecule has the shape of a soccer ball, whereas C_{70} molecule has the shape of a rugby ball. Moreover, C_{70} has a red-orange colour in solution. The C atoms in C_{76} molecules are arranged in pentagon and hexagon shapes – see Figure 2.6. The colour of C_{70} in solution is green-yellow, while C_{78} is golden-yellow and chestnut brown, and C_{84} is olive-green.

The fullerene molecule does not only contain one type of crystalline structure (like diamond or graphite, which have cubic, hexagonal, and rhombohedral crystals), but a cage-like spheroid form with pentagons and hexagons interconnected. Unlike graphite, sigma (σ) orbitals in fullerene do not completely cover all pi (π) orbitals and s-orbitals, as well as not belonging entirely to p-orbitals. This leads to fullerene hybridization being unstable, unlike diamond and graphite hybridizations, which are sp^3 and sp^2, respectively. However, the only factor that influences hybridization in fullerene is the number of carbon atoms in the molecule. Among all known carbon phases, fullerene is the only one capable of converting into diamond at room temperature. This transformation can be achieved by compressing the C_{60} powder at more than 150 atm in less than a second.

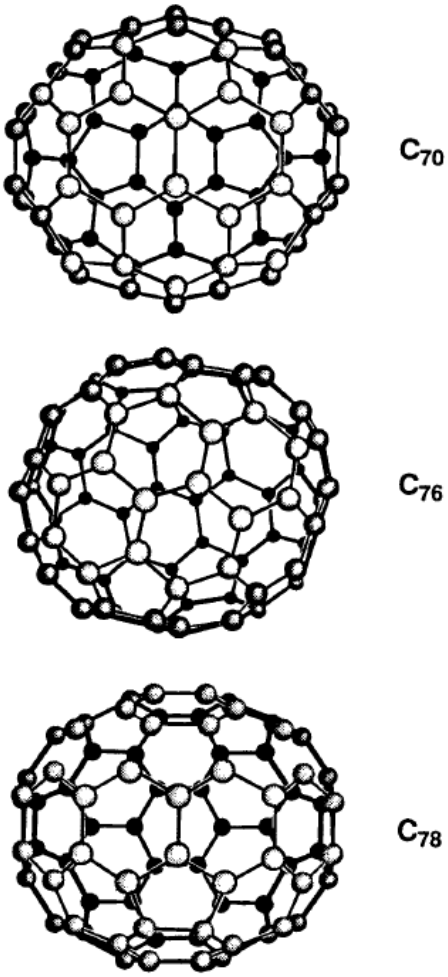

Figure 2.6: *Molecular schematics of some fullerenes. Taken from [Pie93].*

Carbon nanotubes with single walls are also known as fullerene. Single-walled carbon nanotubes or fullerene are formed when the dangling bonds of carbon atoms are connected together at the end (edge) of each finite layer of graphene. Carbon nanotubes and fullerenes both contain six carbon rings connected by their pentagonal structure. Moreover, carbon onions (rings) are also a form of fullerenes. However, among these fullerene molecules, C_{60} is the most stable, famous, aromatic, dominant, and most symmetric. A typical fullerene (C_{60}) molecule is shown in Figure 2.7 [Fal07, Ter00, Sat06].

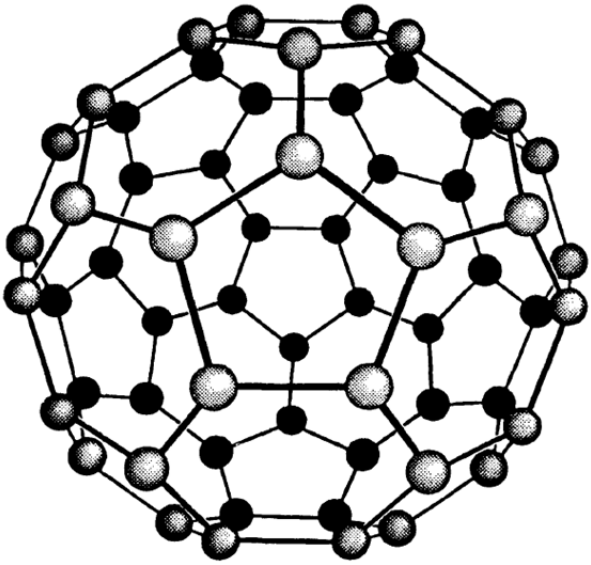

Figure 2.7: *Molecular structure of C_{60} fullerene. Taken from [Pie93].*

2.1.3.1 Fullerene properties and its applications

The softest solid state of carbon is C_{60} aggregates. However, at high pressure, they could become harder than diamonds if compressed to 70% of their original volume. Physically, C_{60} aggregates are stable, but chemically, they can be very reactive to free radicals [Pie93]. Based on its interesting physical properties [Fal07], C_{60} has recently been investigated for biological and solar cell applications. Moreover, due to its solubility in water, fullerene has pharmacological effects on body cells, organs, nucleic acids and enzymes. Since it was discovered in 1985 [Sat06], it has also been used in biomedicine due to its pharmacological properties.

2.1.4 Glassy carbon

The discovery of glassy (vitreous) carbon material took place in the early 1960s [Har04]. Glassy carbon is a form of non-graphitized carbon that exhibits ribbon-like and tangled graphitic crystallites/microstructures [Jen71]. This material is obtained by high-temperature carbonization of a polymeric precursor. According to Noda [Nod64] and Furukawa [Fur64], the glassy carbon structure comprises both graphite and tetrahedral parts, as illustrated in Figure 2.8.

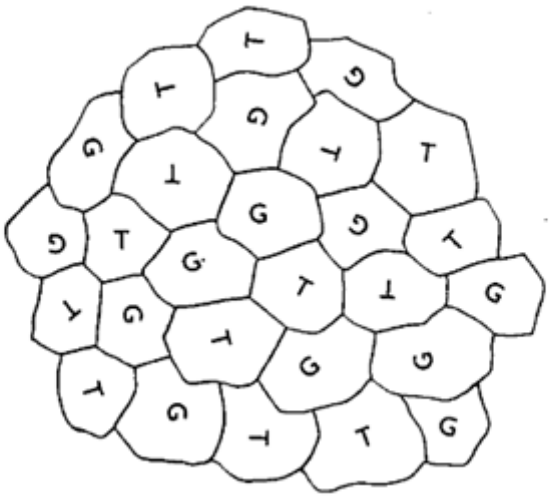

Figure 2.8: *A model of the microstructure of glassy carbon developed by Noda, Inagaki, and Furukawa. Taken from [Nod64, Fur64].*

Jenkins and Kawamura [Jen71] proposed a different model for glassy carbon, as shown in Figure 2.9. A controlled, slow transformation of certain polymers at temperatures between 900 and 1000 ˚C was used to manufacture glassy carbon [Jen71]. Microfibers and twisted graphite ribbons were the basis for Jenkins and Kawamura's model (i.e., consisting of very narrow microfibers and twisted ribbon-like graphite). Although this model was widely accepted, it was imperfect. This is because the micropore structure of this model may allow some gases to permeate. This contrasts with the fact that glassy carbon is highly impermeable to gases [Har05, Har04].

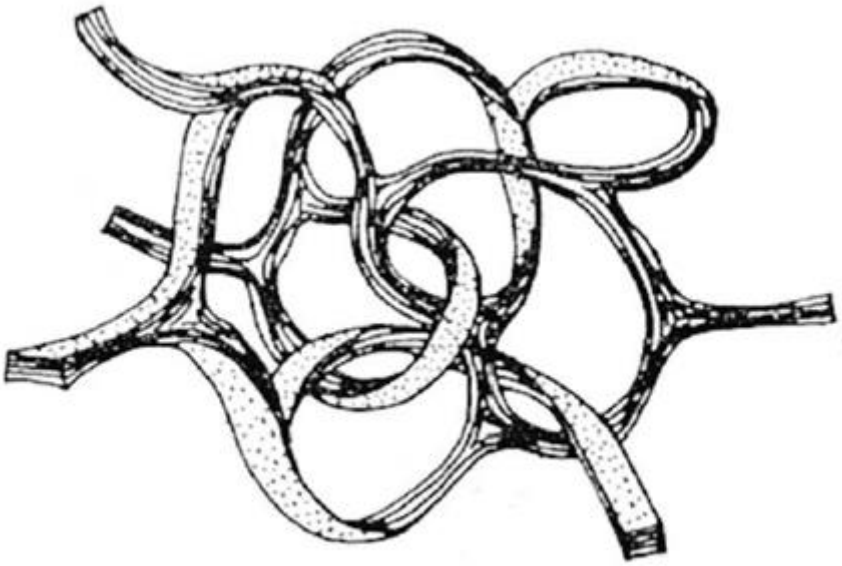

Figure 2.9: *A model of the microstructure of glassy carbon proposed by Jenkins and Kawamura. Taken from [Jen 71].*

Sigradur is a glass-like carbon form, frequently used for chemical and physical experiments because of its excellent texture, non-wettability, and low impurity levels [Www2]. Other properties of Sigradur glassy carbon are summarized in Table 2.3. Sigradur glassy carbon can be manufactured in two different types, namely Sigradur K and Sigradur G. The differences between them are related to the temperatures at which they are manufactured. Sigradur K glassy carbon is usually produced at lower temperatures (compared to Sigradur G), usually between 1000 and 1100 ˚C. It has a disordered microstructure composed of tightly curled carbon layers containing nanopores of 1 nm in size – see Figure 2.10 (a). However, Sigradur G glassy carbon needs a very high temperature, 3000 ˚C, to be produced. This type of Sigradur glassy carbon has large pores, about 5 nm in diameter - see Figure 2.10 (b). Graphitic walls and facets surround both types of Sigradur glassy carbon – as shown in Figure 2.10. Moreover, glassy carbon, like other non-graphitized carbons, has fullerene-related structures [Har04].

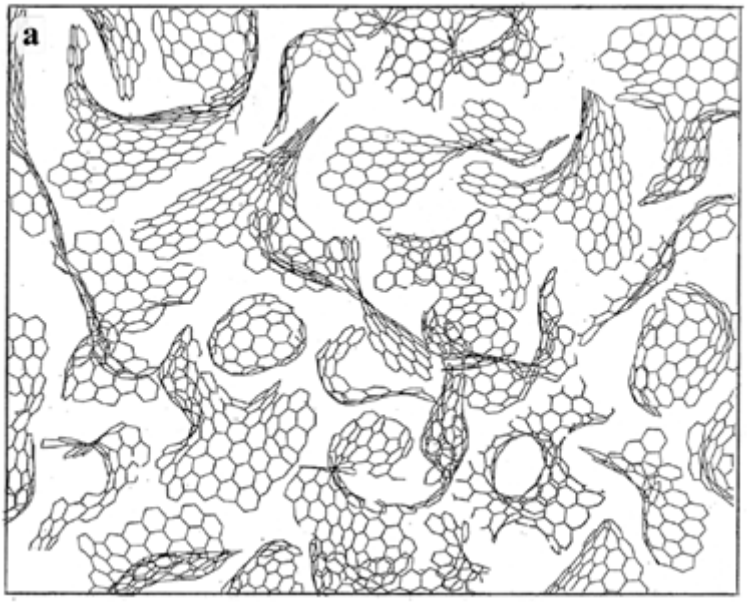

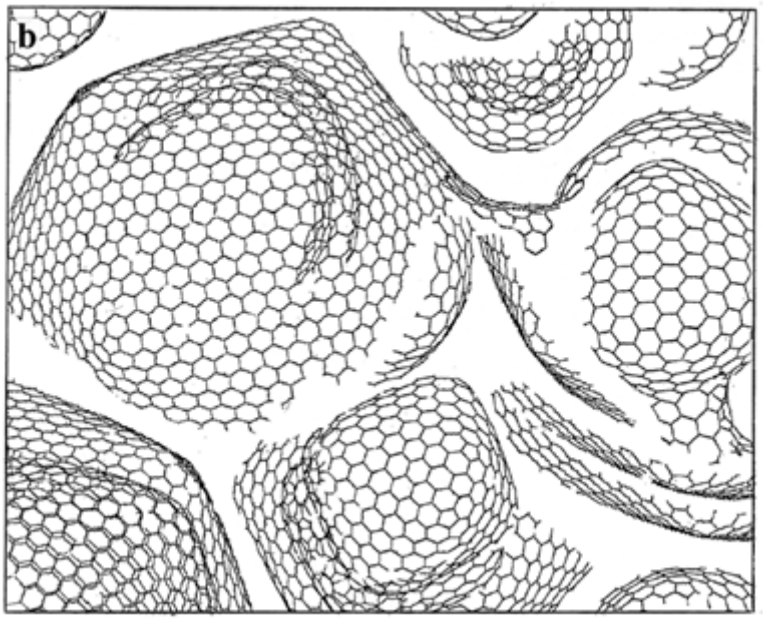

Figure 2.10: *The structural models of (a) Sigradur K and (b) Sigradur G. Taken from [Har04].*

With its high hardness and density, Sigradur K glassy carbon has more applications than Sigradur G glassy carbon. However, Sigradur G glassy carbon was used in this study because it offers better thermal resistance (~ 3000 C), high thermal conductivity, and better corrosion and erosion resistance compared to Sigradur K glassy carbon.

2.1.4.1 Properties of Sigradur glassy carbon

Glassy carbon is widely used in many technological applications because of its excellent properties. Table 2.3 lists some of the excellent glassy carbon properties [Pie93, Yam68].

Table 2.3. *Physical properties of glassy carbon*

Property	**Value**	
	Sigradur K	**Sigradur G**
Density	1.54 g/cm^3	1.42 g/cm^3
Hardness	120 Moh	70 Moh
Tensile strength	190 MPa	130 MPa

Compressive strength	580 MPa	480 MPa
Flexural strength	210 MPa	260 MPa
Gas permeability	10^{-12} cm^2/s	10^{-7} cm^2/s
In the range of 20 to 200°C, the thermal expansion coefficient is	3.5×10^{-6} K^{-1}	2.6 K^{-1}
Heat proof limit	Up to 1000 ˚C	Up to 3000 ˚C
Thermal conductivity	4.6 W/m.K	6.3 W/m.K
Spalling coefficient	21000 kcal/m.hr	17000 kcal/m.hr
Electrical resistivity	50×10^{-4} Ω.cm	35×10^{-4} Ω.cm
Energy gap	10^{-2} Ev	10^{-3} eV
Specific heat	5 kcal/kg.K	50 kcal/kg.K
Young's modulus of elasticity	35 GPa	35 GPa

Glassy carbon also has a smooth surface and relatively low electrical resistance, making it ideal for use as an electrode in microphones, electrodes for metal film production and lightning protectors for telephone circuits [Yam68]. Moreover, due to its low impurity content, glassy carbon might also be used in nuclear reactors. Our research group at the University of Pretoria has proposed using glassy carbon as a container material for nuclear waste. Due to its extraordinary properties, including chemical resistance, high thermal resistance, strength, hardness, and corrosion/erosion resistance, glassy carbon is an ideal material for use in nuclear storage casks [Pie93, Har04].

In nuclear reactors, glassy carbon can also be used as a diffusion barrier for a variety of reasons, such as having a low level of impurities and good ability to resist the passage of gases and liquids [Lin11] and, thus, it is an excellent diffusion barrier for gaseous fission products. Moreover, it is highly stable against alkaline earth halides like CaF_2, as well as highly resistant to thermal shock [Yam68].

Glassy carbon can exhibit improved wear resistance and better mechanical properties when implanted with ions at different concentrations [Iwa89, McC94]. As a result of the increase in density of glassy carbon after implantation, the researchers suggested that the material would be effective as an abrasive wear resistant material. In the next chapter, we will discuss ion implantation in more detail.

In the past few years, our research group at the University of Pretoria, South Africa, has published several papers regarding glassy carbon use in nuclear storage casks [Ade22, Jaf23, Hla17, Inn18, Ism18, Mal18, Odu18].

2.1.4.2 Applications of glassy carbon

Glassy carbon exhibits a variety of remarkable properties that are highly dependent on its processing conditions. Here are some notable properties and applications of glassy carbon:

- Glassy carbon has a high degree of chemical inertness, which makes it resistant to oxidation in dry air and water vapor. This property makes it a suitable material for applications in navy missiles and supersonic engines [Pie93].
- In addition to its chemical inertness, glassy carbon also exhibits excellent electrical conductivity, making it a highly effective electrode material for acid batteries [Pie93].
- Glassy carbon is highly resistant to acid attacks and can withstand exposure to sulfuric and nitric acids for several months without any effect. Its resistance to chromic and hydrofluoric acids makes it useful in electrochemistry as electrodes and crucibles [Pie93, Har04].
- Glassy carbon has been found to be compatible with a variety of materials, including chloride fused salts and alkali metals like Li, Na, and K. This property makes it a suitable material for nuclear reactor applications. Additionally, it is biocompatible, making it useful for prosthetic devices [Har04].
- Glassy carbon has a high melting point of around 4000 K, making it suitable for use in electronic devices, including minute heaters.
- In the mechanical field, glassy carbon exhibits high erosion resistance, making it useful for applications such as mandrels, rollers, and glass working equipment [Yam68].

References

[Ade22] S. Adeojo, J. Malherbe, A. Azarov, O. Odutemowo, E. Njoroge, H. Abdelbagi, S. Mpelane, T. Hlatshwayo, *Effects of implantation temperature and annealing on structural evolution and migration of Se into glassy carbon*, Solid State Sciences, 129 (2022) 106914.

[Ans06] E.V. Anslyn, D.A. Dougherty, *Modern physical organic chemistry*, University Science Books, 2006.

[Bar14] J. Barjon, F. Jomard, S. Morata, *Arsenic-bound excitations in diamond*, Physical Review B: Condensed Matter and Materials Physics, 89 (2014) 1–5.

[Fal07] E.H.L. Falcao, F. Wudl, *Carbon allotropes: beyond graphite and diamond*, Journal of Chemical Technology and Biotechnology, 82 (2007) 524 – 531.

[Fur64] K. Furukawa, *Nippon Kessho Gakkaishi (in Japanese)*, 1964.

[Har04] P.J.F. Harris, *Fullerene related structure of commercial glassy carbons*, Philosophical magazine, 84 (2004) 3159–3167.

[Har05] P.J.F. Harris, *New perspectives on the structure of graphitic carbons*, Critical reviews in solid state and materials sciences 30 (2005) 235–253.

[Hla17] T.T. Hlatshwayo, L.D. Sebitla, E.G. Njoroge, M. Mlambo, J.B. Malherbe, *Annealing effects on the migration of ion-implanted cadmium in glassy carbon*, Nucl. Instr. Methods. Phys. Res. B 395 (2017) 34–38.

[Hir10] A. Hirsch, *The era of carbon allotropes*, Nature Materials, 9 (2010) 868-871.

[Inn18] A.J. Innocent, T.T. Hlatshwayo, E.G. Njoroge, J.B. Malherbe, *Interface interaction of tungsten film deposited on glassy carbon under vacuum annealing*, Vacuum 148 (2018) 113–116.

[Ism18] M.Y.A. Ismail, J.B. Malherbe, O.S. Odutemowo, E.G. Njoroge, T.T. Hlatshwayo, M. Mlambo, E. Wendler, *Investigating the effect of heat treatment on the diffusion behaviour of xenon implanted in glassy carbon*, Vacuum 149 (2018) 74–78.

[Iwa89] M. Iwaki, K. Takahashi, K. Yoshida, Y. Okabe, *Improvement of wear properties of glassy carbon surface layer modified by ion implantations*, Nucl. Instr. Methods. Phys. Res. B 39 (1989) 700–703.

[Jaf23] T.A.O. Jafer, T.T. Thabethe, O.S. Odutemowo, S.A. Adeojo, H.A.A. Abdelbagi, A. Azarov, J.B. Malherbe, *Ruthenium ion modification of glassy carbon: Implication on the structural evolution and migration behaviour of implanted Ru atoms*, Nucl. Instr. Methods. Phys. Res. B 534 (2023) 72-80.

[Jen71] G. Jenkins, K. Kawamura, *Polymeric carbons-carbon fiber, glass and char*, Cambridge university press, 1971.

[Kru10] A. Krueger, *Carbon materials and nanotechnology*, John Wiley & Sons, 2010.

[Li07] Z. Q. Li, C. J. Lu, Z. P. Xia, Y. Zhou, Z. Luo, *X-ray diffraction patterns of graphite and turbostratic carbon*, Carbon, 45 (2007) 1686–1695.

[Lin11] Y. Lin, L. Zhang, H.K. Mao, P. Chow, Y. Xiao, M. Baldini, J. Shu, W.L. Mao, *Amorphous diamond: A High-Pressure superhard carbon allotrope*, Physical Review Letters, 107 (2011) 30–33.

[Mal18] J.B. Malherbe, O.S. Odutemowo, E.G. Njoroge, D.F. Langa, T.T. Hlatshwayo, C.C. Theron, *Ion bombardment of glassy carbon*, Vacuum 149 (2018) 19-22.

[McC94] D. McCulloch, S. Prawer, A. Hoffman, *Structural investigation of xenon-ion-beam-irradiated glassy carbon*, Physical Review B 50 (1994) 5905.

[Miy98] K. Miyoshi, *Structures and mechanical properties of natural and synthetic diamonds*, Lewis Research Center, Ohio, 1998.

[Niu12] H. Niu, X. Q. Chen, S. Wang, D. Li, W. L. Mao, Y. Li, *Families of superhard crystalline carbon allotropes constructed via cold compression of graphite and nanotubes*, Physical Review Letters, 108 (2012) 31–35.

[Nod64] T. Noda, M. Inagaki, *The structure of glassy carbon*, Materials Research Bulletin 37 (1964) 1534–1538.

[Odu18] O.S. Odutemowo, J.B. Malherbe, L.C. Prinsloo, E.G. Njoroge, R. Erasmus, E. Wendler, A. Undisz, M. Rettenmayr, *Structural and surface changes in glassy carbon due to strontium implantation and heat treatment*, Journal of Nuclear Materials 498 (2018) 103–116.

[Pau66] L. Pauling, *The structure and properties of graphite and boron nitride*, Proceedings of the National Academy of Sciences, 56 (1966) 1646–1652.

[Pie93] H.O. Pierson, *Handbook of carbon, graphite, diamond and fullerenes: properties, processing and applications*, Noyes Publications, New Jersey 1993.

[Sat06] M. Satoh, I. Takayanagi, *Review pharmacological studies on fullerene (C_{60})*, a novel carbon allotrope, and its derivatives, 518 (2006) 513–518.

[Sma85] H.W. Kroto, J.R. Heath, S.C. O'Brien, R.F. Curl, R.E. Smalley, *C_{60}: Buckminsterfullerene*, 318 (1985) 162-163.

[Ter00] H. Terrones, M. Terrones, E. Hernández, N. Grobert, J.C. Charlier, P.M. Ajayan, *New metallic allotropes of planar and tubular carbon*, Physical Review Letters 84 (2000) 1716–1719.

[Ter10] M. Terrones, A.R. Botello-Méndez, J. Campos-Delgado, F. López-Urías, Y.I. Vega-Cantú, F.J. Rodríguez-Macías, A.L. Elías, E. Muñoz-Sandoval, A.G. Cano-Márquez, J.C. Charlier, H. Terrones, *Graphene and graphite nanoribbons: Morphology, properties, synthesis, defects and applications*, Nano Today, 5 (2010) 351–372.

[Tok64] B. Tokiti, *The melting of glassy carbon*, 002 (1964) 1709–1710.

[Ume10] K. Umemoto, R. M. Wentzcovitch, S. Saito, T. Miyake, *Body-centered tetragonal C4: A viable sp^3 carbon allotrope*, Physical Review Letters, 2010.

[Www1] https://education.nationalgeographic.org/resource/carbon-cycle/.

[Www2] www.google.com, "Sigradure comercial glassy carbon", 2018.

[Yam68] S. Yamada, *A review of glasslike carbons*, 1968.

[Zha17] Z. Zhang, Q.i. Wang, *The new method of XRD measurement of the degree of disorder for anode coke material*, Journal of crystals 7 (2017) 1 – 10.

[Zhu11] Q. Zhu, A.R. Oganov, M.A. Salvadó, P. Pertierra, A.O. Lyakhov, *Denser than diamond: Ab initio search for superdense carbon allotropes*, Physical Review B: Condensed Matter and Materials Physics, 83 (2011) 1–4.

CHAPTER 3
ION IMPLATATION

Ion implantation is the term used to describe the process by which projectile ions are incorporated into target material. After penetration into the material, the energetic ions are slowed down by transferring their energy to the target atoms through elastic and inelastic collision events, and eventually stop at a certain depth within the target. Ion implantation can be used in a wide range of technologies. In materials science research, ion implantation has a variety of uses such as altering the chemical, physical, or electrical properties of solid materials as well as doping in the production of semiconductor devices.

The final distribution of ions in the target substrate can be calculated if all the processes (such as nuclear and electronic stopping forces, energy loss, energy straggling, as well as range and range straggling) are involved for the ion to rest within the target material are fully understood. Therefore, the most significant processes that occur during ion implantation are discussed in this chapter.

3.1 Stopping Force

Several articles and standard textbooks have extensively discussed the stopping force theory [Was07 and Wi173]. Charged particles (i.e., ions) lose energy as they pass through the material and eventually coming to stop at a certain depth within the target material. The mass and energy of the incident ions and the properties of the target material affect the stopping power of ions in solids [Www1]. The stopping force (also known as stopping power), which will be discussed in this section, is defined as the energy lost by a charged particle per unit path length at a given depth as a result of its interactions with the target atoms.

Nuclear energy loss and electronic energy loss are two independent processes that contribute to the transfer of energy from an ion to a substance. Elastic collisions between the ion and nucleus of atoms in the material or substrate cause the nuclear energy loss. However, it is the inelastic collisions between the ion and the electrons of the target atoms that causes the electronic energy loss. Sections 3.1.1 and 3.1.2 provide descriptions of these two types of

stopping force. The sum of the nuclear stopping force (S_n) and the electronic stopping force (S_e) gives the total stopping force (S) which is expressed as follows:

$$S = -\frac{dE}{dx} = \left[\frac{dE}{dx}\right]_n + \left[\frac{dE}{dx}\right]_e \tag{3.1}$$

where *n* is the nuclear stopping force, while *e* is the electronic stopping force.

The stopping cross-section (ε) can be calculated from equation (3.1) by dividing the total stopping force (*S*) by the target density (*N*) as follows:

$$\varepsilon = -\left[\frac{1}{N}\right]\left[\frac{dE}{dx}\right] \tag{3.2}$$

The range of the ion refers to the actual distance that an ion travels (within the material) before it finally comes to rest in a target material. By integrating the energy losses, it is possible to obtain the mean total range of the ions (i.e., average total range of the ions) as follows [Nor70]:

$$R_T = \int_0^{E_0} \frac{dE}{S} = \int_0^{E_0} \frac{dE}{\left[\frac{dE}{dx}\right]_n + \left[\frac{dE}{dx}\right]_e} \tag{3.3}$$

where R_T is the average total ion range and E_0 is the incident ion energy. The range of ions is discussed in section 3.4 in more detail.

In nuclear stopping force, due to elastic collisions between the projectile ion and the target atoms, the projectile ion transfers a large amount of energy and momentum to the target atoms. This can change the ion directions within the target and displace the target atoms from their lattice positions. However, in the electronic stopping force and due to the inelastic collisions between charged ions and electrons in the material, the change in the directions of the ion and displacement of the target atoms is negligible.

The projectile ions can have different stopping forces depending on ion types, energy, and substrate properties. At low ion energies, nuclear stopping dominates, while at high ion energies, electronic stopping dominates. As mentioned earlier, the direction of the projectile ion does not effectively change in the electronic stopping force, and the path is almost entirely a straight line. This is because the mass of heavy charged particles is much greater than the mass of electrons. Therefore, heavy ions are deflected only slightly by the electrons of the atoms. However, the nuclear stopping force will dominate after the projectile ion loses most of

its energy due to the ion and electron interactions. Therefore, in nuclear stopping force, a significant deviation from the initial direction of the projectile ion may occur due to the interaction between the ion and the nucleus of the target atom.

Figure 3.1 shows the different energy loss regimes. In Figure 3.1, *L* represents the low energy region, while *I* and *H* represent the intermediate and high energy regions, respectively. The nuclear stopping mechanism dominates at low energies below the critical energy (E_c) (see Figure 3.1). The electronic stopping dominates at higher energies (> E_c) and reaches a maximum before decreasing at the Bethe-Bloch region, or very high energies region (represented by *H* in Figure 3.1). These stopping mechanisms are influenced by the ion velocity (v_1) and the ion atomic number (Z), where in the low energy region $v_1 < v_0 Z^{2/3}$, where v_0 is the Bohr velocity. In this study, we are interested in the low energy loss regimes as discussed in section 3.1.2. Moreover, in the intermediate and high energy regions, the ion velocities should be in the range of $v_1 \approx v_0 Z^{2/3}$ and $v_1 >> v_0 Z^{2/3}$, respectively.

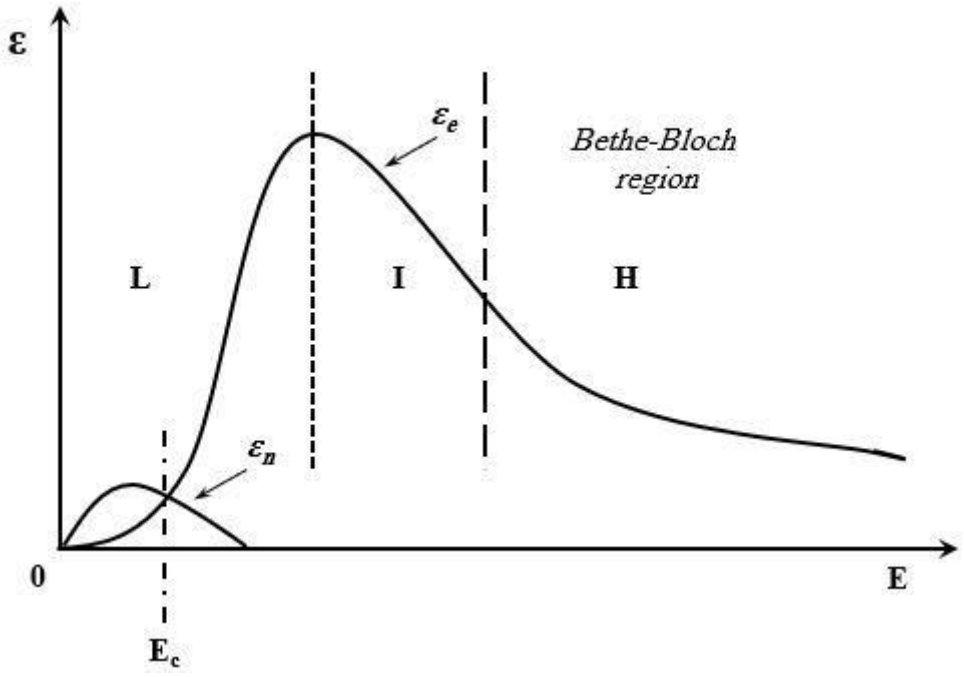

Figure 3.1: *Nuclear ε_n and electronic ε_e stopping forces as a function of ion energy E. Redrawn from [Was07].*

The electronic stopping force decreases in the Bethe-Bloch region due to the high velocity of the ion, where the ion has a very short time to interact with the target atoms. The

Bethe-Bloch equation in [Bet30], described this phenomenon mathematically in an extensive form.

3.1.1 Nuclear Stopping

In the nuclear stopping mechanism, energy is transferred from the ion to the target nuclei due to a series of elastic collisions (between the ion and target nucleus). The collision may be strong enough to displace the target atom from its lattice position. Therefore, the nuclear stopping force can cause lattice disorder and damaging the crystal structure.

As mentioned in the previous section (section 3.1) we are interested in the low and intermediate energy loss regimes. In this study, the glassy carbon samples were implanted with 150 keV Ru^{+} at room temperature and 200 ˚C. The Ru implantation energy used is much lower than the critical energy (E_c = 1207 keV, see Figure. 3.2), and thus, nuclear stopping power is expected to dominate during implantation [Zar15]. Furthermore, the implanted samples were analysed by Rutherford backscattering spectroscopy (RBS) using helium ions with energies of 1.4 MeV and 1.6 MeV, which are higher than the critical energy and in the intermediate energy regime (in region *L* as shown in Figure 3.1).

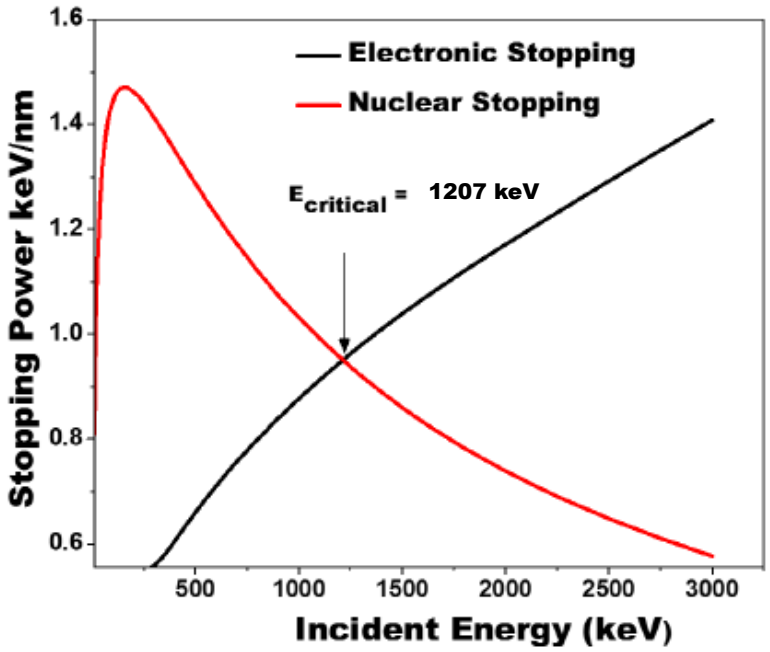

Figure 3.2: *The nuclear and electronic stopping powers of glassy carbon (with a density of 1.42 g/cm3) for Ru ions were determined using the stopping and ranges of ions in matter (SRIM) program [SRi12].*

Theoretically, the nuclear stopping can be explained by a series of binary collisions between two charged particles, which can be describe by classical kinematics (see Figure. 3.3). Ion scattering and energy transfer can be described as simple two-body collisions if the interaction between the incident ion and the target atom is isolated (i.e., isolated from the rest of the target atoms). This assumption means that the incident ion will lose the same amount of energy as the target atom would gain in a head-on collision, i.e. a two-body collision. An incident ion's energy loss (*T*) to the target atom is expressed as [Tow94]:

$$T = E_0 \frac{4M_1M_2}{(M_1+M_2)^2} sin^2(\frac{\theta}{2}) \tag{3.4}$$

where E_0 is the energy of the incident ion, M_1 is the atomic mass of the projectile, M_2 is the atomic mass of the target atom and θ is the scattering angle in the centre of mass system. The maximum transferred energy, $T_{max} = 4M_1M_2E_0/(M_1+M_2)^2$, when ($\theta = \pi$), is given when the collision is head-on, so:

$$T = T_{max} sin^2(\frac{\theta}{2}) \tag{3.5}$$

A binary elastic collision can be assumed to be the mechanism for energy transfer from the ion to the target atoms [Was07]. For a theoretical description of average energy transfer, we need to determine the probability of such a collision using the scattering cross-section reaction σ.

$$S_n(E) = N \int_0^{T_{max}} T d\sigma\,, \qquad d\sigma(T) = 2\pi b db \tag{3.6}$$

Figure 3.3 shows the distance between the asymptotic trajectory of the colliding projectiles *b*, where *b* is the impact parameter.

A projectile will transfer energy *T* to target atoms based on the collision event over all possible impact parameters b. Therefore, to calculate the nuclear stopping, the impact parameters is integrated as follows:

$$S_n(E) = 2\pi \int_0^{b_{max}} T(E,\theta)\, b db \tag{3.7}$$

For determining nuclear stopping power, the biggest challenge is calculating the repulsive interaction potential *V(r)*. Because the collision is being treated as a binary collision, without any external effects, it is acceptable to describe the particles as point masses (this is

acceptable based on the nucleus size). Therefore, the potential for interaction can simply be treated as the potential between the two nuclei, with electrons serving only to screen positive nuclear charges from each other, i.e., to reduce the effective positive charge on each nucleus. Moreover, in ion implantation at high energies and small interatomic separations of target atoms, r, $0 < r << a_0$ where a_0 is the Bohr's radius (0.53 Å), $V(r)$ reduces to repulsive Coulomb interactions between the nucleus. The screen of charges at intermediate separations (the most relevant region for ion bombardment) makes it very difficult to describe this region accurately [Bac12].

The Coulomb interatomic potential becomes invalid during ion implantation since the distance between the two nuclei (of the incident ion and the target atom) is typically in the order of a_0. Since the nuclei have limited interaction ranges, no other nuclei will be involved in the process. Thus, the effects of charge screening have been investigated and modelled by other researchers, and they all agree that the Coulomb potential should be multiplied by a screening function $\Phi(r)$, such that the Coulomb potential $V(r)$ then becomes [Wer06, Bac12]:

$$V(r) = \frac{Z_1 Z_2 e^2}{4\pi\varepsilon_0 r}\Phi\left(\frac{r}{a}\right) \tag{3.8}$$

where Z_1 and Z_2 are the atomic numbers of the ion and target atom respectively, e is the electron charge, a represents the screening length, which is determined by Z_1 and Z_2, and r/a is called the reduced radius. Many classical interatomic potentials have a function $\Phi(r/a)$ that is independent on Z_1 and Z_2 because of the reduced radius r/a.

Several attempts have been made to fit individual interatomic potentials successfully. A screening function based on the Hartree-Fock equation, and the local density approximation developed by Ziegler, Littmark, and Biersack is widely used for modelling atomic collisions [Zie85]. With this approach, they were able to derive an expression for universal screening potential, Φ, as given below:

$$\Phi = 0.1818e^{-3.2x} + 0.5099e^{-0.9423x} + 0.2802e^{-4029x} + 0.02817e^{-0.2016x} \tag{3.9}$$

where (x) equals (r/a) is defined as the reduced radius based on the universal screening length which is given as:

$$a = \frac{0.8854\, a_0}{Z_1^{0.23} + Z_2^{0.23}} \tag{3.10}$$

where a_0 is the Bohr's radius, which is equal to 0.529 Å. Based on this potential, binary collision codes like (SRIM) are frequently used for calculating implantation profiles.

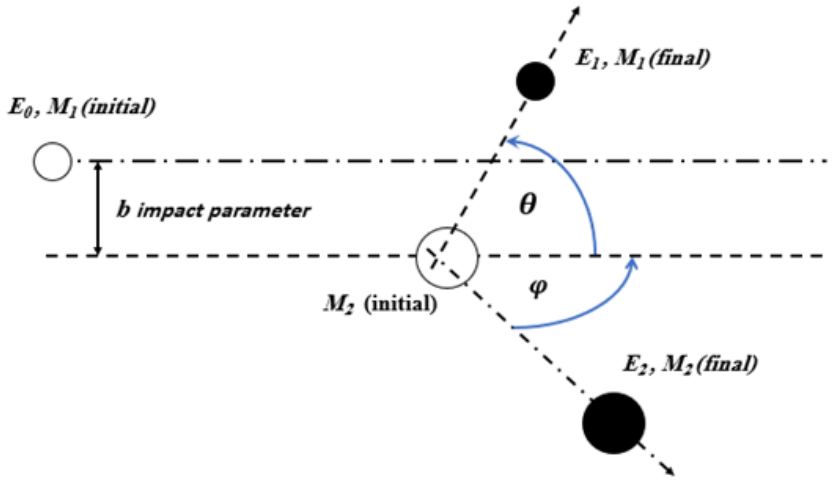

Figure 3.3: *An energetic ion scatters by a stationary atom in the laboratory.*

3.1.2 Electronic Stopping

When an energetic ion penetrates a material, it is first slowed down by inelastic collisions with the electrons of the target atoms. In this process, energy is transferred from the ion to the target electrons in a more complex manner than in nuclear stopping discussed above. Over the past decades, researchers have studied the processes that facilitate the transfer of kinetic energy from an ion to a target electron [Chu78, Zie85]. A couple of these processes are the excitation and ionization of target atoms and the electron capture or ionization of incident ions. According to equation (3.11), the energy loss process usually divides into three parts according to ion velocity and Bohr velocity, given as:

$$v_0 = \frac{e^2}{\hbar} \tag{3.11}$$

where v_0 is the Bohr velocity, e is the electron charge and $\hbar$ is the reduced Planck's constant which equal $h/2\pi$, where h is the Planck's constant. In the low energy region as shown in Figure 3.1, where the nuclear stopping dominates, the ion velocity v_1 is less than $v_0 Z^{2/3}$. For ruthenium ions, the $v_0 Z^{2/3}$ is equal to 2.7×10^9 cm/s. At an energy of 150 keV of ruthenium ions, the initial velocity (v_1) of the ruthenium ions is 7.8×10^7 cm/s. This velocity v_1 is less than $v_0 Z^{2/3}$. In this scenario, the ion cannot transfer enough energy to electrons with lower energies

than Fermi levels. Thus, in this region, inelastic energy loss is limited to electrons at Fermi levels. The electronic stopping in this region is calculated by assuming a free electron gas with a density (ρ). Therefore, the electronic stopping (S_e) of a charged particle is [Lin54]:

$$S_e = \int L(v,\rho)(Q(v))^2 \rho dV \tag{3.12}$$

where Q is the charge of the ion, dV is the volume element of the target, and L is the stopping interaction of an ion with unit charge and velocity, v, and ρ is the electron density of the volume element of the target dV.

As shown in Figure 3.1, the second region of energy loss refers to the intermediate region, where the ion velocity (v_1) is almost the same as $v_0 Z^{2/3}$. The ion is partially ionized in this region, and electronic stopping is maximal.

For very high ions velocities, where $v_1 >> v_0 Z^{2/3}$, the Bethe-Bloch equation [Bet30] defines the ion velocity in the third region of the model (H region in Figure 3.1). In this region, electronic stopping is proportional to Z_1^2 as shown in the Bethe-Bloch equation below:

$$\varepsilon_e = \frac{4\pi Z_1^2 Z_2 e^4}{m_e v_1^2}\left[\ln\frac{2m_e v_1^2}{I} - \ln(1-\beta^2) - \beta^2 - \frac{C}{Z_2} - \frac{\delta}{2}\right] \tag{3.13}$$

where e and m_e are the electron charge and electron mass, respectively, v_1 is the ion velocity, and β is the velocity of the ion divided by the speed of light (c) ($\beta = v_1/c$). At very high kinetic energies, the density function (δ) is due to dielectric polarization of the stopping medium, while C/Z_2 is the shell correction, and I indicate the mean excitation potential which is theoretically defined by [Kam84], as follows:

$$\ln I = \sum_n f_n \ln(E_n - E_0) \tag{3.14}$$

E_0 and E_n represent the ground state and possible energy transitions, respectively, for target atoms, where f_n is the corresponding oscillator strengths. In order to estimate I, many models have been used. Block's rule [Blo33] provides an approximate value for I, as follows:

$$I = (10\ eV)\ Z_2 \tag{3.15}$$

where Z_2 is the target atomic number.

This study focuses on the low and intermediate energy loss regimes shown in Figure 3.1. At an energy of 150 keV, ruthenium ions were implanted in glassy carbon, which falls in the low energy loss regime. The migration behaviour of ruthenium in glassy carbon was studied with Rutherford backscattering spectrometry (RBS). In the RBS analysis, helium particles with an energy of 1600 keV were used, which is in the intermediate energy regime.

3.2 Energy Straggling

When an energetic ion moves through a medium, it loses energy through many interactions with its atoms. Such discrete interactions cause statistical fluctuations. As a result, ions with the same initial energy will not have the same energy when they traverse the same thickness (x) of the same medium. This phenomenon is known as energy straggling [Fe186].

Straggling has been described by several theories, but most of them are inaccurate. Bohr proposed a simple theory, in which the energy straggling, Ω_B^2, is given as [May77].

$$\Omega_B^2 = 4\pi Z_1^2 Z_2 e^4 N x \tag{3.16}$$

where Ω_B^2 is Bohr's energy straggling, Z_1 and Z_2 are the atomic numbers of the projectile and target, respectively, N is the atomic density, and x is the thickness of the target. Assuming the ion energy distribution is Gaussian in most cases, the full width at half maximum (FWHM) of the distribution can be expressed as follows:

$$FWHM_B = 2\Omega_B\sqrt{2\ln 2} \tag{3.17}$$

In accordance with Bohr's theory, the electronic energy straggling occurs regardless of the projectile's energy. Bohr's theory predicts the change in the value of the energy increases with the square root of the number of electrons per unit area ($N\Delta x Z_2$) in the target [Nas14]. Basically, Bohr's theory assumes [Bon71]:

(i) The atoms of the target are distributed randomly.

(ii) The projectile has a high velocity compared to the orbital velocity of the target electrons.

(iii) Only a slight change in the projectile's energy occurs during penetration.

Bohr's theory of straggling has been modified by Lindhard and Scharff [Lin62] [Lin68] [Lin96], Bonderup and Hvelplund [Bon71]. Their theory includes corrections for low and medium energies where the Bohr's assumptions may not be valid.

3.3 Range and Range Straggling

Mean total range R_T refers to the mean distance that energetic ions with initial energy E_0 have travelled from the surface of a material to the point where they stop. This is also called the average total range. In equation (3.3) above, we get the average total range.

Multiple scattering of ions from target atoms and statistical fluctuations of interactions results in zigzagging paths of ions during energy loss processes. As a result of statistical fluctuations of interactions, the same ions can be implanted at different depths, even if their initial energy is the same. Based on these factors (e.g., statistical fluctuations of interactions), equation (3.18) below gives the range of an ion.

$$R_i = \sum l_i \tag{3.18}$$

where R_i is the ion's range and l_i represents the length of an individual section of an ion moving through a target medium. Figure 3.4 illustrates the relationship between R_i and l_i. The average total range R_T (i.e., the mean total range of the ions) is given by:

$$R_T = \frac{R_{i_1} + R_{i_2} + R_{i_3} + \cdots + R_{i_n}}{n} \tag{3.19}$$

where R_i represents the range of each ion, and n represents the number of incident ions.

When the energetic ions penetrate a material, they follow a straight line due to their high velocity. At this stage, electronic stopping dominates and there is no nuclear stopping. As they lose energy due to the collisions with the target atom their velocity decreases causing them to follow a zigzag motion. At this point, nuclear sopping dominates. Ions with low energy have a shorter path that exhibits large deflections. The projected range (R_p) of an ion is the length (perpendicular to the target surface) between the target surface and where the ion comes to rest - see Figure 3.4. The R_p of an ion is always smaller than its R_i due to scattering in its interactions with the substrate – see Figure 3.4. For a given substrate and ions with the same initial energy,

the ion range R_T is the averages of all the ion ranges, while R_p is the averages of ion projected ranges.

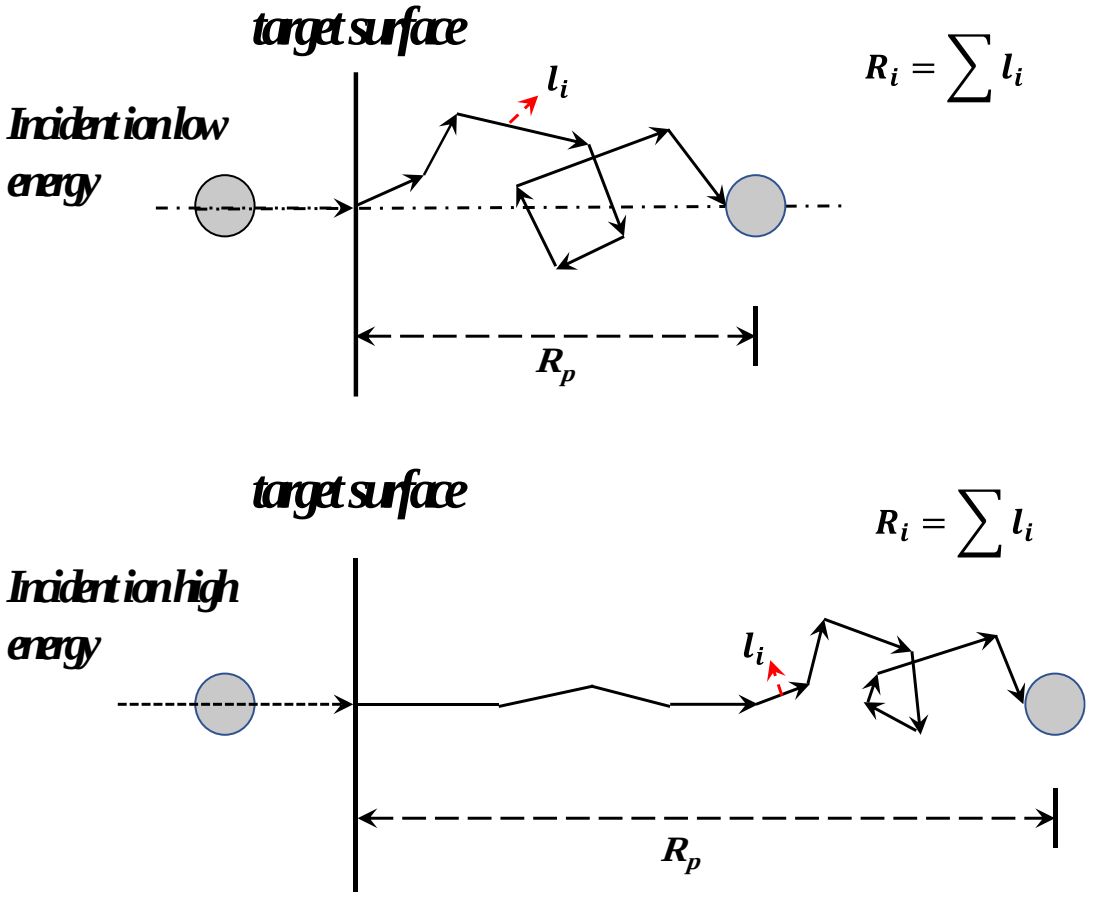

Figure 3.4: *An ion with low energy (top figure) and high energy (bottom figure) will have a projected range R_p and a total range R_i in the target material.*

It is common for the implanted profile to be very close to a Gaussian profile, as illustrated in Figure 3.5 (showing the R_p, *FWHM* and ΔR_p). A major reason for this is that the collisions between energetic impinging ions and substrate atoms have a statistical nature [Mal17]. The concentration of incident ions at depth x in the target material is given by [Hic07]:

$$C(x) = C_P \, e^{\left[-\frac{(x-R_p)^2}{2\pi\Delta R_p^2}\right]} \tag{3.20}$$

where ΔR_p is the range straggling (standard deviation of the distribution), x is the depth in the target material, while R_p is the projected range and C_p is the maximum concentration value/height of a Gaussian ion distribution, which can be expressed as follows [Agu88]:

$$C_P = \frac{\emptyset}{\sqrt{2\pi N \Delta R_p}} \tag{3.21}$$

where $\emptyset$ (ion/cm^2) and N are the ion dose and atomic density of the substrate, respectively. The range straggling (standard deviation) of a Gaussian distribution can be expressed as follows:

$$\Delta R_p = \sqrt{\frac{1}{\emptyset}\int_{-\infty}^{\infty}\left(x - R_p\right)^2 C(x)\, dx} \tag{3.22}$$

The projected range (R_p) is the average depth of the implanted ions, and it can be calculated as follows:

$$R_p = \frac{1}{\emptyset}\int_{-\infty}^{\infty} x\, C(x) dx \tag{3.23}$$

Based on the standard deviation shown in equation (3.22), the FWHM of the implantation profile can be calculated as follows: $FWHM = 2\ (\Delta R_p)\sqrt{2\ln 2}$. In our experiment, we found that ruthenium implanted in glassy carbon had a near Gaussian depth profile - see Figure 3.5. Using equations (3.24) and (3.25), we can determine the skewness and kurtosis moments in a Gaussian profile. Basically, skewness, γ, determines the degree of asymmetry in a distribution. If the distribution has an asymmetric tail that extends toward more positive values in the profile, then the skewness will have a positive value, and if the opposite is true, then the skewness of the profile will be negative.

$$\gamma = \frac{\int_{-\infty}^{\infty}(x-R_p)^3\, C(x)dx}{\emptyset\, \Delta R_p^3} \tag{3.24}$$

$$\beta = \frac{\int_{-\infty}^{\infty}(x-R_p)^4\, C(x)dx}{\emptyset\, \Delta R_p^4} \tag{3.25}$$

where β is Kurtosis, which is described as the tail of the contribution ion distribution profile over the flatness of the profile shape. In a perfect Gaussian profile, the skewness of the profile shape should equal zero while the kurtosis should equal 3.

Figure (3.5) shows the depth profile of ruthenium in glassy carbon. In order to determine the projected range (R_p), range straggling (ΔR_p), skewness (γ) and kurtosis (β) of the as-implanted Ru depth profile, the Genplot fitting function program was used to fit it to an Edgeworth distribution. Below is an expression for the Edgeworth distribution:

$$N(x) = Af(x)e^{\left[\frac{(x-R_p)^2}{2\Delta R_p^2}\right]} \quad (3.26)$$

$$f(x) = 1 + \frac{\gamma}{6}\left[\left(\frac{x-R_p}{\Delta R_p}\right)^3 - 3\left(\frac{x-R_p}{\Delta R_p}\right)\right] + \frac{(\beta-3)}{24}\left[\left(\frac{x-R_p}{\Delta R_p}\right)^4 - 6\left(\frac{x-R_p}{\Delta R_p}\right)^2 + 3\right] \quad (3.27)$$

Based on Figure (3.5), it is clear that these three curves agree with each other, which implies that our as-implanted Ru has a Gausian shape. In the next chapter, we will discuss the importance of this point for determining the diffusion coefficient from the depth profiles obtained from Rutherford Backscattering Spectrometry (RBS).

Figure (3.5) shows the Ru depth profile, which has a skewness (γ) of 0.16, a kurtosis (β) of 3, a projected range (R_p) of 123 nm, and straggling (ΔR_p) of 35 nm. As mentioned above, for a perfect Gaussian profile, both skewness and kurtosis should be zero and three, respectively. In this case the values of skewness and kurtosis for the Ru depth profile are very close to those of a perfect Gaussian profile.

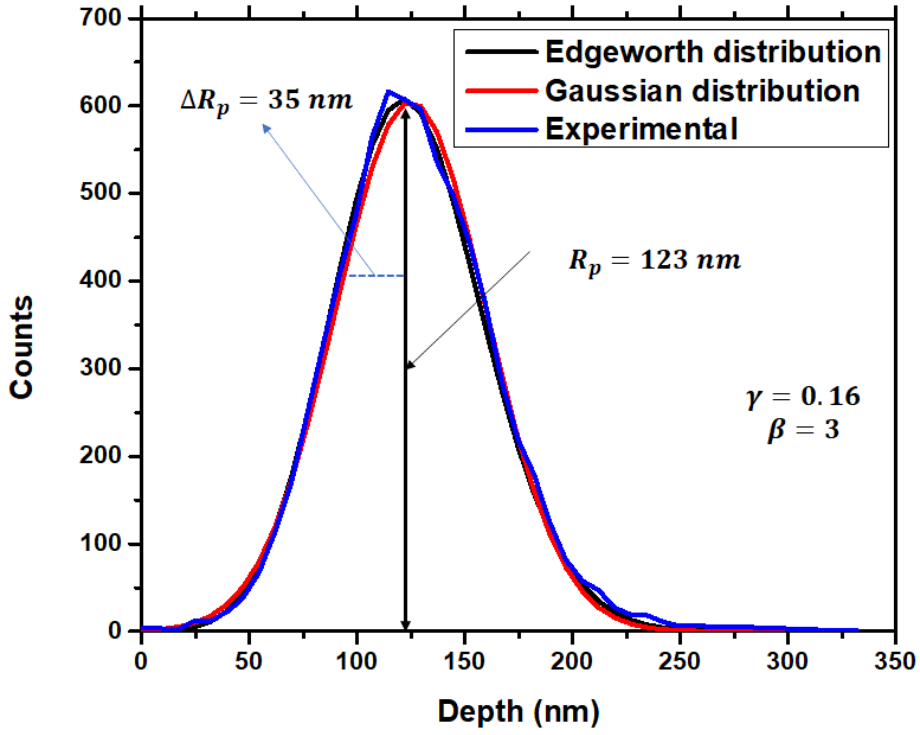

Figure 3.5: *The projected range, straggling, skewness, and kurtosis for the depth profile of ruthenium ions implanted in glassy carbon. The depth profile was fitted to Edgeworth distributions to get these values.*

3.4 Simulation of ruthenium ion implanted in glassy carbon

It is important to begin with a simulation before performing an experiment to gain an understanding of ion implantation details. In this study, a variety of parameters and moments related to ion implantation (such as R_p, ΔR_p, γ *and* β) were calculated using the Stopping and Ranges of Ions in Matter (SRIM) program [Sri12]. A variety of programs are included in the SRIM program, including the Transport of Ions in Matter (TRIM) program. In order to simulate and predict the effects of ruthenium ion implantation on glassy carbon, TRIM was used. The depth profile obtained from TRM was compared with the profile from the RBS data.

TRIM is an extremely efficient computer program with an error rate of approximately 5 to 10 percent. When using the program, parameters of interest must be selected (i.e., ions, ion's energy and the substrate). However, TRIM does not consider other parameters, such as crystal structure and dynamic composition, that can cause deviations when compared to the real data after implantation. As the incident ion penetrates the target material, changes occur in the material. There are several assumptions made by TRIM, including the following:

- It is assumed that the target is amorphous, therefore crystal orientation effects are not taken into consideration.
- It does not take into account thermal effects, like redistribution of implanted ions by thermal energy or vacancy effect.
- There is no consideration given to the recombination of interstitials with vacancies resulting from bombardment processes.
- Binary collisions alone are used to predict the projected range (the influence of neighbouring atoms is neglected).
- In the case of electronic and nuclear stopping powers, the data points from many experiments are used to calculate the average stopping powers.

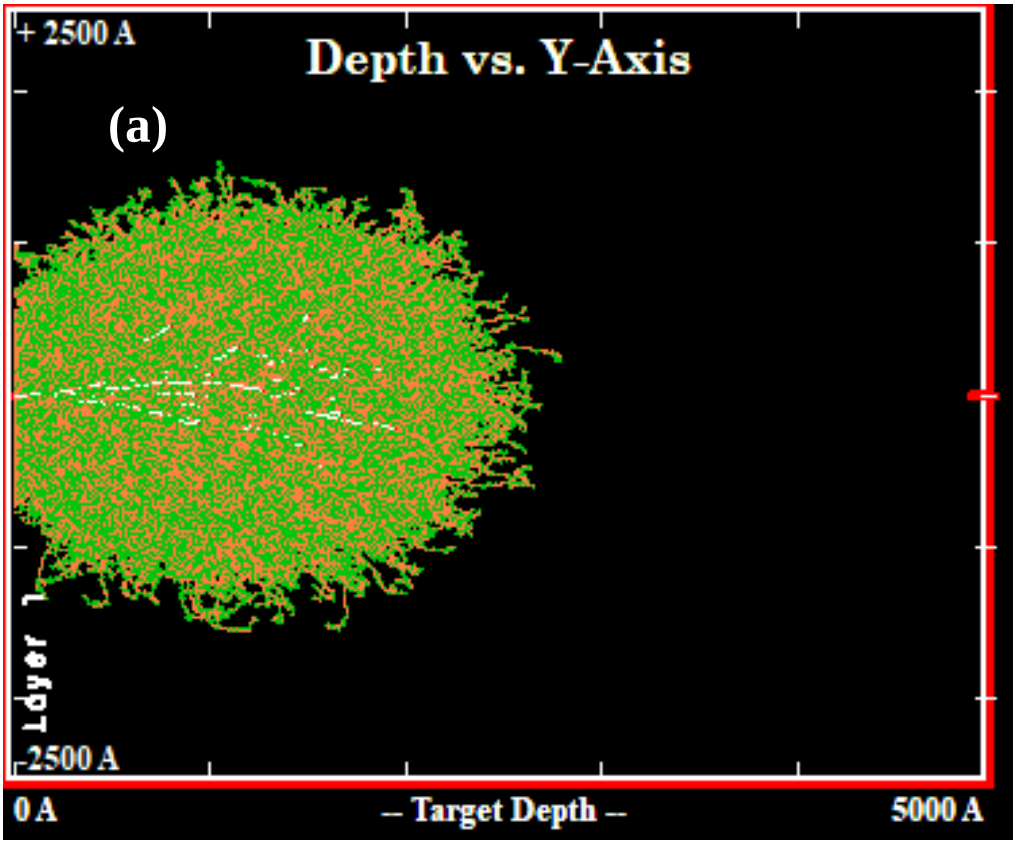
+ 2500 A
Depth vs. Y-Axis
(a)
Layer 1
-2500 A
0 A
-- Target Depth --
5000 A

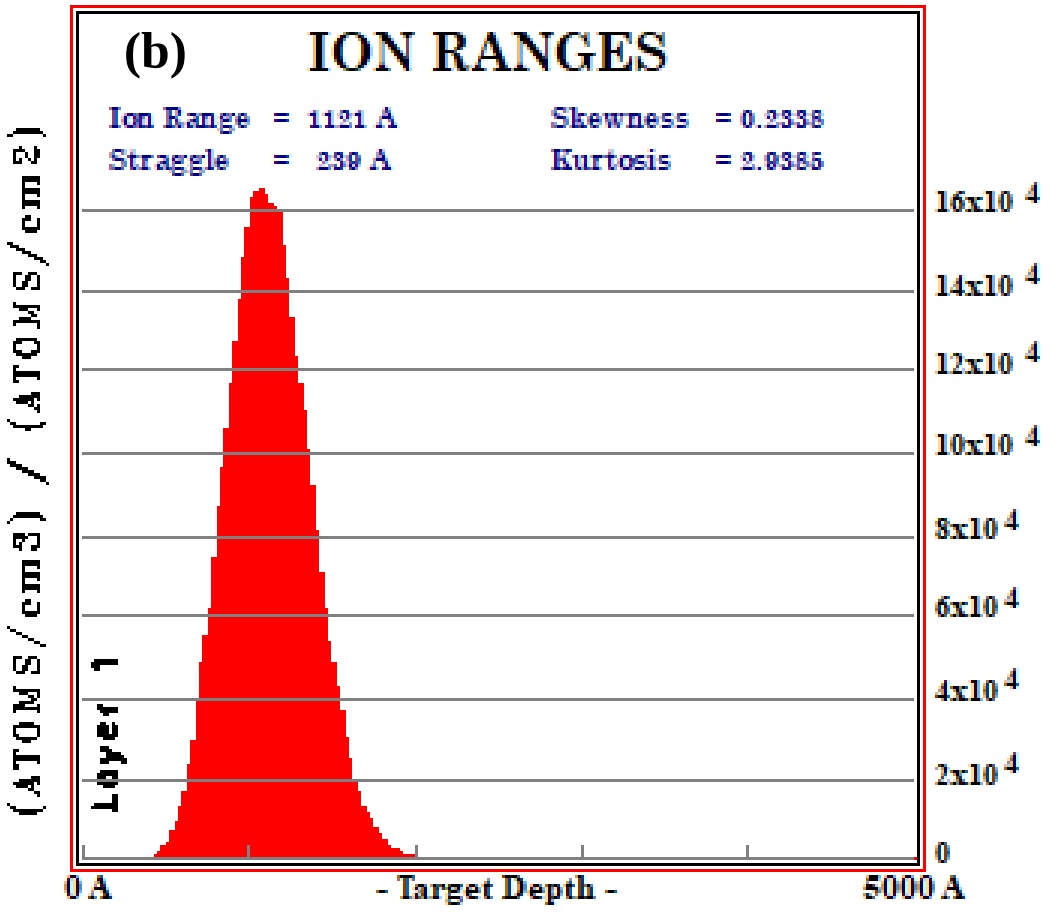
(b)
ION RANGES
Ion Range = 1121 A
Straggle = 239 A
Skewness = 0.2338
Kurtosis = 2.9385
(ATOMS/cm3) / (ATOMS/cm2)
16x10 4
14x10 4
12x10 4
10x10 4
8x10 4
6x10 4
4x10 4
2x10 4
0
Layer 1
0 A
- Target Depth -
5000 A

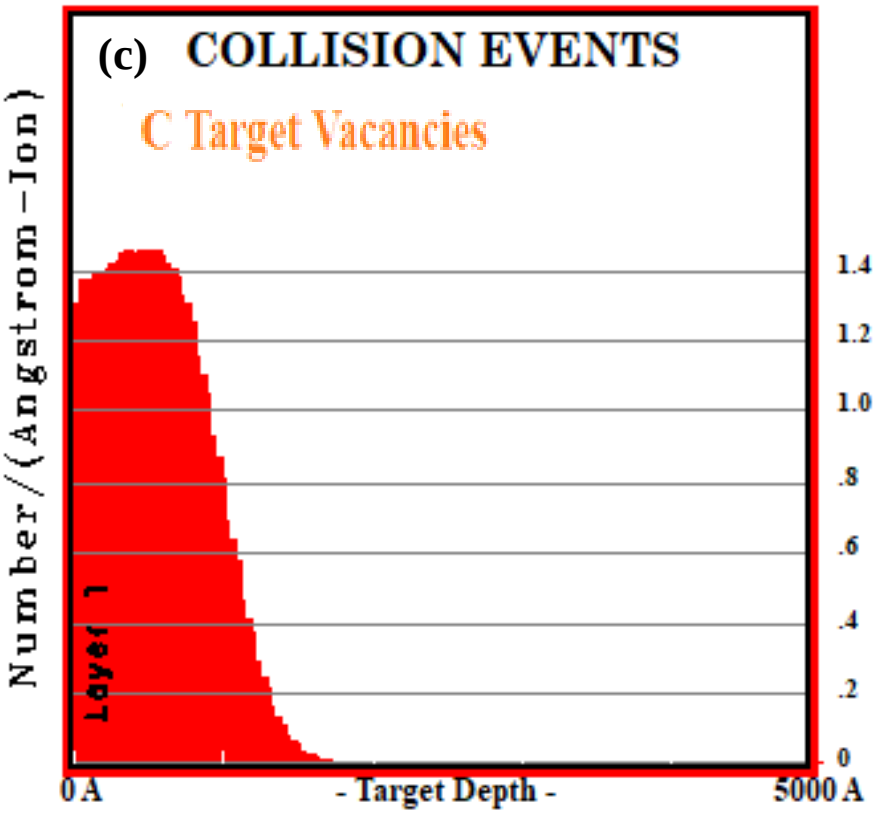

Figure 3.6: *Simulation based on TRIM [Sri12] showing: (a) the trajectory of 150 keV ruthenium ions implanted in glassy carbon; (b) the distribution of Ru ions implanted; (c) the distribution of vacancies in glassy carbon.*

Furthermore, TRIM simulations were also used to determine the displacement per atom (dpa) introduced in glassy carbon by Ru implantation using equation (3.28) below [Hal17]:

$$dpa = \frac{\frac{vac}{ion\,Å}\times 10^{8}}{\rho_{GC}(atoms\ cm^{-3})} \times \emptyset\ (ions\ cm^{-2}) \qquad (3.28)$$

where $\emptyset$ is the ion fluence, ρ_{GC} is the theoretical atomic density of glassy carbon (7.119×10^{22} atoms/cm^3) and vac/ionÅ is the vacancy per ion ratio from TRIM [Zie85].

3.5 Amorphization

As a result of implantation at low temperatures, such as room temperature (RT), and low energies, each ion produces a region of disorder within the ion track in the target material.

Moreover, energy deposition caused by ion bombardment causes crystal lattice damage during implantation. In some cases, it may be possible to achieve full amorphization or extended disorder in the target material depending on the mass and fluence of the implanted ions (e.g., Ru). Increasing the implantation fluence causes the lattice disorder to increase, causing more atoms to be displaced and leading to the formation of amorphous layer. The energy of implanted, at the low energies < 400 keV, ions can affect the structure of the target material, causing it to induce amorphization of the target substrate.

The glassy carbon material is easily amorphized due to its predominant covalent bonds (e.g., carbon). As a graphitic material, glassy carbon has the structure of a long-range disorder coexisting with the order of six-hold aromatic rings in nanosized graphite. Numerous authors have studied the amorphization of glassy carbon caused by ion implantation [Iwa00] [Toi01] [Odu18], and they all agree that ion bombardment with high fluence increases glassy carbon density from (1.4–1.5) g/cm^3 to approximately 2.25 g/cm^3, which is the density of amorphous carbon. Due to the ion bombardment, glassy carbon's density changes, resulting in an improvement in its wear resistance. Therefore, the process of ion implantation may be able to improve glassy carbon's wear resistance. As a result of these properties, glassy carbon can also serve as an alternative material for nuclear waste storage.

3.6 Annealing of the radiation damage

The implanted ions may rest in more point defects being introduced in the crystal lattice such as vacant lattice position (fill a vacancy) or occupy a non-lattice position (become an interstitial). Ion implantation can also cause other point defects in the lattice such as interstitial atoms (self-interstitials or foreign interstitials) and substitutional atoms (foreign atoms that sit on the host lattice site). The annealing process allows the removal/reduction of the defects.

During annealing, energy is added to the crystal to reduce/remove damage by causing the defects to become mobile [Hic07]. Point defects can interact with one another to form extended defects at moderate temperatures. By annealing at a higher temperature or at a longer time, the defects will evolve to the point where the atoms will be able to locate lower-energy places in the crystal, thereby restoring its crystal structure [Gib72]. Figure 3.7 shows the effects of annealing on the crystal structure. As part of this study, glassy carbon (which bombarded with Ru ions) was annealed at low- and high-temperatures to determine how annealing affects

structural changes. In the glassy carbon with an amorphous structure (produced by ion implantation at room temperature and 200 ˚C), the annealing behaviour depends on its structure (which are discussed in more detail in chapter 2).

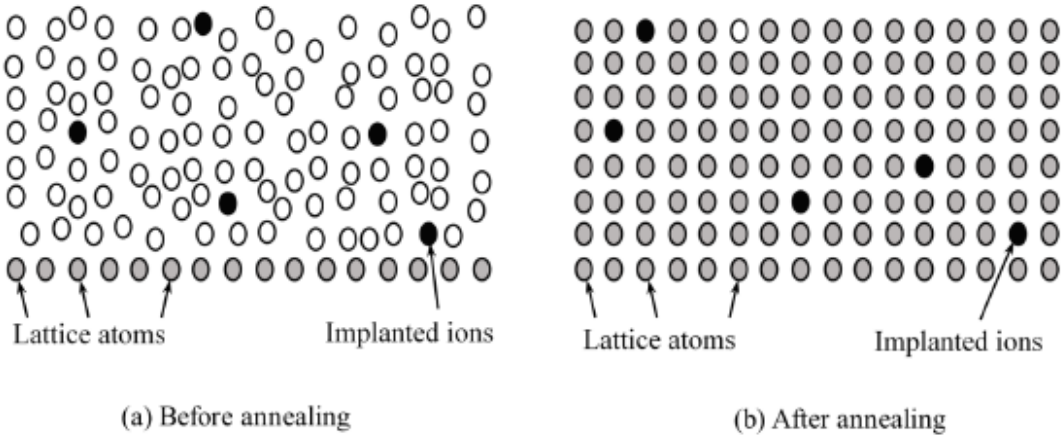

Figure 3.7: *(a) Crystal damage and (b) annealed the damage.*

References

[Agu88] F.A. Lopez, C.R.A. Catlow, P.D. Townsend, *Point defects in materials*, Academic press. (1988).

[Bac12] M. Backman, *Effects of nuclear and electronic stopping power on ion irradiation of silicon based compounds*, Helsinki, Finland, 2012.

[Bet30] H. Bethe, *Zur Theorie des Durchgangs schneller Korpuskularstrahlen durch Materie*, Ann. Phys. Leipzig 5 (1930) 324.

[Blo33] F. Bloch, *Zur Bremsung rasch bewegter Teilchen beim Durchgang durch Materie*, Ann. Phys. Leipzig 16 (1933) 285.

[Bon71] E. Bonderup, P. Hvelplund, *Stopping power and energy straggling for swift protons*, Physical Review A 4 (1971) 562 – 569.

[Chu78] W. Chu, J. W. Mayer, M. Nicolet, *Backscattering spectrometry*, Academic Press. (1978).

[Fe186] L. Feldman and J. Meyer, *Fundamental of surface and thin film analysis*, Elsevier Science Publishing Co. New York. (1986).

[Gib72] J.F. Gibbons, *Ion implantation in semiconductors—Part II: Damage production and annealing*, Proc. IEEE 60 (1972) 1062.

[Hal17] T.T. Hlatshwayo, L.D. Sebitla, E.G. Njoroge, M. Mlambo, J.B. Malherbe, *Annealing effects on the migration of ion-implanted cadmium in glassy carbon*, Nucl. Instrum. Methods Phys. Res. B 395 (2017) 34-38.

[Hic07] D.P. Hickey, *Ion implantation induced defect formation and amorphization in the Group IV semiconductors: Diamond, silicon and germanium*, URL: http://etd.fcla.edu. (2007).

[Inn20] A.J. Innocent, T.T. Hlatshwayo, E.G. Njoroge, T.P. Ntsoane, M. Madhuku, E.O. Ejeh, M. Mlambo, M.Y.A. Ismail, C.C. Theron, J.B. Malherbe, *Evaluation of diffusion parameters and phase formation between tungsten films and glassy carbon*. Vacuum 175 (2020) 109245.

[Iwa00] M. Iwaki and K. I. Terashima, *Change in atomic density of glassy carbon by Na ion implantation*, Surface and Coatings Technology 128-129 (2000) 429 – 433.

[Kam84] E. Kamaratos, *The mean excitation energy for stopping power I, the Bragg rule, and chemical and phase effects. Application of a statistical treatment to the determination of I for chemically bound particles*, Chem. Rev. 84 (1984) 561-576.

[Lin54] J. Lindhard, *On the properties of a gas of charged particles*, Kgl. Dan. Vid. Selsk. Mat. Fys. Medd. 28 (8) (1954).

[Lin62] J. Lindhard and V. Nielsen, *Nuclear collisions and ionisation fluctuations in charged particle detectors*, Physics Letters 2 (1962) 209 – 211.

[Lin68] J. Lindhard, V. Nielsen, M. Scharff, *Approximation method in classical scattering by screened coulomb fields*., Kgl. Dan. Vidensk. Selsk., Matematisk- fysiske Meddelelser 36, (10) (1968).

[Lin96] J. Lindhard, H. Allan, *Relativistic theory of stopping for heavy ions*, Physical Review A 53 (1996) 2443 – 2455.

[Mal17] J.B. Malherbe, P.A. Selyshchev, O.S. Odutemowo, C.C. Theron, E.G. Njoroge, D.F. Langa and T.T. Hlatshwayo, *Diffusion of a mono-energetic implanted species with a Gaussian profile*. Nucl. Instr. Methods. Phys. Res. B 406 (2017) 708.

[Mal18] J.B. Malherbe, O.S. Odutemowo, E.G. Njoroge, D.F. Langa, T.T. Hlatshwayo, C.C. Theron, *Ion bombardment of glassy carbon*, Vacuum 149 (2018) 19 – 22.

[May77] J.W. Mayer, E. Rimini, *Ion beam handbook for material analysis*, Academic Press, New York, 1977.

[Nas14] M. Nastasi, J. Mayer, Y. Wang, *Ion Beam Analysis, Fundamentals and Applications*, CRC Press, London 2014.

[Nor70] L.C. Northcliffe, R.F. Schilling, *Range and stopping-power tables for heavy ions*, Atomic Data and Nuclear Data Tables, 7 (1970): 233-463.

[Odu18] O.S. Odutemowo, J.B. Malherbe, L.C. Prinsloo, E.G. Njoroge, R. Erasmus, E. Wendler, A. Undisz, M. Rettenmayr, *Structural and surface changes in glassy carbon due to strontium implantation and heat treatment*, Journal of Nuclear Materials 498 (2018) 103 – 116.

[Sri12] J. Ziegler, *SRIM 2012 computer code*, 2012. URL: www.srim.org.

[Toi01] H. Toida, K. Terashima, T. Kobayashi, M. Osada, K. Watanabe, M. Iwaki, *Densification of glassy carbon by fluorine ion implantation*, Nucl. Instr. Methods. Phys. Res. 175-177 (2001) 532 – 536.

[Tow94] P.D. Townsend, P.J. Chandler, L. Zhang, *Optical effects of ion implantation*, Cambridge University Press, New York, 1994.

[Was07] G. Was, *Fundamentals of radiation materials science, metals and alloys*, Springer, Berlin. (2007).

[Wi173] R. Wilson, G. Brewer, *Ion beams with applications to ion implantation*, John Wiley and Sons Inc. New York. (1973).

[Www1] Stopping Power. URL: https://www.sciencedirect.com/topics/earth-and-planetary-sciences/stopping-power, (Visited on 13/11/2023).

[Zar15] E. Zarkadoula, M. Toulemonde, W. J. Weber, *Additive effects of electronic and nuclear energy losses in irradiation-induced amorphization of zircon*, Applied Physics Letters 107 (2015) 1 – 5.

[Zie85] J.F. Ziegler, J.P. Biersack, *The stopping and range of ions in matter*, Treatise on Heavy-Ion Science, Springer, US, (1985) 93 – 129.

CHAPTER 4
DIFFUSION

The atoms in the crystal lattice are located in the position of minimum potential energy, which is known as the fixed position or the lattice position. An atom can move from its fixed position if it gains enough energy (from an external energy source, such as thermal energy and energetic ion bombardment) to overcome the barrier between itself and the surrounding atoms bonded to it. Diffusion is the process by which material is moved by atomic motion from an area of high concentration to an area of low concentration [Cra75]. When more atoms randomly move from an area of higher concentration to another area of lower concentration, this is known as a net flux. Therefore, the concentration gradient of the material has a significant influence on the diffusion transport. Other factors, such as temperature (thermal energy), microstructure of the material and diffusing species can influence the diffusion. Moreover, the chemical reactions and microstructural changes in solids are affected by the diffusion process.

Diffusion can be divided into two main categories: time-dependent diffusion and steady state diffusion, which are discussed below.

4.1 Steady state diffusion

Steady state diffusion can be explained by Fick's first law which gives the relationship between the concentration and diffusional transportation in one dimension (*x*-direction) as shown in Figure. 4.1 and the following equation:

$$J = -D\left(\frac{dC}{dx}\right) \tag{4.1}$$

where J is the flux, C is the particle concentration (which can be molecules, atoms or ions), $\partial c/\partial x$ is concentration gradient (atoms/m^4), and D is the diffusivity or diffusion coefficient (which will be discussed in more detail in this chapter, Section 4.2). The minus sign in equation 4.1 is due to the fact that diffusion occurs in the opposite directions of the concentration gradient and atomic flux. The diffusion flux unit (J) is expressed as the number of particles (or moles) that flow perpendicularly to a unit area per unit time, while the unit of concentration C is the number of particles per unit volume. Therefore, from equation (4.1),

considering the units of J and C mentioned above, the unit of the diffusion coefficient D is defined as length^2 per unit time (i.e., m^2/s). The diffusion flux decreases towards zero as the sample becomes homogeneous, according to equation (4.1). The Fick's first law in three dimensions is generalized as follows:

$$J = -D\,\nabla C \tag{4.2}$$

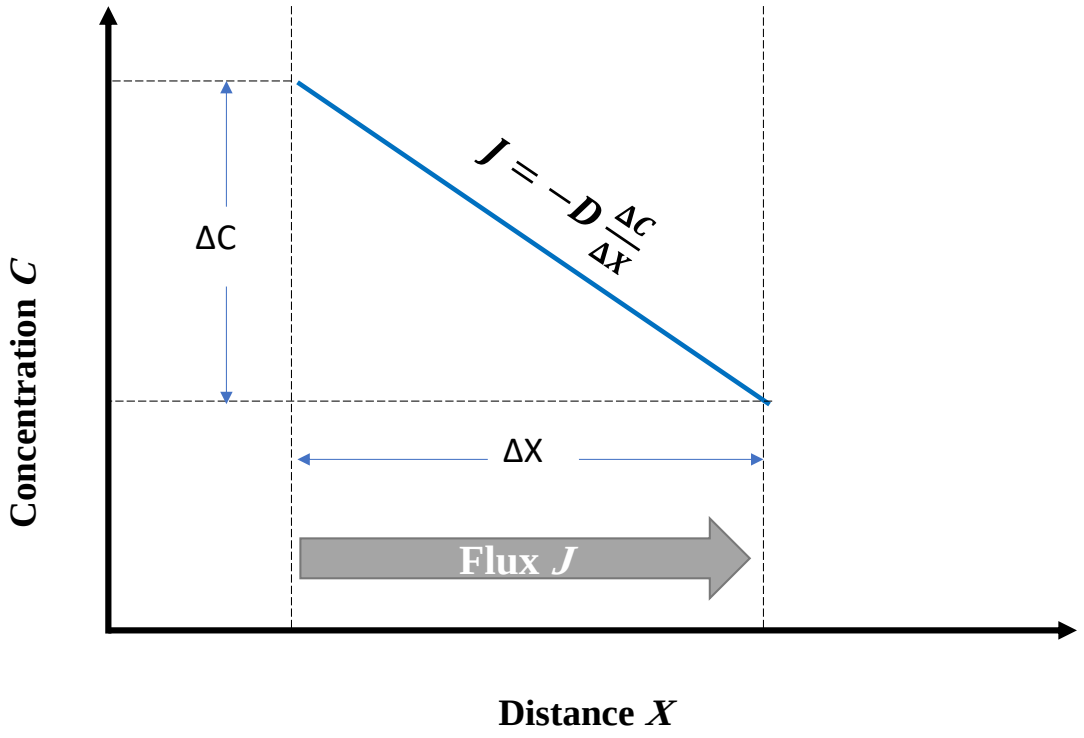

Figure 4.1: *Illustration of steady state diffusion showing the change in concentration C as a function of the distance x.*

4.2 Time dependent diffusion

In most real diffusion systems, the particle concentration profile (i.e., concentration gradient) changes with both distance and time, not with distance only as in steady state diffusion. The time-dependent diffusion is referred to as the non-steady state diffusion. Therefore, Fick modified his first law in equation (4.1) to take into account the change in concentration with time and distance. The new law is known as Fick's second law (see equation (4.3)). Consider a bar with a cross-sectional area, *A*, and a short length, *dx*, as shown in Figure. 4.2 below. From this Figure, by considering the two cross-sections separated by a distance *dx*,

the flux of the impurity entering the volume element J_1 will not be the same as the flux exiting the volume element ($J_1 \neq J_2$) [Cam01], then:

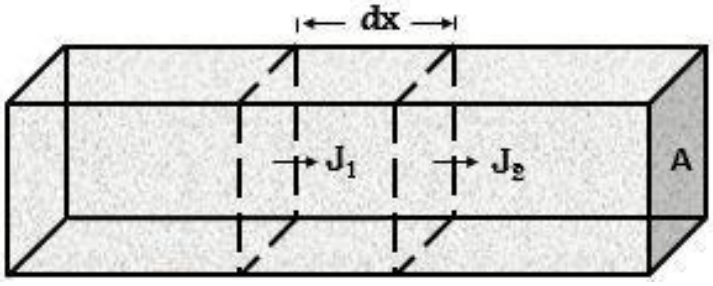

Figure 4.2: *A differential volume element (dx) in a bar with cross sectional area A. J_1 and J_2 are the impurity fluxes entering and leaving the volume, respectively. Obtained from [Cam01].*

$$\frac{\nabla J}{\partial x} = \frac{J_2 - J_1}{dx} \tag{4.3}$$

Since $J_2 \neq J_1$, the concentration of the diffusing impurities in the volume should change. By considering that the concentration of impurity atoms (or particles, or moles) in the volume element is related to the cross-sectional area and length ($A.dx$), then the continuity equation can be written as:

$$(A\,dx)\frac{\partial C}{\partial t} = -A(J_2 - J_1) = -(A\,dx)\frac{\partial J}{\partial x} \tag{4.4}$$

Or equation (4.4) can be expressed as:

$$\frac{\partial C(x.t)}{\partial t} = -\frac{\partial J}{\partial x} \tag{4.5}$$

Equation (4.1) can be substituted into equation (4.5) to get [She89]:

$$\frac{\partial C(x.t)}{\partial t} = \frac{\partial}{\partial x}\left(D\frac{\partial C}{\partial x}\right) \tag{4.6}$$

The continuity equation, or Fick's second law, can be expressed as follows if we assume that the diffusion coefficient D is independent of position (which is usually the case):

$$\frac{\partial C(x.t)}{\partial t} = D\frac{\partial^2 C}{\partial x^2} \tag{4.7}$$

The Fick's second law (equation (4.7)) in three dimensional can be written as:

$$\frac{\partial C(r.t)}{\partial t} = D\nabla^2 C \tag{4.8}$$

In limited temperature ranges, the Arrhenius equation gives the relationship between temperature in Kelvin (*T*) and diffusion coefficient (*D*) as follows [Ash14]:

$$D = D_0 \exp\left(-\frac{E_a}{K_B T}\right) \tag{4.9}$$

where E_a is the activation energy (it is the minimum amount of energy required to move an atom from its position), D_0 is a temperature independent pre-exponential factor and K_B is the Boltzmann constant.

4.3 Evaluation of the diffusion coefficient

Two books, titled ‘‘Diffusion in Condensed Matter’’ by Heitjans [Hei05] and ‘‘The Mathematics of Diffusion’’ by Crank [Cra75], extensively discuss the several methods for evaluating the diffusion of impurities in different materials.

The as-implanted profile is usually very close to a Gaussian distribution, as reported in the chapter on ion implantation (section 3.5). This results from the statistical nature of the collisions between energetic impinging ions and the substrate atoms [Mal17]. In generally, the diffusion of ions implanted in glassy carbon after high temperature annealing were found to be Fickian [Ism19, Ken19 and Mal21]. Malherbe *et al.* [Mal17] derived a solution to the Fick diffusion in equation (4.6) for an original Gaussian profile with projected range R_p and range struggling ΔR_p (see equation below) in order to calculate the diffusion coefficient *D* for the Fickian diffusion.

$$C(\xi, 0) = A_0\, exp\left[-\frac{(\xi - R_p)^2}{2\Delta R_p^2}\right] \tag{4.10}$$

Here, ξ is the depth below the surface. The solution for the diffusion of the implanted profile with annealing time is given by the two equations below:

$$N(x,t) = \frac{A_0 \,.\, \Delta R_p}{2\sqrt{2Dt+\Delta R_p^2}}\, e^{\left[-\frac{(x-R_p)^2}{4Dt+2\Delta R_p^2}\right]}\left[1 + erf\left(\frac{2DtR_p+x\Delta R_p^2}{\Delta R_p\sqrt{2(2Dt)^2+4Dt\Delta R_p^2}}\right) - ke^{\left[\frac{xR_p}{Dt+\Delta R_p^2/2}\right]}\left\{1 + erf\left(\frac{2DtR_p-x\Delta R_p^2}{\Delta R_p\sqrt{2(2Dt)^2+4Dt\Delta R_p^2}}\right)\right\}\right] \quad (4.11)$$

and

$$k = 1 - \left[\frac{2N_0}{A_0}\,\frac{\sqrt{2Dt+\Delta R_p^2}}{.\Delta R_p}\, exp\left(\frac{R_p^2}{4Dt+2\Delta R_p^2}\right) \Bigg/ \left\{1 + erf\left(\frac{R_p\sqrt{Dt}}{\Delta R_p\sqrt{2Dt+\Delta R_p^2}}\right)\right\}\right] \quad (4.12)$$

In the equation above, there are two extreme situations for the parameter k (i.e., k = 1 and k = -1). In the case of a perfect sink at the surface of the substrate, k = 1 (meaning that the arrived impurity at the surface is immediately sublimated), and in the case of a perfect reflecting surface, k = -1 (meaning no impurity is lost from the surface), respectively. In our calculations, k was a fitting variable.

4.4 Diffusion mechanisms in solids

Volume diffusion, surface diffusion, dislocation and grain boundary diffusion are the main mechanisms of diffusion in solids. The temperature and crystal structure have a considerable impact on these diffusion mechanisms. The average kinetic energy of the atoms increases with increasing temperature, causing the atoms to oscillate faster until they separate from the molecular bond. Diffusion in solids occurs when these oscillations are large enough to allow an atom to move from its lattice position in the crystal to another position.

4.4.1 Volume diffusion

In a crystal lattice, the migration of point defects causes volume diffusion, also known as lattice diffusion, to take place. The following types of point defects largely influence how volume diffusion occurs:

- Vacancy (substitutional)
- Interstitial (direct interstitial)
- Interstitialcy (self-interstitial) diffusion

4.4.1.1 Vacancy Diffusion Mechanism

The lattice vacancies are a type of point defect that represents unoccupied lattice sites in the crystal and plays a role in the diffusion of impurities. In the vacancy mechanism [She89], an atom in a crystal changes position with an adjacent vacancy. When this occurs, the atom that has moved leaves a vacancy. As a result, the vacancy also appears to have moved or jumped in the direction opposite to the atom during its movement (see Figure 4.3). The dotted circle and solid circle in this figure represent the vacancy and atom, respectively, while (a) and (b) show the vacancy and atom positions before and after diffusion.

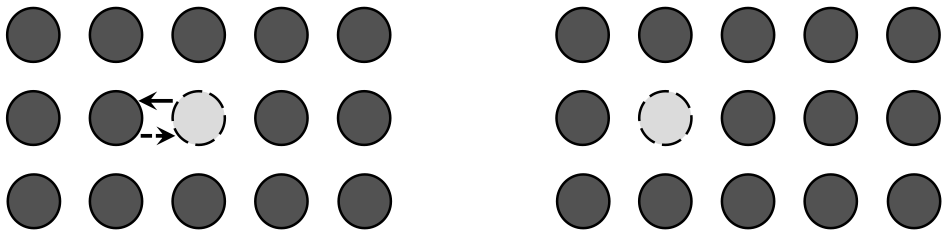

Figure 4.3: *Schematic diagram of the vacancy diffusion mechanism.*

4.4.1.2 Interstitial Diffusion Mechanism

The migration of an atom from one interstitial side to another in the crystal is known as interstitial diffusion. This migration occurs in the crystal without displacement of any of the lattice atoms (shown in Figure 4.4). Interstitial atoms can be smaller, larger, or the same size

as the host atoms. There are many more interstitial sites than vacancy sites in a crystal, interstitial diffusion is generally faster than vacancy diffusion. In addition, the bonding of the interstitials atoms to the surrounding atoms is usually weaker. Though, the lattice atom has stronger bonds (compared to interstitial atom) with its neighbouring atoms which must be broken to move to the vacancy site in the crystal. For these two reasons mentioned above, the interstitial diffusion within the crystal is faster than vacancy diffusion.

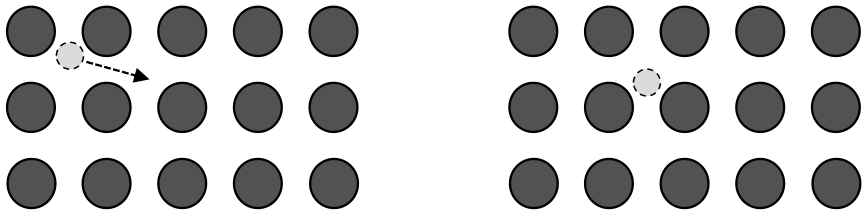

Figure 4.4: *Schematic diagram of the interstitial diffusion mechanism: the dotted circle represents an interstitial atom, the open circles represent lattice atoms, (a) and (b) shows the positions before and after interstitial diffusion respectively.*

4.4.1.3 Interstitialcy Diffusion Mechanism

In the interstitialcy diffusion, an interstitial atom (which is approximately the same size as the host atoms - see Figure 4.5) can push one of its nearest neighbour lattice atoms out of a lattice position and into an adjacent lattice site. As a result, the interstitial atom can move into a normal lattice site, in contrast to interstitial diffusion (mentioned in the section above) where the atom moves from one interstitial side to another interstitial side in the crystal.

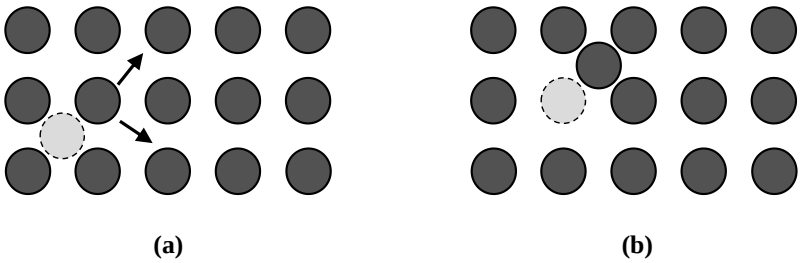

Figure 4.5: *Schematic diagram of the interstitialcy diffusion mechanism: the dotted circle represents an interstitial atom, the open circles represent lattice atoms, (a) and (b) shows the positions before and after interstitialcy diffusion respectively.*

4.4.2. High diffusivity paths

As previously discussed, the migration of the atoms in a crystal is usually through a vacancy, interstitial, or interstitial diffusion (which is known as volume diffusion). The volume diffusion is temperature dependent. In the high diffusivity paths (also known as short circuit diffusion), the diffusion of atoms occurs through grain boundaries, dislocations and surface diffusion. In solids, grain boundary diffusion (high diffusivity path) dominates the volume diffusion at lower annealing temperatures, e.g. up to and below 0.3 – 0.5 T_{mp} (melting point temperature). Whereas, at higher annealing temperatures (at 0.5 T_{mp}), the grain boundary diffusion is usually faster than volume diffusion [Lau03]. Short circuit diffusion is important in modern technology because many microelectronic devices depend on it. This is due to the diffusion process through grain boundaries or surface diffusion (i.e., short circuit diffusion) which affects the diffusion barrier between thin film layers in devices [Kum08].

The diffusion process in polycrystalline materials is more complex, due to the large number of crystallites with different sizes, shapes and orientations. Since the diffusion species may leak from the grain boundary into the lattice and vice versa, it is rare for the grain boundary diffusion to be decoupled from lattice or volume diffusion in this case. Therefore, in polycrystalline materials, atoms/impurities can diffuse along volume, grain boundaries, and surfaces [Poa78].

4.5. Segregation and aggregation in solids

Surface segregation is the enrichment of impurities from the bulk of the substrate to its surface, grain boundaries, or interfaces. The main reason for the segregation is the difference in chemical potential between the bulk and the surface of a given sample. The concentration of component in the bulk, the temperature, and the period of segregation (i.e., time during which segregation takes place) all affect the enrichment of segregation. The segregation process may also be affected by surface contaminants absorbed by the sample from the surrounding environment or those carried to the surface by diffusion from the bulk [Dow87].

Aggregation occurs whenever single atoms or nanoparticles cluster together forming larger objects - see Figure 4.6. Usually, the aggregation of atoms occurs due to the high cohesive forces between the atoms themselves, which leads to the formation of clusters or

particles [Jon37]. Atoms can aggregate to form nanoparticles through a number of different processes occur including condensation, pressurization, chemical reaction, electrodeposition, melting [Www1]. The aggregation of atoms can occur both on the surface (known as surface aggregation) and in the bulk of the substrate (bulk aggregation). In solids, surface aggregation is more pronounced compared to bulk aggregation, as the diffusion of atoms on the surfaces is much faster than that of atoms diffuse in the bulk, as mentioned in section 4.4.2.

For the bulk aggregation, several studies have shown that, the metal atoms implanted into the substrate were aggregated to form metal nanoparticles inside the substrate (i.e., in the bulk of the substrate), due to the high cohesive force between the implanted ions [Arn77, Jon37, Mio01 and Res14].

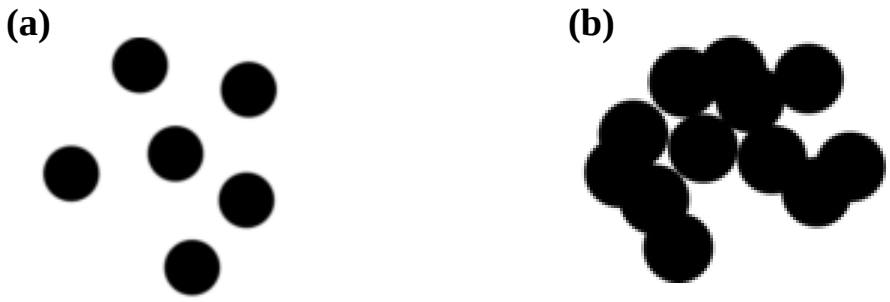

Figure 4.6: *A schematic diagram of the aggregation of atoms, (a) and (b) showing the positions of the atoms before and after aggregation respectively.*

References

[Ash14] S.A. Ashter, *Thermoforming of Single and Multilayer Laminates: Plastic Films Technologies, Testing, and Applications*, 1st Edition, William Andrew publishing, Elsevier, Amsterdam, Netherlands, (2014).

[Arn77] G.W. Arnold, J.A. Borders, *Aggregation and migration of ion-implanted silver in lithia-alumina-silica Glass*, J. Appl. Phys. 48 (1977) 1488–1496.

[Cam01] S.A. Campbell, *The science and engineering of microelectronic fabrication*, 2nd ed., Oxford University Press, New York, 2001.

[Cra75] J. Crank, *The mathematics of diffusion*, Oxford University Press, Bristol, England. (1975).

[Dow87] P.A. Dowben, A.H. Miller, R.W. Vook, *Surface segregation from gold alloys*, Gold Bulletin. 20 (1987) 54–65.

[Hei05] P. Heitjans, J. Karger, *Diffusion in condensed matter*, Springer, Netherlands. (2005).

[Ism19] M.Y.A. Ismail, *The migration behaviour of xenon implanted into glassy carbon*, PhD thesis, University of Pretoria (2019).

[Jon37] J.E. Lennard-Jones, *The migration and aggregation of atoms on solid surfaces*, Proceedings of the Physical Society (1926-1948), 49. (1937) 140.

[Ken19] M.F. Kenari, *Diffusion of implanted europium in glassy carbon*, PhD thesis, University of Pretoria (2019).

[Kum08] S.P. Kumar, *Diffusion barriers in semiconductor devices/circuits*, William Andrew, Inc. (2008) 239–281.

[Lau03] T. Laurila, J. Molarius, *Reactive phase formation in thin film metal/metal and metal/silicon diffusion couples*, Critical reviews in solid state and materials sciences, 2003.

[Mal17] J.B. Malherbe, P.A. Selyshchev, O.S. Odutemowo, C.C. Theron, E.G. Njoroge, D.F. Langa, T.T. Hlatshwayo, *Diffusion of a mono-energetic implanted species with a Gaussian profile*, Nucl. Instr. Methods. Phys. Res. B 406 (2017) 708.

[Mal21] J.B. Malherbe, O.S. Odutemowo, C.C. Theron, E. Wendler, *Diffusion of strontium implanted in glassy carbon*, Proceedings of the Royal Society A. 477 (2021) 20200797.

[Mio01] A. Miotello, G. D. Marchi, G. Mattei, P. Mazzoldi, C. Sada, *Clustering of gold atoms in ion-implanted silica after thermal annealing in different atmospheres*, Phys. Rev. B 63 (2001) 075409.

[Poa78] J.M. Poate, K.N. Tu and J.W. Mayer, *Thin films-interdiffusion and reactions*, John Wiley, USA. (1978) 578.

[Res14] V. Resta, G. Quarta, L. Maruccio, L. Calcagnile, *Copper ion implantation of polycarbonate matrices: Morphological and structural properties*, Nucl. Instrum. Meth. Phys. Res. B 331 (2014) 187-190.

[She89] P. Shewmon, *Diffusion in solid*, The Minerals, Metals and Materials Soc., USA. (1989).

[Woo93] R.A. Wood, P.D. Townsend, N.D. Skelland, D.E. Hole, J. Barton, C.N. Afonso, *Annealing of ion implanted silver colloids in glass*, J. Appl. Phys. 74 (1993) 5754–5756.

[Www1] https://www.nde-ed.org/Physics/Materials/Structure/bonds.xhtml. (Visited on 19/10/2019).

CHAPTER 5

ANALYTICAL TECHNIQUES

In this chapter, the analysis techniques used in this study were extensively discussed. The structural changes in pristine glassy carbon due to ruthenium implantation and annealing were investigated by scanning electron microscopy (SEM), atomic force microscopy (AFM), X-ray diffractometer (XRD), and Raman spectroscopy. Moreover, Rutherford backscattering spectroscopy (RBS) was used to monitor the migration of ruthenium implanted in glassy carbon. The main techniques used in this thesis are discussed in depth in sections 5.1, 5.2, 5.3, 5.4 and 5.5.

5.1 Rutherford Backscattering Spectroscopy (RBS)

To prove Rutherford's proposed model of the atom [Rut12], Rutherford backscattering was used for the first time in 1913. After the Second World War, nuclear physicists applied RBS using particle accelerators to identify contaminants in their samples. The backscattered ions from target atoms appeared as a “parasitic” effect in the nuclear reaction particle spectra [Tol49], [Gro84]. The elemental composition of lunar soil samples was analyzed by Turkevich *et al.* [Tur68] in 1968 using an alpha-scattering particle experiment. In Rutherford backscattering analysis, the element's atomic mass and their distribution in depth can be determined based on the detected energy from backscattered particles [Per87]. Moreover, RBS is highly sensitive and can be used to study the composition of solid surfaces.

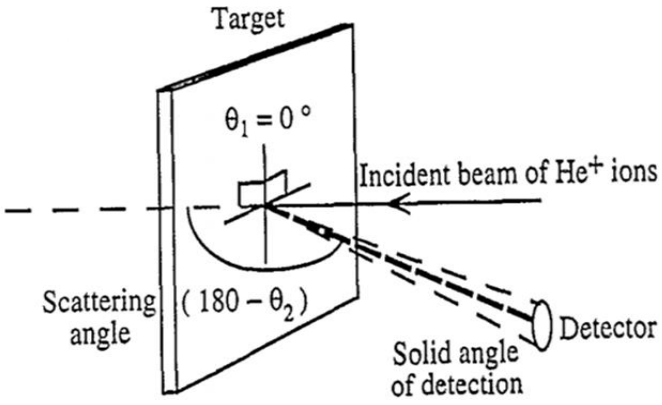

Figure 5.1: *Geometry of the RBS experiment [Gol96].*

5.1.1 Components of Rutherford Backscattering Spectroscopy

Three systems are involved in Rutherford backscattering spectroscopy: an accelerator, a scattering chamber, and a detector. The main purpose of an accelerator is to generate charged particles and accelerate them. An RF-source (i.e., radio-frequency ion source) generates charged particles (He^+ ions in this study were used) in the accelerator, which are then accelerated to high energies by applying a huge potential difference across the accelerator pipe – see Figure 5.2. In this study, RBS measurements were performed using the Van de Graaff accelerator at the University of Pretoria. In 1929, Van de Graaff developed the Van de Graaff accelerator. The accelerator builds up a large potential difference on a smooth conductor surface and maintains it. During this process, positive static charges are continuously transferred from a moving belt to the belt surface, as illustrated in Figure 5.2. Usually, the belt in the Van de Graaff accelerator is made of silk or another high-dielectric material. The difference in the electric voltage between the high-voltage supply and ground accelerates ions from the source to the target [Chu78]. By applying a potential difference of 2.7 MeV to the accelerator tube of the Van de Graaff accelerator (see Figure 5.2), charged particles (He^+) with energies of 1.4 and 1.6 MeV were produced.

By using a dipole magnet, the charged particles generated by the Van de Graaff accelerator will be separated based on their mass and energy, and the ions are deflected either to beamline 1 (the top beamline) or beamline 2 (the bottom beamline) as shown in Figure 5.3. In order to produce a monochromatic beam (consisting of one species, helium ions, with a specific energy), a dipole magnet was used here. In the scattering chamber at the end of beamline 1, the temperature was lower than room temperature, while in the scattering chamber at the end of beamline 2, it was 25 ˚C. In this study the scattering chamber at the end of beamline 2 was used.

Moreover, the ion beam is focused and guided into a chamber using the slits shown in Figure 5.3. The beam is first shaped into a specific size by a collimator inside the chamber, as shown in Figure 5.4 (a) (i.e., collimator size affects ion beam size). A stainless-steel sample holder was used to hold samples in the chamber, which was connected to a three-axis goniometer with 0.02˚ precision in each angle setting – see Figure 5.4 (a). Inelastic interactions between the He^+ ions and target atoms can generate secondary electrons, which can falsify measurements. In order to suppress secondary electrons, a ring-shaped electrode with a negative voltage of 200 V was placed in front of the target.

Using a Si surface barrier detector with a reverse bias of 40 V, backscattered alpha particles were detected. Through the preamplifier, the output charge signal received from the detector is integrated into a voltage signal proportionate to the energy of the backscattered ions. An amplifier was used to amplify the voltage signal. Then, an analog-to-digital converter (ADC) inside a multi-channel analyzer (MCA) was used to digitize the voltage signal and store it in the computer connected to the MCA – see Figure 5.4 (b). The outputs from a multi-channel analyzer are the number of backscattered ions versus channel number spectrum. The channel number is proportional to the backscattered energy, while the yield is the number of backscattered particles detected with a Si surface barrier detector at 165° (in our experimental set-up).

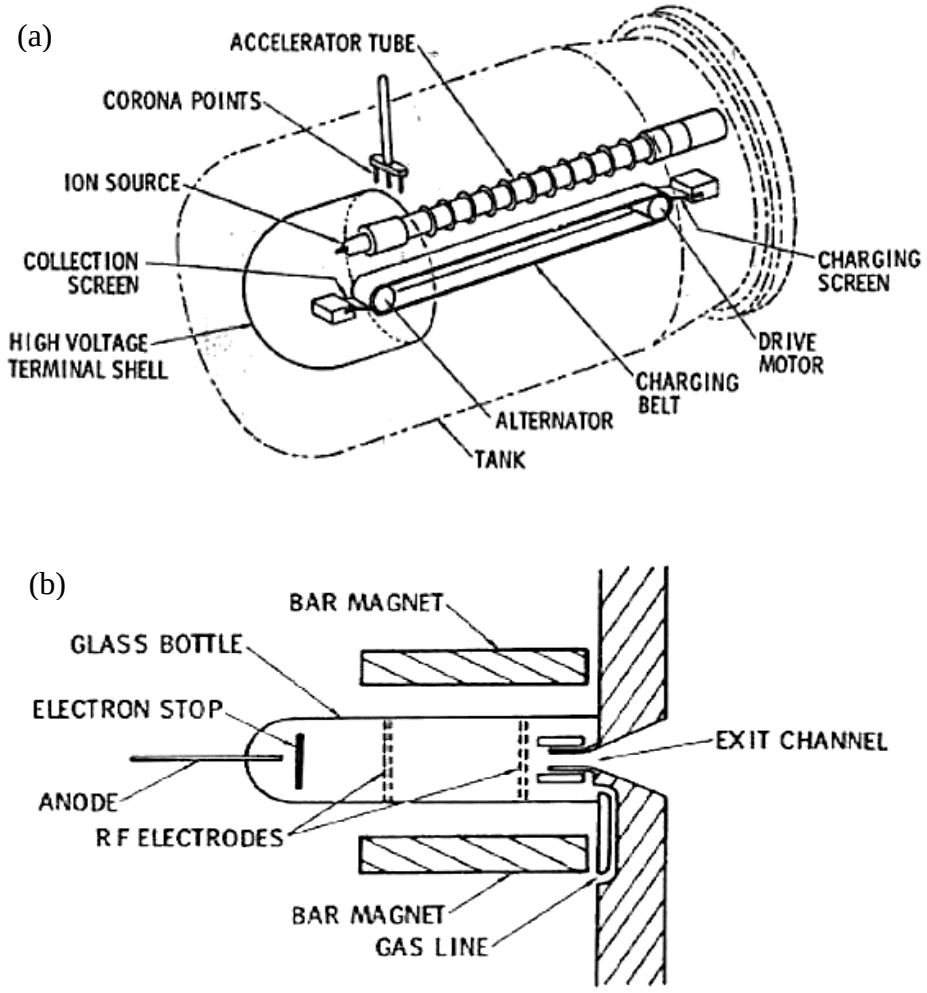

Figure 5.2: *Schematic diagram of a Van der Graaff accelerator (a) and a radio-frequency ion source (b). Taken from [Chu78].*

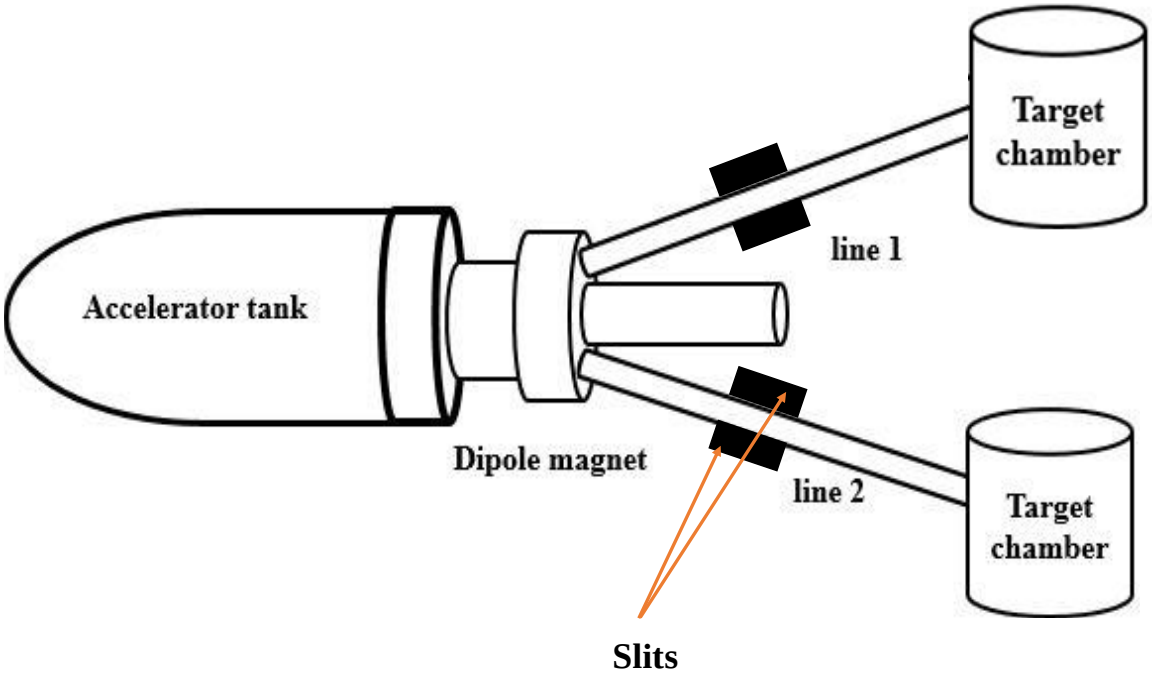

Figure 5.3: *A schematic diagram showing the Van de Graaff accelerator and beam lines at the University of Pretoria.*

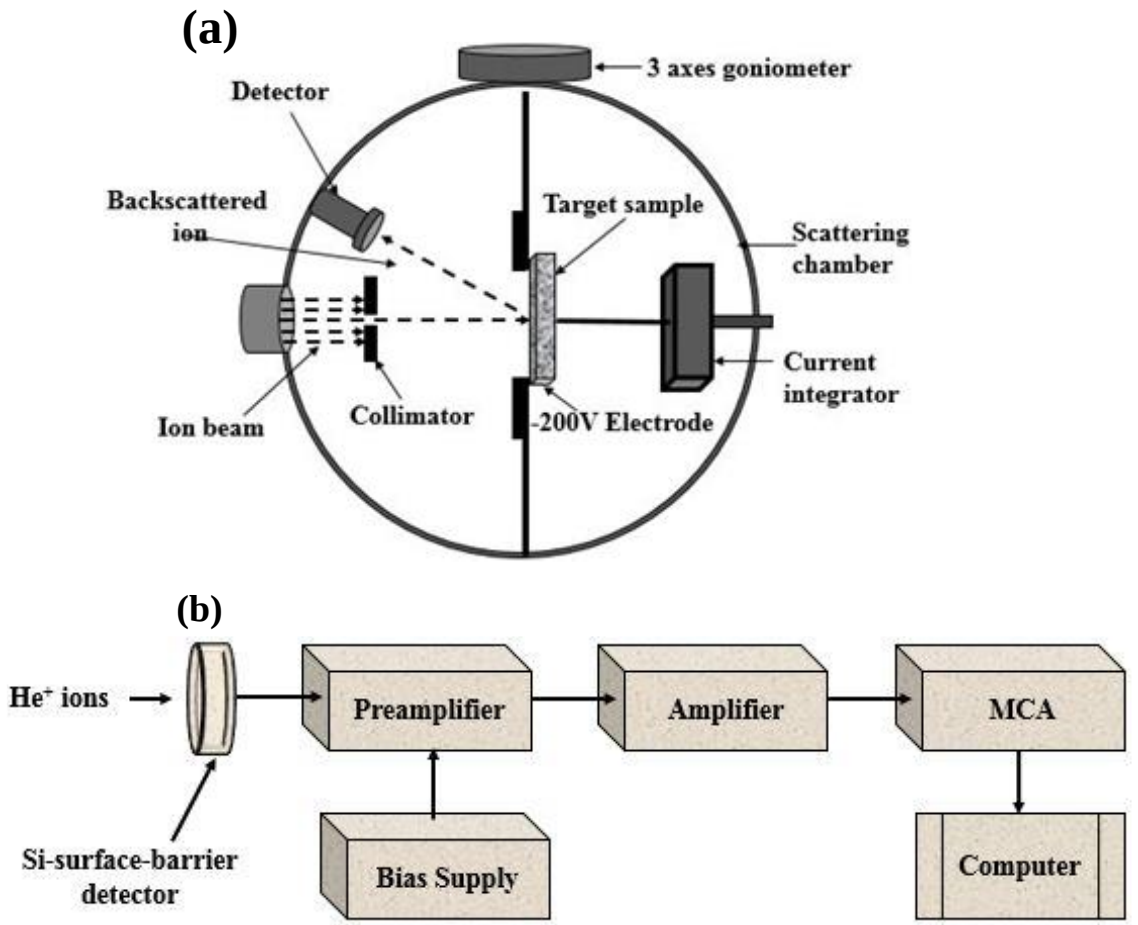

Figure 5.4: (a) *A schematic diagram showing the side view of the scattering chamber and (b) detector system for the University of Pretoria's Van de Graaff accelerator.*

5.1.2 Kinematic Factor

The kinetic factor (*K*) describes the transfer of energy from the incident projectile ion (alpha particle) to the target atom during the elastic collisions. In this case (i.e., elastic collisions), the conservation of energy and momentum can be used to describe this process [Miz12, Chu78, Gro84]. Using the conservation of momentum and energy, the backscattered particle (E_1) can be calculated from a classical two-body elastic collision (as shown in Figure 5.5) giving:

$$E_1 = K \times E_0 = \left[\frac{M_1 \cos\theta \pm \sqrt{\left(M_2^2 - M_1^2 \sin^2\theta\right)}}{M_1 + M_2}\right]^2 \times E_0 \qquad 5.1$$

where E_0 and E_1 are the energies of the incident and backscattered particles, respectively, M_1 and M_2 are the atomic masses of the incident particles and the target atom, and θ is the scattering angle shown in Figure. 5.5. In Equation 5.1, if the mass of the incident particles (M_1) is less than the mass of the target atom (M_2), the plus sign is taken. However, the minus sign will be used when $M_1 > M_2$. In our case, the mass of the incident particles (helium ions) was much lighter than the mass of the target atoms (i.e., carbon and ruthenium). Therefore, the plus sign was taken.

The kinetic factor (K) and the energy of the incident beam (E_0) can be used to estimate the energy of the backscattered particles (E_1). Moreover, K can be used to calibrate the RBS spectrum [Chu78]. From Equation 5.1 above, the mass of an unknown target atom can be determined from the measured energy E_1, thereby identifying the target atoms [Chu78]. In general, the mass of the target atoms can influence the kinematic factor, as K increases when the target atoms have heavy masses. As a result, the mass separation on the RBS energy spectrum decreases when mass increases.

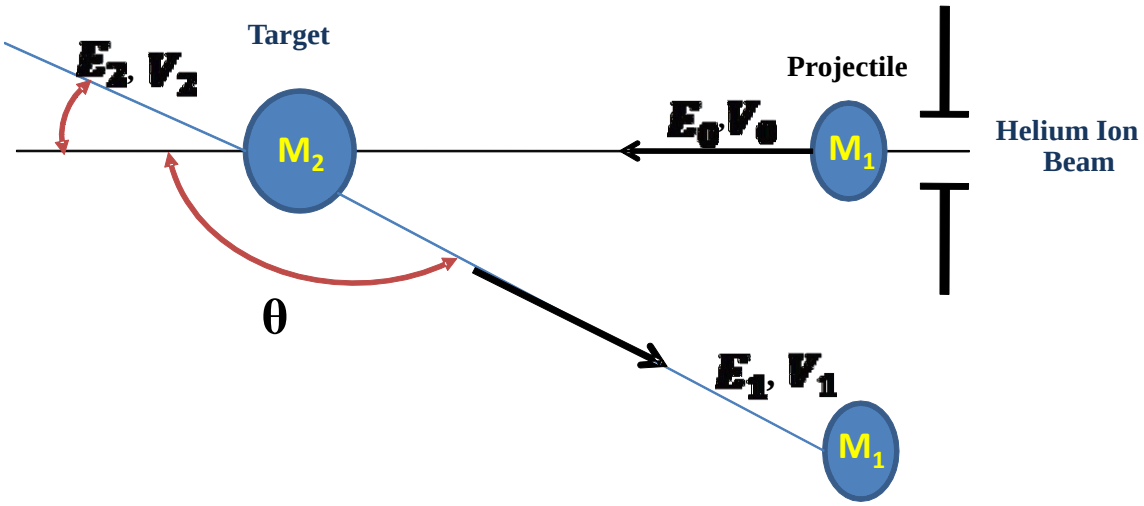

Figure 5.5: *A typical schematic of scattering between projectile and target atom.*

5.1.3 Scattering Cross Section (σ)

Generally, incident projectiles backscatter from a target at different angles. However, there is a small fraction of backscattered projectiles that can be detected at a certain angle, θ. In our RBS set-up, only backscattered projectiles at angle 165 (with respect to the incoming

beam) would be detected. In order to calculate the differential cross section ($d\sigma/d\Omega$) for scattering, the number of particles that backscattered into a solid angle ($d\Omega$) and the number of incident particles per unit area must be considered. Using the laboratory frame of reference, the differential cross section for scattering of a projectile into a solid angle ($d\Omega$) is given by [Chu78, Gro84]:

$$\frac{d\sigma}{d\Omega} = \left(\frac{Z_1 Z_2 e^2}{4E_0}\right)^2 . \frac{4\left[\left(M_2^2 - M_1^2 sin^2\theta\right)^{\frac{1}{2}} + M_2 \cos\theta\right]^2}{M_2 sin^4\theta \left(M_2^2 - M_1^2 sin^2\theta\right)^{\frac{1}{2}}} \qquad 5.2$$

where Z_1 and Z_2 are the atomic numbers of the projectile and target atoms, respectively, M_1 and M_2 are the masses of the projectile and target atoms, E_o is the energy of the projectile before scattering, θ is the backscattering angle and e is the electron charge.

The differential cross section for any projectile (i.e., $d\sigma/d\Omega$) is proportional to Z_2^2, so the projectile scatters more efficiently from heavy atoms than light atoms in the target. As a result, the RBS is more sensitive to heavy elements than to light elements. Since E_o is inversely proportional to the differential cross section, the yield of backscattered particles will increase if the energy of the bombardment ions decreases. The total number of helium particles backscattered from the target (i.e., detected by the Si detector) can be calculated as follows:

$$A = \sigma\, \Omega\, .\, Q\, .\, N \qquad 5.3$$

where A is the particles detected by the detector, Q is the total number of incident projectiles, σ is the differential cross section, **Ω** is the solid angle of the detector, and N is the number of target atoms per unit area. Since the numbers of incident (Q) and detected particles (A) were measured with RBS, and σ and **Ω** are known, then the number of target atoms per unit area (N) can be determined from Equation 5.3.

5.1.4 Depth Profiling

As illustrated in Figure 5.6, depth scaling describes the relationship between the energy of alpha particles backscattered from the target surface and from depth x inside the target. KE_o is the energy of the alpha particles backscattered from the surface of the target, where E_0 is the energy of the incident beam, while E is the initial energy of the alpha particle at depth x. The

energy of the particles backscattered at depth *x* (i.e., *E* – see Figure 5.6) is less than the initial energy of the incident particles (i.e., E_0) because they lose energy on their path from the target surface to depth *x*. In addition, the particles that backscatter at depth *x* lose energy on their way out of the target. From Figure 5.6, $x/cos\Theta_1$ and $x/cos\Theta_2$ represent the length of the inward path and the outward path of the particles respectively. According to [Chu78] [Wan09], the energy of the backscattered alpha particle at depth *x* can be calculated by assuming that the energy loss (*dE/dx*) is constant along each path:

$$KE_0 - E_1 = \left[\left(\frac{K\,dE}{cos\theta_1\,dx}\right)_{in} + \left(\frac{K\,dE}{cos\theta_2\,dx}\right)_{out}\right] x \qquad 5.4$$

where E_1 and KE_o are the energies of the particles backscattered from the atom at depth *x* and from the atom at the target surface, respectively. Taking ΔE as the energy difference between E_1 and KE_o, then:

$$\Delta E = KE_0 - E_1 \qquad 5.5$$

Equation above can be written as follows:

$$\Delta E = [S]x \qquad 5.6$$

where [S] is the energy loss factor, which indicates how energy and depth are related to one another. As a result, a measured energy spectrum can be directly converted into a depth scale by using the energy loss factor, S.

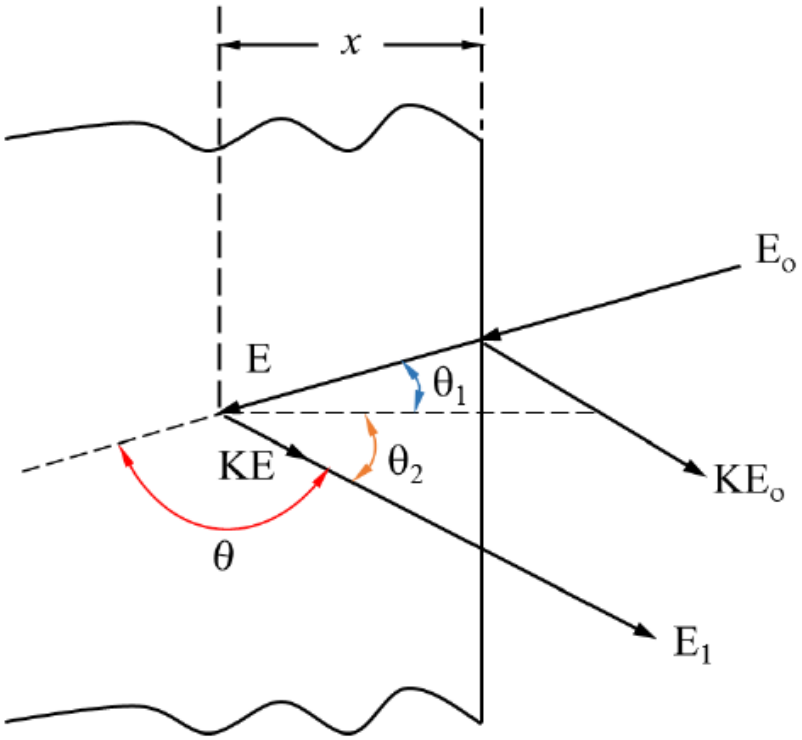

Figure 5.6: *An illustration of alpha particles backscattering and energy loss from depth x [Chu78].*

5.1.5 Depth Resolution

Depth resolution is defined as the minimum detectable in-depth difference (δx) that can be calculated as a function of the minimum detectable scattering particle energy difference, (δE). Due to the fact that the energy straggling increases as the ions penetrate deeper into the sample, the depth resolution is better near the surface while it is degraded at a deeper layer because of the energy straggling [Jey09]. However, if the energy loss factor [S] is increased, a better depth resolution can be achieved. This is achieved by tilting the sample normal relative to the incoming beam (i.e., increasing θ_1 and/or θ_2). This increases the path length required to reach a given depth in the sample (measured perpendicular to the surface). As a result, the scattered particles have a more significant energy difference for the same depth difference [Wan09].

5.2 Raman Spectroscopy

In Raman spectroscopy, the phenomenon of inelastic scattering of monochromatic light is used to determine the properties of materials. To generate light for Raman spectroscopy, a laser light source is used. Generally, when incident light interacts with molecules, photons with energy E_o can be scattered at the same energy (i.e., elastic scattering), reflected, or transmitted [Gra89]. The Raman Effect occurs when some incident photons scatter at optical frequencies different from their incident energies E_o (i.e., inelastic scattering).

Due to the inelastic interaction between monochromatic light and the target, the frequency of the scattered photons can be shifted up or down (i.e., have higher or lower frequencies than their initial frequency). Through this shifting, the Raman spectrum provides information about the rotational, vibrational and electronic energy of a molecule or crystal structure [Fer03, Lew01]. Accordingly, Raman spectra will vary according to the molecular structure of the material. In addition to studying different types of materials (solid, liquid and gaseous), Raman spectroscopy can also be used to probe the molecular structure and any changes that occur in the material. Therefore, Raman spectroscopy was used to study the structure of glassy carbon before and after ion implantation and annealing.

There are three types of scattering of laser light from a substance, namely Stokes scattering, anti-Stokes scattering and Rayleigh scattering as shown in Figure 5.7. Rayleigh scattering, which is a strong elastic scattering, has the same frequency as the incident beam (ν_0), while Stokes and anti-Stokes scattering are inelastic. The Stokes and anti-Stokes scattering has frequencies of ($\nu_0 - \nu_m$) and ($\nu_0 + \nu_m$) respectively - see Figure (5.7), where ν_0 is the frequency of the incident photon and ν_m is the vibrational frequency of a molecule. Consequently, in Raman spectroscopy, vibrational frequency (ν_m) can be measured as a shift from incident beam frequency (ν_0).

The four major components of a modern Raman instrument are: 1) the excitation source (laser), 2) the illumination system for the sample and the optics for collecting the light, 3) the wavelength selector (spectrophotometer or filter) and 4) the detector (array, CCD or PMT) [Jia11]. The most common laser beams used to illuminate samples are ultraviolet (UV), visible (VIS) or near infrared (NIR). The Raman spectrum of a sample is obtained by collecting scattered light through a lens and passing it through an interference filter or spectrophotometer.

Since Raman scattering is weak, it can be difficult to distinguish it from Rayleigh scattering. To increase Raman scattering sensitivity, highly sensitive multichannel detectors such as Charge Coupled Devices (CCD) are applied. Also, notch filters are used to enhance Raman scattering sensitivity. Using notch filters, Stokes and anti-Stokes Raman signals are transmitted while Rayleigh scattering is prevented. Figure 5.8 illustrates the Raman setup schematically.

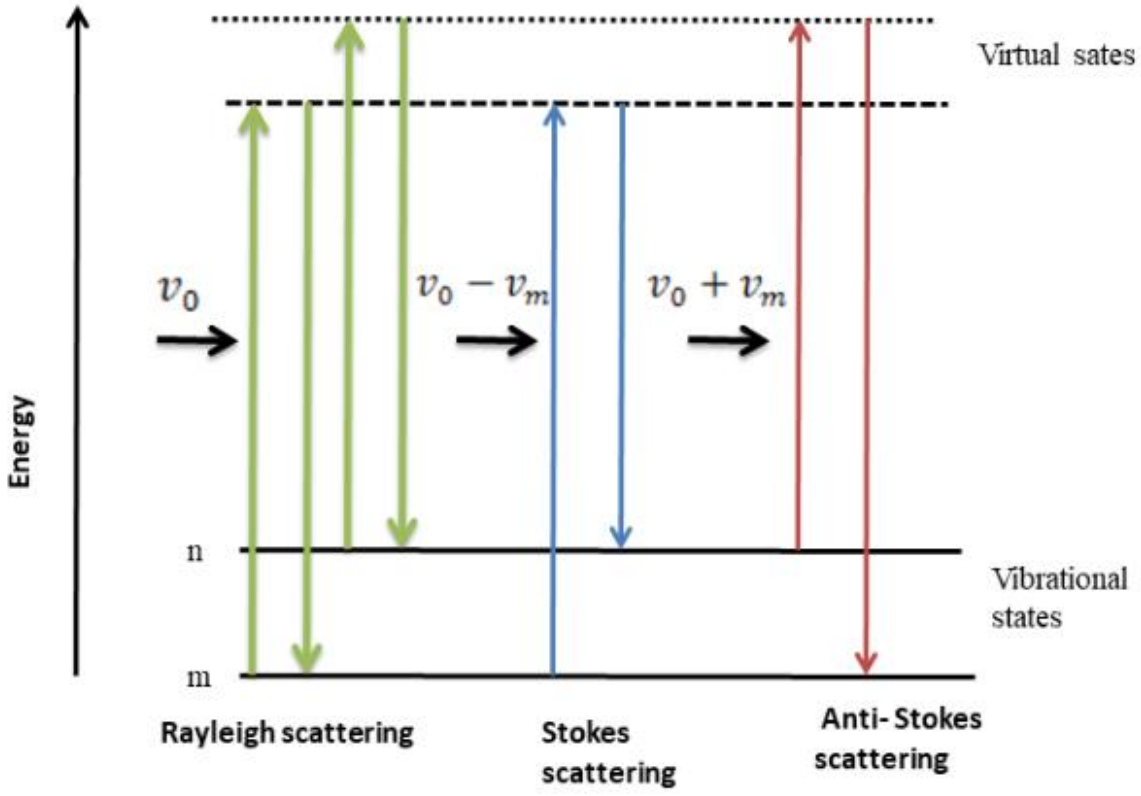

Figure 5.7: *The three types of laser scattering. Taken from [Odu17].*

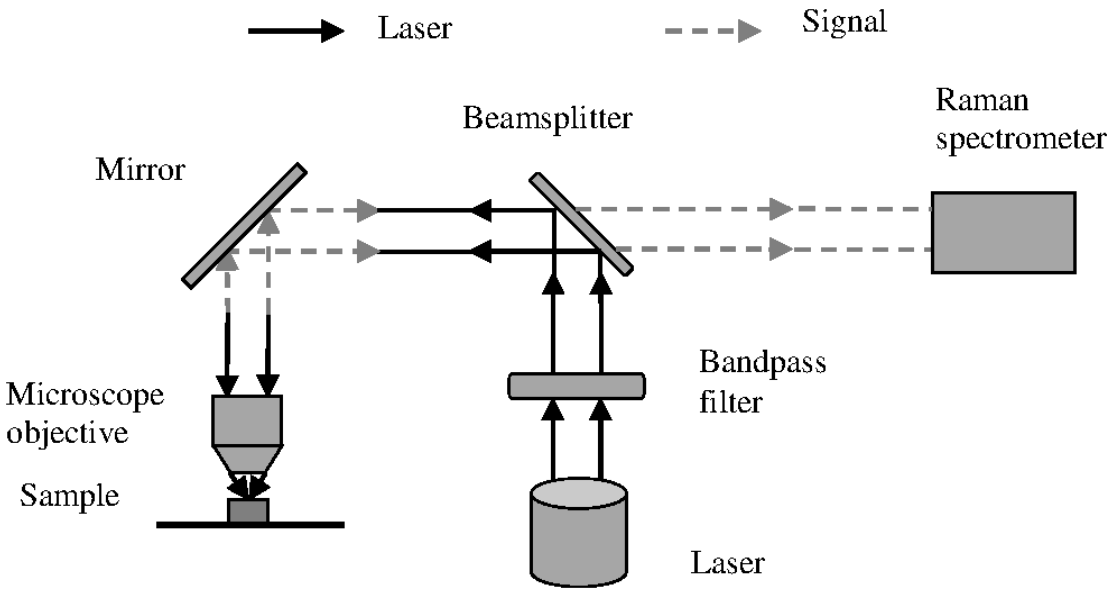

Figure 5.8: *Schematic diagram showing the different components of a Raman instrument. Taken from [Odu17].*

The Raman analysis was performed using a T64000 series II triple spectrometer from HORIBA Scientific, Jobin Yvon Technology. A coherent Innova® 70C series Ar+ laser line with a wavelength of 514.3 nm, a spot size of 2 µm and a resolution of 2 cm^{-1} was used in the range of 200 cm^{-1} - 1800 cm^{-1}. A backscattering configuration was used, using an Olympus microscope (LD 50x objective) with 1.7 mW laser power. The Raman spectra were recorded under these conditions using an integrated triple spectrometer in the double subtractive mode, which rejects Rayleigh scattering, and disperses the light onto a Symphony CCD detector (cooled in liquid nitrogen). The Raman spectra were then normalized to have the same scale. In chapter 7, Raman spectra of glassy carbon before and after ion implantation and annealing are presented.

5.3 Scanning Electron Microscopy (SEM)

The scanning electron microscope (SEM) is a microscope that creates an image of an object on a very small scale by using electrons rather than light [Zho07]. SEM creates a highly magnified image of a specimen by using a beam of electrons focused on it. SEM can be used

for a variety of applications, including analyzing thin film surface morphology and microstructural evolution.

Inelastic and elastic scatterings are usually caused by interactions between incident electrons and specimen electrons or atoms. By transferring their energies to the target, some incident electrons scatter with reduced energy (i.e., inelastic scattering) [Zho07]. Moreover, a backscattered electron (BSE) is a result of the elastic collision between the incident beam and the atoms of the target. Elastic scattering occurs when incident electrons are deflected by the atomic nucleus of the specimen. BSEs are reflected off the target sample with an energy similar to the initial energy of the incident electrons. Therefore, BSEs are high-energy electrons as shown in Figure 5.9. Compared to secondary electrons (SE), BSE has a higher energy and provides information from deeper regions of a sample.

In an inelastic collision, incoming electrons collide with target atoms, generating secondary electrons (SEs) which then create more secondary electrons. Compared to BSEs, these SEs are less energetic [Haf07]. Signals from SEs can be used to study the surface topography of samples. SEs with low energy can exit samples when they are near the surface, whereas other SEs are absorbed by the sample because of their low energy [Ste08]. Therefore, only SEs that are located near the surface can be detected. SEs and BES are not the only signals generated by the incident electrons; characteristic X-rays and Auger electrons can also be produced (see Figure 5.9).

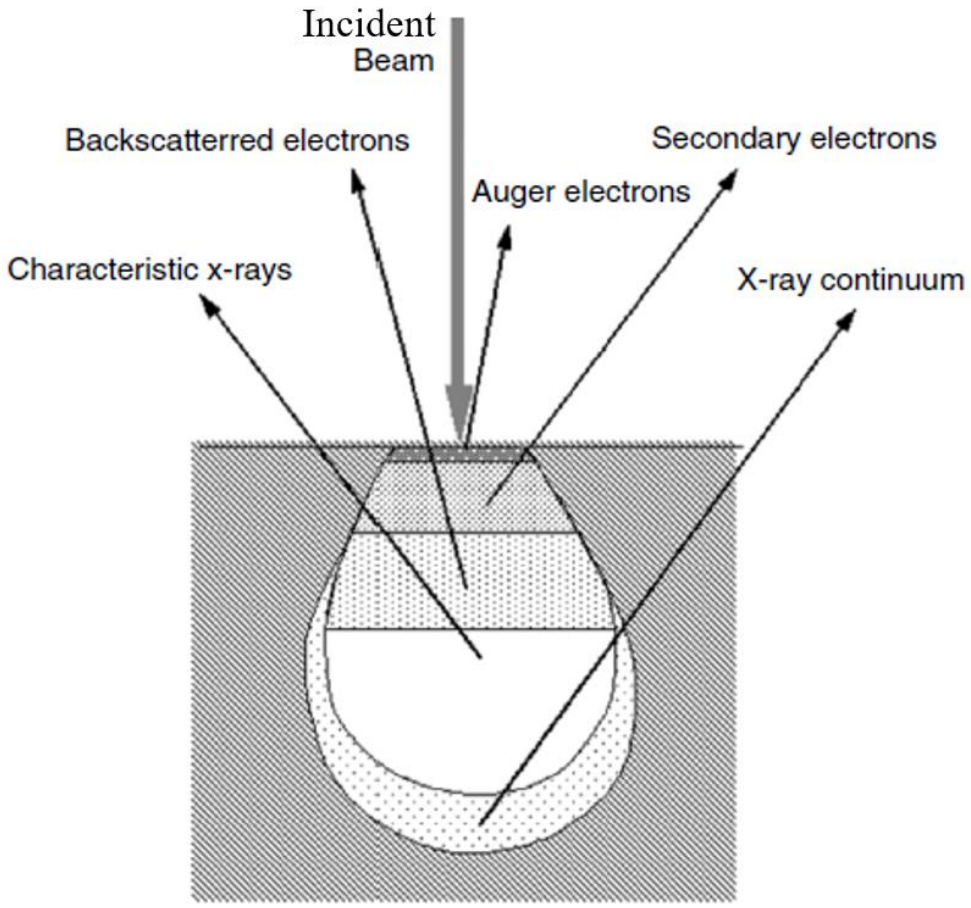

Figure 5.9: *Diagram showing particles and rays emitted when an energized electron strikes a sample [Zho07].*

5.3.1 SEM Configuration

A conventional SEM electron column is shown in Figure 5.10. At the top of the column, the primary electrons are generated by an electron gun. This gun can produce electrons with energy ranging from 0.1 to 30 keV [Zho07, Ege05]. The electron gun in a modern SEM system must create a stable electron beam that has a small spot size, adjustable energy, and small energy dispersion. Several electron guns have been used in many SEM systems. In the first generation of SEMs, tungsten or lanthanum hexaboride (LaB6) cathodes were commonly used, but in modern systems, field emission sources have been used. Moreover, SEM measurements were performed in a moderate vacuum. This allowed the generated electrons to move freely from the electron gun to the sample and then to the detectors after scattering from the sample [Pos94]. An electron probe is created on the sample surface by focusing the electron beam (into

a beam spot smaller than 10 nm in diameter) using scanning coils, which consist of several electromagnetic lenses. Typically, the depth of the electron beam interaction with the specimen is approximately 1 µm, although this can vary depending on the electron energy and the properties of the specimen [Nix71].

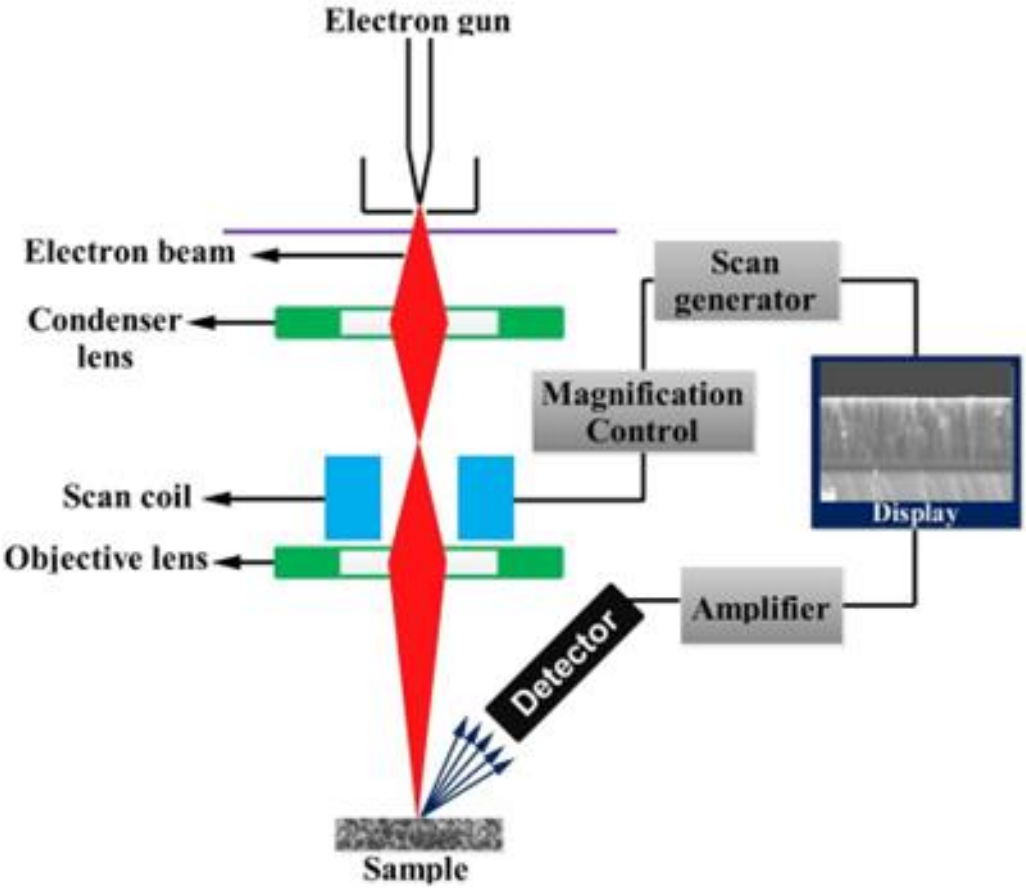

Figure 5.10: *Schematic diagram of a scanning electron microscope.*

5.3.2 SEM Setup and Measurement

A typical SEM consists of an electron column, scanning system, detectors, display, electronic controls and a vacuum system. The surface morphology of the samples was examined using a Zeiss Ultra 55 field emission scanning electron microscope equipped with a field emission electron gun (FEG). The FEG gun, which is mounted on this optical instrument, is composed of sharp tip tungsten wires with a radius of less than 100 nanometres. Electrons are emitted from FEG when the electric field intensity at the tip reaches 10 V/nm [Hal10]. Several detectors, such as SE, BE and in-lens SE detectors, can be used to detect electrons

during SEM measurements. In this study, SE-in-lens detector was used. SEM images of sample surfaces were taken at various magnifications. A beam energy of 2 kV was used in order to concentrate on the near surface area of the samples.

5.4 X-ray Diffraction (XRD)

The X-ray diffraction technique is a noninvasive analytical technique that can reveal information about the chemical composition, physical properties and crystallographic structure of materials and thin films. This technique measures the scattered intensity of X-rays hitting a sample by adjusting the incident and scattering angles and the wavelength of the incident X-rays. X-rays are a form of electromagnetic radiation with a very short wavelength compared to light. Moreover, quantitative and qualitative analyses can be performed using this technique (i.e., the X-ray diffraction technique) [Bir06]. In quantitative analysis, the structural properties and phase proportions of a specimen are determined numerically. In qualitative analysis, the phases are identified by comparing the data collected from our samples with reference patterns.

When electrons with energies between 10 and 40 keV [Lan96] interact with metal targets, X-ray photons are produced. An X-ray photon's maximum energy depends on the incident energy of the electrons hitting the anode (i.e., the metal target). Most of the anodes used to generate X-rays are made of metals such as Cu, Cr, Fe, Co and Mo [Lan96]. In most X-ray tubes, anodes are made of Cu, which emits (Kα) radiation with a wavelength of 1.5406 Å [Hol97]. An X-ray beam of wavelength λ focused at an angle θ onto crystalline matter may undergo diffraction if the following condition is met: the distance travelled by the X-rays reflected from successive planes differs by an integer multiple of the wavelength of the radiation (see Figure 6.11).

X-rays diffracted by the crystal lattice can constructively interfere due to the regularly repeated arrangement of the atoms in the crystal lattice. Sir William Lawrence Bragg proposed these conditions in 1912, which became known as Bragg's law [Lan96]. Figure 6.11 shows that the ray BAY leads ray BA'Y by the amount of path-length (nλ) [Klu74], as defined geometrically by the following:

$$n\lambda = BA' + A'D = d\ sin\theta + d\ sin\theta \qquad 5.7$$

Equation 5.7 can be written as follows (which is Bragg's diffraction law) [Lan96, Klu74]:

$$n\lambda = 2d\ sin\theta \qquad 5.8$$

where n is a positive integer, λ, d and θ are the wavelength of the X-ray, the spacing between crystal planes and the diffraction angle from the plane (hkl), respectively [Nau00]. Since the XRD experiments are conducted at a fixed wavelength, Equation 5.8 can be used to calculate the d-spacing based on the measured diffraction angles. Moreover, the lattice parameter (a) of cubic crystalline materials is given by [Klu74]:

$$a = \frac{d_{hkl}}{\sqrt{h^2+k^2+l^2}} \qquad 5.9$$

where *hkl* are the Miller indices for the (*hkl*) plane. It is possible to determine the crystal structure of a material by using equations 5.8 and 5.9 if the peaks in the diffraction pattern are properly indexed.

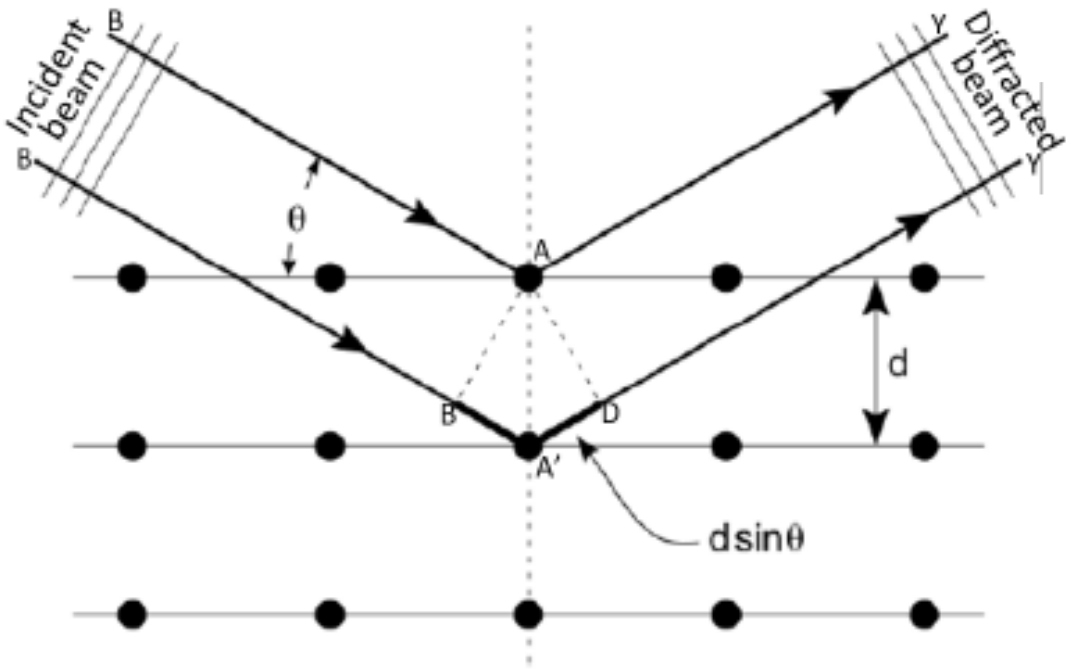

Figure 5.11: *Schematic of X-ray interaction with crystal planes. Adapted from [Klu74].*

5.4.1 Residual stress determination from XRD peak broadening

There are three major factors that influence peak broadening in XRD [Cul56]: strain in the material, crystallite size, and instrumental contributions to peak broadening. The measurement of crystal size from the broadening of XRD peaks was first proposed by Scherrer, where the Scherrer equation can be expressed as [Zha08]:

$$\mathrm{D} = \frac{\mathrm{K}\lambda}{\mathrm{B}\cos\theta} \qquad 5.10$$

Assume D is the crystal size, K is a dimensionless shape factor (values between 0.62 and 2.08), λ is the wavelength of the X-ray, B is the line broadening at the full width half maximum (FWHM) and θ is the Bragg angle. Nanoparticles can be measured by the Scherrer equation, but grains larger than 0.1 or 0.2 μm cannot be measured by this method. Because of a variety of factors, Scherrer's formula provides a lower bound on particle sizes. Apart from instrumental effects and crystallite size, other factors can also affect the width of a diffraction peak. The most significant factors include inhomogeneous strain and crystal lattice imperfections. Therefore, the Williamson-Hall equation assumes that the total broadening of the XRD peak is due to strain and crystallite size as shown below [Wil53]:

$$\beta_{total} = \beta_L + \beta_e \qquad 5.11$$

where β_{total} is the total broadening of the XRD peak, β_e and β_L are the broadening due to strain and crystal size respectively. The approximate formulae for size (Scherrer) broadening, β_L, and strain broadening, β_e, are shown in Equation 5.12 below:

$$\beta_L = \frac{k\lambda}{D\cos\theta}, \beta e = C_\epsilon tan\theta = C_\epsilon \frac{sin\theta}{cos\theta} \qquad 5.12$$

where D is the crystallite size, θ is the Bragg angle (in radians). For the strain broadening β_e, the C_ϵ is the amount of strain in the sample. Moreover, by substituting Equation 5.12 into Equation 5.11, then one gets:

$$\beta_{total} = \frac{k\lambda}{D\cos\theta} + C_\epsilon \frac{sin\theta}{cos\theta} \qquad 5.13$$

By multiplying Equation 5.13 by cosθ we get:

$$\beta_{total}\cos\theta = C_\epsilon sin\theta + \frac{k\lambda}{D} \qquad 5.14$$

Comparing Equation 5.14 to the standard equation for a straight line (m = slope; c = intercept), y = mx + c, one sees that by plotting $\beta_{total}\cos\theta$ versus $\sin\theta$ we obtain the strain (C_ε) component from the slope (m) and the crystal size (D) component from the intercept (c). Such a plot is known as a Williamson-Hall plot – see Figure 5.12. The strain in pristine glassy carbon after ruthenium implantation and annealing was calculated using Equation 5.14 and the results are presented in Chapter 7.

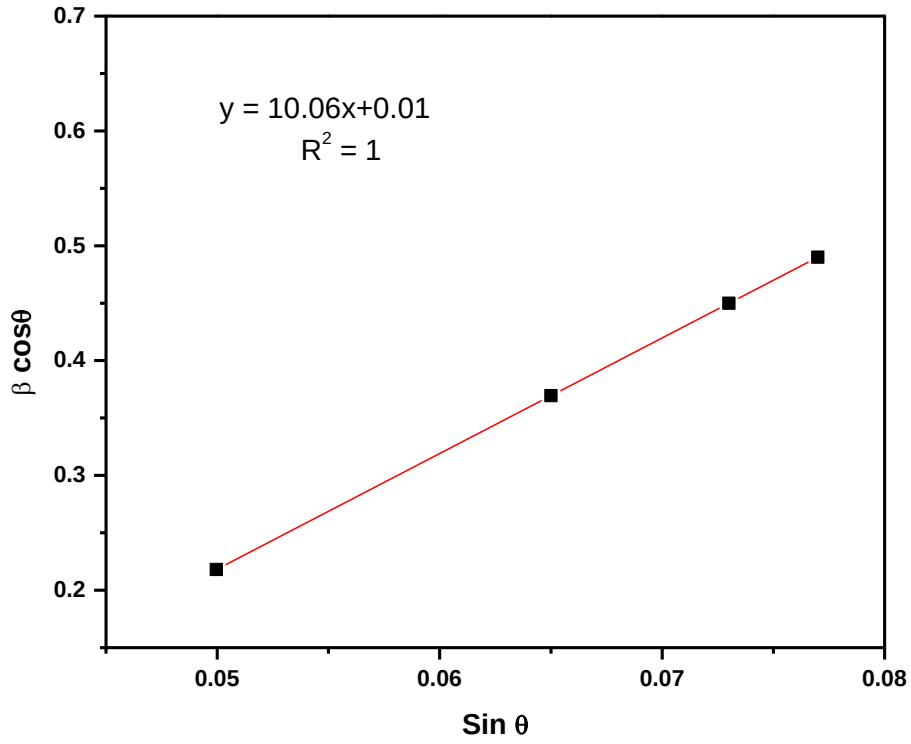

Figure 5.12: *Williamson-Hall plot.*

5.4.2 XRD setup and measurement

A database of XRD data provided by the Inorganic Crystalline Structure Database (ICSD) was used to identify crystalline phases found in our samples by comparing peak positions and relative intensities with those in the ICSD database. In addition to d-spacing and intensities of the peaks, ICSD provides information on hkl values, chemical formulas, cell dimensions, selected physical properties, and references [Ber83].

XRD was used to characterize the glassy carbon samples at the Radio-Analysis Laboratory of the South African Nuclear Energy Corporation (NECSA). Sample analysis was performed with Bruker D8 Discover equipment that uses a Cu (K_α) X-ray radiation source. A

two-theta step size of 0.03˚ and a dwell time of 240 s per frame (four frames) were applied during data collection. In this experiment, the incident X-ray beam was retained at 3˚ relative to the sample surface, while a goniometer rotated the detector from 22˚ to 120˚ two-theta as the diffraction pattern was collected. The collected data is presented and discussed in detail in Chapter 7.

5.5 Atomic Force Microscopy (AFM)

Atomic force microscopy (AFM) is used in surface science to determine surface topography at a high resolution of 1 nm [Bin86]. From thin films to organic cells, AFMs are widely used as nondestructive tools to investigate surface morphologies [Mar97]. The AFM characterizes surface morphology by exerting force on the surface atoms of the sample via its movable tip [Wic89].

In an AFM, the sharp tip is fixed to a spring cantilever. AFM works by the principle of interatomic potential [Jag05]. Interatomic potentials develop between the atoms of the AFM tip and the atoms of the sample surface when the AFM tip is brought very close (within interatomic separation distance) to the sample surface. The interatomic potential causes the cantilever to bounce up and down as the sharp tip moves across a rough sample surface (see Figure 5.13). As a result of measuring the cantilever deflections, topographic features of the sample surface can be mapped out. Using a laser and a detector, the force exerted between atoms on the sample surface and atoms on the AFM tip is measured. Moreover, by recording cantilever motion in the z-direction as a function of the sample's x and y positions, a 3D image can be created from the AFM [Jag05]. Besides providing surface morphology and grain size information, AFM analysis can provide quantitative roughness value as well.

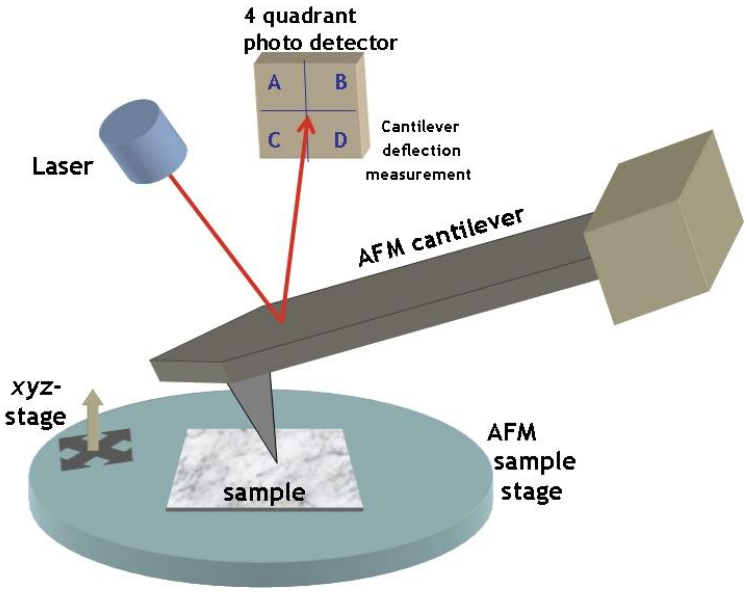

Figure 5.13: *A diagram of an atomic force microscopy.*

5.5.1 AFM setup and measurement

Glue was used to mount the samples on metal plates (i.e., sample holders) to do the AFM measurements. Dimension Icon AFM system was used to obtain AFM images. This system operates in contact mode and has a sharp nitride lever (SNL) probe with a spring constant of 0.30 N/m. AFM probes with tip radiuses of 2 nm and scan rates of 0.3 Hz are used for sample analysis. The resonance frequencies of the SNL probe range from 40 to 75 kHz. Furthermore, NanoScope Analysis (Bruker, USA) was used to analyze the AFM images obtained during the analysis of all samples.

References

[Ber83] G. Bergerhoff, R. Hundt, R. Sievers, I.D. Brown, *The inorganic crystal structure data base*, J. Chem. Inf. Comput. Sci., 23 (1983) 66-69.

[Bin86] G. Binnig, C.F. Quate, and C. Gerber, *Atomic force microscope*, Physical review letters, 56 (1986) 930–933.

[Bir06] M. Birkholz, *Thin film analysis by x-ray scattering*, John Wiley and Sons, New York, 2006.

[Chu78] W. Chu, J.W. Mayer, M. Nicolet, *Backscattering spectrometry*, Academic Press. (1978).

[Cul56] B.D. Cullity, S.R. Stock, *Elements of x-ray diffraction*, Addison-Wesley Publishing company Inc, Massachusetts, 1956.

[Ege05] R.F. Egerton, *Physical principles of electron microscopy*, Springer, New York, 2005.

[Fer03] J.R. Ferraro, K. Nakamoto, C.W. Brown, *Introductory Raman spectroscopy*, 2nd ed., Elsevier Science, USA, 2003.

[Gol96] F. Golgberg and E.J. Knystautas, *NiTi thin film characterization by Rutherford backscattering spectrometry*, Mater. Sci. Eng. B. 40 (1996) 185-189.

[Gra89] D.J. Gardiner, P.R. Graves, *Practical Raman spectroscopy*, Springer-Verlag, Berlin Heidelberg, 1989.

[Gro84] J.J. Grob, P. Siffert, *Rutherford Backscattering Spectroscopy (RBS)*, Progress in crystal growth and characterization, 1 (1984) 59–106.

[Haf07] B. Hafner, *Scanning electron microscopy primer, Characterization Facility*, University of Minnesota-Twin Cities, (2007) 1–29.

[Hal10] T.T. Hlatshwayo, *Diffusion of silver in 6H-SiC*, PhD thesis, University of Pretoria, 2010.

[Hol97] G. Holzer, M. Fritsch, M. Deutsch, J. Hartwig, E. Forster, *K(α 1, 2) and K(β 1, 3) x-ray emission lines of the 3 d transition metals*, Physical Review A, 56 (1997) 45–54.

[Jag05] R. Jagtap and A. Ambre, *Atomic force microscopy (AFM): Basics and its important applications for polymer characterization: An overview*, Journal of Polymer Materials, 22 (2005) 1–26.

[Jey09] C. Jeynes and N.P. Barradas, *Pitfalls in ion beam analysis*, Handbook of Modern Ion Beam Materials Analysis, Materials Research Society, 15 (2009) 347-383.

[Jia11] I. Jain and G. Agarwal, *Ion beam induced surface and interface engineering*, Surf. Sci. Rep. 66 (2011) 77- 172.

[Klu74] H.P. Klug, L.E. Alexander, *X-ray diffraction procedures: For polycrystalline and amorphous materials*, John Wiley and Sons, New York, 1974.

[Lan96] J.I. Langford, D. Louer, *Powder diffraction*, Reports on Progress in Physics, vol. 59, no. 2, pp. 131–234, 1996.

[Lew01] I.R. Lewis, H.G.M. Edwards, *Handbook of Raman spectroscopy*, Marcel Dekker, Inc., New York, 2001.

[Mar97] N. Martin, C. Rousselot, D. Rondot, F. Palmino,, R. Mercier, *Microstructure modification of amorphous titanium oxide thin films during annealing treatment*, Thin solid films, 300 (1997)113–121.

[Miz12] K. Mizohata, *Progress in elastic recoil detection analysis*, HELSINKI. (2012).

[Nau00] D. Naumann, R. Meyers, *Encyclopedia of analytical chemistry*, John Wiley and Sons, Chichester, UK (2000) 102–131.

[Nix71] W. Nixon, *The general principles of scanning electron microscopy*, Philosophical Transactions of the Royal Society, 261 (1971) 45–50.

[Odu17] O.S. Odutemowo, *Modification of glassy carbon under strontium ion implantation*, PhD thesis, University of Pretoria. (2017).

[Per87] J. Perriere, *Rutherford backscattering spectrometry*, Vacuum, 37 (1987) 429–432.

[Pos94] M.T. Postek, *Critical issues in scanning electron microscope metrology*, Journal of Research-National Institute of Standards and Technology, 99 (1994) 641–641.

[Rut12] E. Rutherford, *The scattering of α and β particles by matter and the structure of the atom*, Philosophical Magazine, 92 (2012) 379–398.
[Ste08] E.C. Stefanaki, *Electron microscopy: The basics*, *Physics of Advanced Materials*, Winter School, (2008) 1–11.

[Tol49] A.V. Tollestrup, W.A. Fowler, C.C. Lauritsen, *Energy release in beryllium and lithium reactions with protons*, California Institute of Technology, 1 (1949) 4–6.

[Tur68] A.L. Turkevich, J.H. Patterson, E.J. Franzgrot, *The chemical analysis of the lunar surface*, 56 (1968) 312–343.

[Wan09] Y. Wang, M. Nastasi, *Handbook of modern ion beam materials analysis*, 2nd ed, Materials Research Society, USA, 2009.

[Wic89] H.K. Wickramasinghe, *Scanned-probe microscopes*, Scientific American, 261 (1989) 98–105.

[Wil53] G.K. Williamson, W.H. Hall, *X-ray line broadening from filed aluminium and wolfram*, Acta Metall., 1 (1953) 22-31.

[www1] http://htw-germany.com/technology.php5?lang=en&nav0=2&nav1=16.

[Zha08] Y. Zhao, J. Zhang, *Microstrain and grain-size analysis from diffraction peak width and graphical derivation of high-pressure thermomechanics*, J. Appl. Crystallogr., 41 (2008) 1095–1108.

[Zho07] W. Zhou, Z. L. Wang, *Scanning microscopy for nanotechnology: Techniques and applications*, Springer science and business media, New York, 2007.

CHAPTER 6

EXPERIMENTAL PROCEDURE

In this study, ruthenium ions were implanted into SIGRADUR®G glassy carbon wafers at room temperature and 200˚C. The dimensions of the pre-implanted glassy carbon wafers were 50mm×10mm and 2mm thick. After implantation, the samples were cut into small pieces of 5mm×5mm in size, and then annealed in a vacuum tube furnace at temperatures ranging from 500˚C to 1300˚C. RBS and SIMS were used to investigate the migration behavior of ruthenium in glassy carbon before and after annealing. Moreover, Raman spectroscopy, XRD, AFM and SEM were used to investigate the structural changes and surface modifications of pristine glassy carbon samples after implantation and annealing.

6.1 Sample Preparation

SIGRADUR®G glassy carbon samples from Hochtemperatur-Werkstoffe (HTW), Germany were used in this study. The HTW Company produces two types of glassy carbon materials, SIGRADUR®G and SIGRADUR®K. SIGRADUR®G was chosen for this study due to its lower density, higher conductivity, higher corrosion resistance, and higher temperature resistance. The samples were mechanically polished with 1 μm and 0.25 μm diamond solutions, respectively, on an ATM Saphir 500 polisher. After polishing, the following methods were used to clean the samples: first an ultrasonic bath was used to wash the samples in an alkaline soap solution, then, the samples were transferred to beaker containing de-ionized water. By using de-ionized water, the soap solution was removed from the sample. However, in order to remove the de-ionized water from the samples, methanol was used to clean the samples for five minutes in an ultrasonic bath. In the final step, the samples were blown with nitrogen gas for a few minutes and then placed in an oven at 50˚C for an hour. This was done to remove volatile impurities from the surfaces of the glassy carbon samples.

6.2 Ion Implantation

After cleaning the pristine glassy carbon wafers, ruthenium ions were implanted into glassy carbon using a 200–20A2F ion implanter, located at iThemba LABS (Gauteng), South Africa. Glassy carbon samples were implanted with 150 keV ruthenium ions at room temperature to a fluence of 1×10^{16} ions/cm^2. Another set of samples was implanted under the same conditions, but at a higher temperature (i.e., 200 ˚C). The aim was to compare radiation damage introduced into glassy carbon during ruthenium implantation at room temperature and 200°C. Radiation damage usually affects the migration of implanted ions in glassy carbon [Odu20]. Therefore, the effect of radiation damage on the migration of ruthenium in glassy carbon was investigated as discussed in chapter 7.

As-implanted glassy carbon wafers were cut into 5mm×5mm pieces using a tungsten carbide (WC) cutter so that they could be placed in sample holders designed for RBS, XRD, AFM and SEM analysis. To remove dust particles and to avoid contamination of the cut samples, samples were washed again with de-ionized water and methanol. The cleaned samples were then annealed in vacuum furnaces as described below.

6.3 Annealing Systems

The annealing process in this study was conducted at both low and high temperatures using two different annealing systems. Isochronal annealing was done for all samples implanted at different temperatures (i.e., glassy carbon samples implanted at room temperature and 200 ˚C). Low annealing was performed in a quartz vacuum tube furnace, which has a maximum temperature of 1000°C. Figure 6.1 shows a schematic diagram of the annealing equipment. After placing the sample in the quartz tube, the quartz tube was evacuated to below 10^{-3} mbar using the fore pump, and then the turbo pump system was turned on. A turbo pump is used to create a high vacuum (up to 10^{-7} mbar) during the annealing process – see Figure 6.1. In order to measure the sample's temperature, a thermocouple was placed near the sample, and a computer program was used to monitor the temperature during the annealing period.

Prior to annealing, the oven was allowed to stabilize until the required annealing temperature was reached. The oven was moved over the quartz vacuum tube until the sample was near the center of the oven. As a result, the sample was able to reach the required

temperature quickly. However, the oven was pulled back at the end of the annealing time, and the sample was left to cool to room temperature. Following the completion of the annealing process, the sample was removed after the turbo pump and fore pump had been turned off and the turbo pump blades had ceased to rotate. It usually takes approximately an hour for the turbo pump blades to cease to spin completely. Using this quartz vacuum tube furnace, the samples were annealed at temperatures ranging from 500 °C to 1000 °C in 100 °C steps for 5 hours (i.e., annealing at low temperatures).

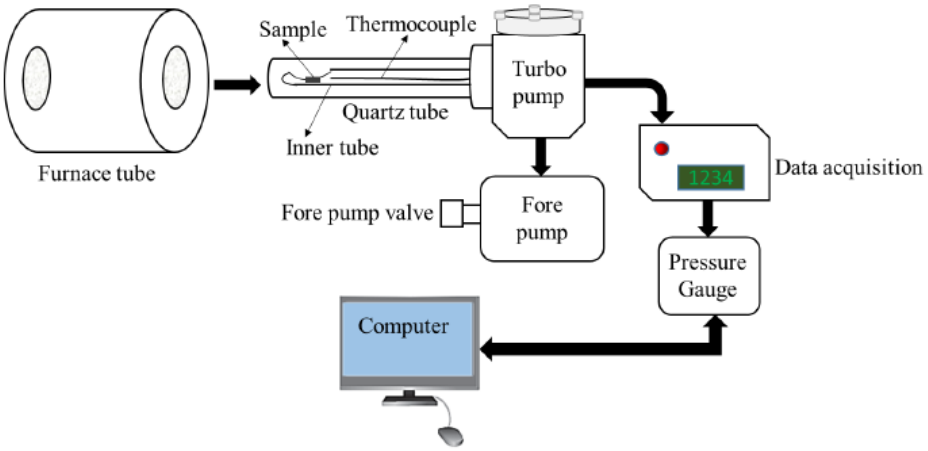

Figure 6.1: *Schematic diagram showing the annealing system used for the low-temperature annealing.*

During the high temperature annealing, the samples were annealed from 1000 °C to 1300 °C in steps of 100 °C for 5 hours. Glassy carbon crucibles were used to hold the samples during annealing. A computer-controlled high temperature vacuum graphite furnace (Webb®77) was used to conduct the annealing. A Eurotherm 2704 controller, connected to a thermocouple, controls the temperature during annealing, while the thermocouple was employed to measure the temperatures (i.e., which can measure temperatures up to 1475 °C) [Kuh15, Web06]. In Figure 6.2, a typical heating and cooling curve as a function of time are shown. Webb ovens have a nominal temperature accuracy of ±15 °C.

The Webb oven was evacuated to a pressure of 10^{-7} mbar before each annealing cycle. To reduce the amount of time spent pumping and to keep the maximum pressure during

annealing below 10^{-6} mbar, degassing was performed at 200°C for one hour before annealing at the required temperature. It was found that the degassing temperature overshoot from 200 °C to 300 °C – see Figure 6.2. This was due to the manufacturer's temperature control system, which caused a large current and fluctuation during initial degassing. The vacuum pressure increased from 10^{-7} to 10^{-5} mbar during the annealing process, due to the increased degassing caused by the high initial current. In addition, the oven was programmed to heat at a rate of 20 °C/min. Once the heating element was turned on, it heated up to the degassing temperature (i.e. 200 °C, see Figure 6.2). The current measured at the beginning of the heating process was approximately 28 A, but it later decreased to zero A due to overheating (i.e., 300 °C). After degassing, the current increased again up to 18 A so that the oven could reach the selected temperature for annealing (i.e. 1300 °C – see Figure 6.2). After the temperature in the oven reached 1300 °C, the current dropped to 8 A for 5 hours (during annealing time). At the end of the annealing process, the system was cooled down by turning off the current (zero A). In order to remove the samples from the oven, the turbo pump (i.e. high vacuum pump) was turned off after the oven had completely cooled down to room temperature, while the fore pump was still pumping. The fore pump was turned off and the pressure in the annealing chamber was raised to atmospheric pressure by leaking Argon gas into the chamber.

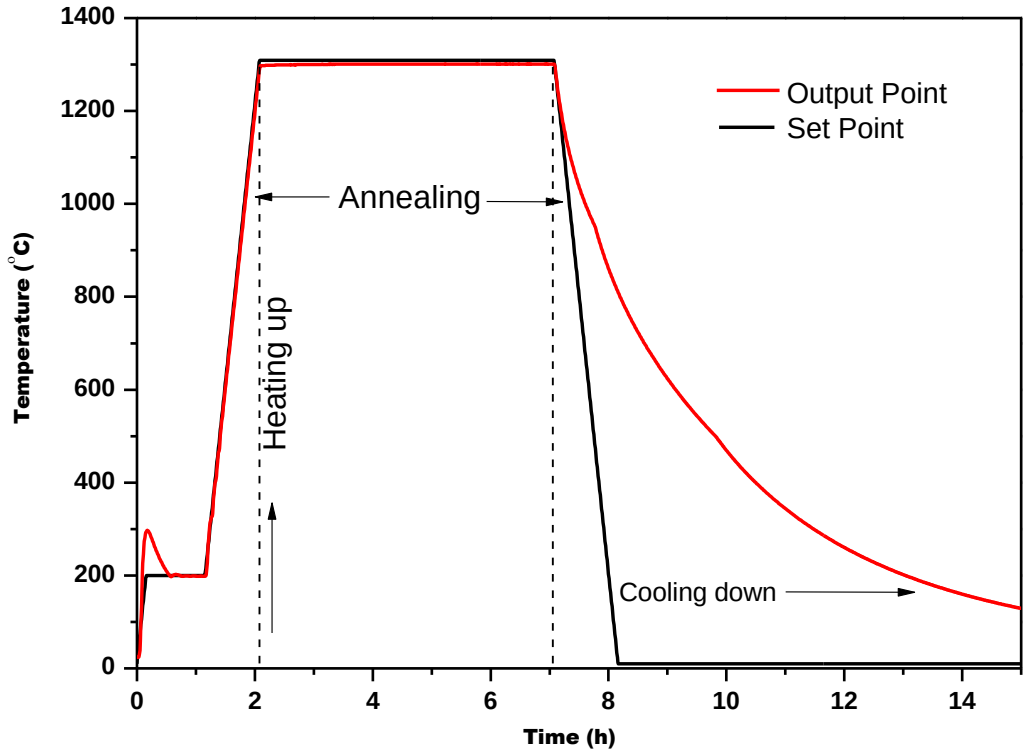

Figure 6.2: *Schematic diagram showing the heating and cooling curves for samples annealed at 1300 ˚C for 5 hours. Temperatures measured with a thermocouple are shown in red, while programmed data are shown in black.*

6.4 Measurement conditions

In order to investigate the structural changes and migration of ruthenium implanted in glassy carbon, Raman spectroscopy, SEM, AFM, XRD, RBS and SIMS analyses were conducted before and after annealing. The advantages and disadvantages of these instruments are shown in Table 6.1 below.

Table 6.1: *Advantages and disadvantages of the instruments used in this study.*

Instruments	Advantages	Disadvantages
Raman spectroscopy	• Non-destructive • Samples do not require special preparation. • Spectral range reaches well below 400 cm^{-1}, making it ideal for organic and inorganic species.	• Cannot be used for metal or alloys. • Difficult to measure low concentrations since Raman effect is weak.
Scanning electron microscopy	• Produce high-resolution images. • It has a wide range of applications, in industry, biomedical science, and for analysing microorganisms,	• SEM can only produce black and white images. • Living specimens cannot be analysed using SEM.

	cells, etc.	
Atomic force microscopy	• AFMs have an advantage in their ability to operate in vacuum, air, and in liquids. • AFM can measure surface physical properties, such as magnetic fields (MFM), surface potential (SKPM), surface temperature (SThM), friction (SFM), and many other surface physical properties.	• AFM images always require image processing before optimal viewing of surface structures.
X-ray diffraction	• Non-Destructive Technique. • It can be used to determine the orientation of the individual grains of a crystal and to identify crystal structures in unknown substances.	• The major limitations of the XRD are it cannot identify the amorphous materials and does not gives information on profile depth.
Rutherford backscattering spectrometry	• Quantitative and nondestructive surface analysis.	• The determined depth of elements in samples can be

	• Measures the composition and thickness of nanoparticles. • Measures mass and depth of the target sample. • Non-Destructive Technique.	affected by the surface roughness.
secondary ion mass spectrometry	• High sensitivity. • the ability to obtain molecular information. • Isotopic analysis and lateral characterization (imaging). • Analysis of low-atomic-number elements such as H and Li.	• Destructive Technique.

6.4.1 Raman measurement

In order to characterize the structural changes in glassy carbon as a result of ion implantation and annealing, a T64000 micro-Raman spectrometer (HORIBA Scientific, Jobin Yvon Technology) was used with a 514 nm laser wavelength and a 120 second spectral acquisition time. Moreover, to minimize heating effects during measurements, the Raman system laser power was kept below 3 mW. The 50× objective was used to acquire the Raman spectra.

6.4.2 The SEM measurement

Using Zeiss Ultra Plus SEM at the University of Pretoria, the surface changes of glassy carbon samples after ion implantation and heat treatment were investigated. For the SEM measurements, an analyzing voltage of 2 kV was used. Both SE and SE in-lens detectors were used throughout this work. SEM images of glassy carbon sample surfaces were taken before, after implantation and after every heat treatment. The working distance was kept at 2.8 mm and magnifications were set at 1 µm, 100 nm, and 200 nm, respectively.

6.4.3 The AFM measurement

Glassy carbon samples were attached to metal plates (i.e., sample holders) before AFM measurements. The Dimension Icon AFM system was used to obtain AFM images. The system operates in contact mode and has a sharp nitride lever (SNL) probe with a spring constant of 0.30 N/m. Sample analysis is performed with AFM probes that have a tip radius of 2 nm and scan rates of 0.3 Hz. The resonance frequency of the SNL probe was between 40 and 75 kHz. AFM images obtained during the analysis of all samples were further analyzed using NanoScope Analysis (Bruker, USA).

6.4.4 XRD measurement

An XRD analysis was performed with Bruker D8 Discover equipment utilizing Cu (K_α) as the source of radiation. During data collection, a two-theta step size of 0.03 and a dwell time of 240 seconds per frame (four frames) were used. The incident X-ray beam was retained at 3° relative to the sample surface in this experiment, while the detector was rotated from 22° to 120° two-theta (using a goniometer) to collect the diffraction pattern. Through comparing peak positions and relative intensities of our samples with those in the ICSD (the Inorganic Crystalline Structure Database), we were able to identify crystalline phases found in our samples. In addition to providing information on d-spacing and peak intensities, ICSD provides hkl values, chemical formulas, cell dimensions, selected physical properties, and references [Ber83]. The data collected is presented and discussed in detail in Chapter 7.

6.4.5 The RBS measurement

Rutherford backscattering spectrometry was used to analyse the implanted glassy carbon samples before and after annealing. The Van de Graaff accelerator at the University of Pretoria was used to bombard the samples with 1.6 MeV helium particles. A total charge of 8 μC was used per measurement. The measurement was repeated three times for each sample to reduce noise in the RBS spectra. In this experiment, the sample tilt angle was maintained at 10° and the surface barrier detector was positioned at a scattering angle of 165°. The detector had a solid angle of 3.41 msr. Throughout the study, the maximum beam current was kept at 15 nA to ensure uniformity.

6.4.6 The SIMS measurement

RBS and SIMS were used to measure the depth profiles of 150 keV Ru ions implanted in glassy carbon. Two techniques were used (i.e., RBS and SIMS) due to the breakdown of RBS during the first part of this study (i.e., annealing at low temperatures). Consequently, SIMS was used to monitor Ru depth profile changes before and after annealing at high temperatures (i.e., from 1000 to 1300 °C).

Using a Cameca IMS 7F microanalyser, SIMS analyses were performed. For each measurement, a primary beam of 10 keV O^{2+} ions was raster scanned across a sample area of 150×150 μm^2. Calibration of intensity-concentration was achieved using the as-implanted samples as a reference. Finally, depth conversion of the recorded profiles was performed by measuring the sputtered crater depth with a DEKTAK 8 stylus profilometer. This was done assuming a constant erosion rate with time.

References

[Ber83] G. Bergerhoff, R. Hundt, R. Sievers, I.D. Brown, *The inorganic crystal structure data base*, J. Chem. Inf. Comput. Sci., 23 (1983) 66-69.

[Kuh15] R.J. Kuhudzai, *Diffusion and surface effects for SiC implanted with fission product elements*, PhD Thesis, Department of Physics, University of Pretoria, South Africa, 2015.

[Odu20] O.S. Odutemowo, M.S. Dhlamini, E. Wendler, D.F. Langa, M.Y.A. Ismail, J.B. Malherbe, *Effect of heat treatment on the migration behaviour of Sr and Ag CO-implanted in glassy carbon*, Vacuum 171 (2020) 109027.

[Web06] R.D. Webb Company, *operating manual Webb® 77*, 2006.

CHAPTER 7

RESULTS AND DISCUSSION

Ruthenium (Ru) ions were implanted in glassy carbon samples at room temperature and 200 ˚C. All samples were then annealed under vacuum and at different temperatures. The effect of ruthenium ion bombardment and heat treatment on the glassy carbon structure was investigated by Raman spectroscopy and XRD. The migration behaviour of implanted ruthenium in glassy carbon due to heat treatment was investigated using RBS and SIMS. AFM and SEM were also used to investigate the surface morphology of glassy carbon after implantation and annealing. The results are presented and discussed in the following sections.

7.1 Implantation of glassy carbon with ruthenium

RBS and SIMS were used to measure the depth profiles of 150 keV Ru ions implanted in glassy carbon to a fluence of 1×10^{16} cm^{-2} at room temperature and 200 °C. The glassy carbon samples implanted with Ru were annealed at two temperature regimes (from 500 to 1000 °C and from 1000 to 1300 °C -in steps of 100 °C) for 5 h under vacuum.

Figure 7.1 shows the RBS depth profiles of Ru that were compared with the theoretical spectra obtained from the TRIM ion distribution simulation software. The TRIM simulations were conducted by taking the density of glassy carbon as 1.42 g/cm^3, representing the density of the virgin Sigradur®G glassy carbon samples used in this study. Furthermore, TRIM simulations were also used to determine the displacement per atom (dpa) introduced in glassy carbon by Ru implantation - see Figure 7.1. Apart from bombardment parameters such as energy of the ion bombardment, the dpa is mostly influenced by ion fluence (the vacancy distribution, surface and maximum damage values (dpa) are extracted based on fluence). The dpa was calculated using equation (3.28) – see section 3.4.

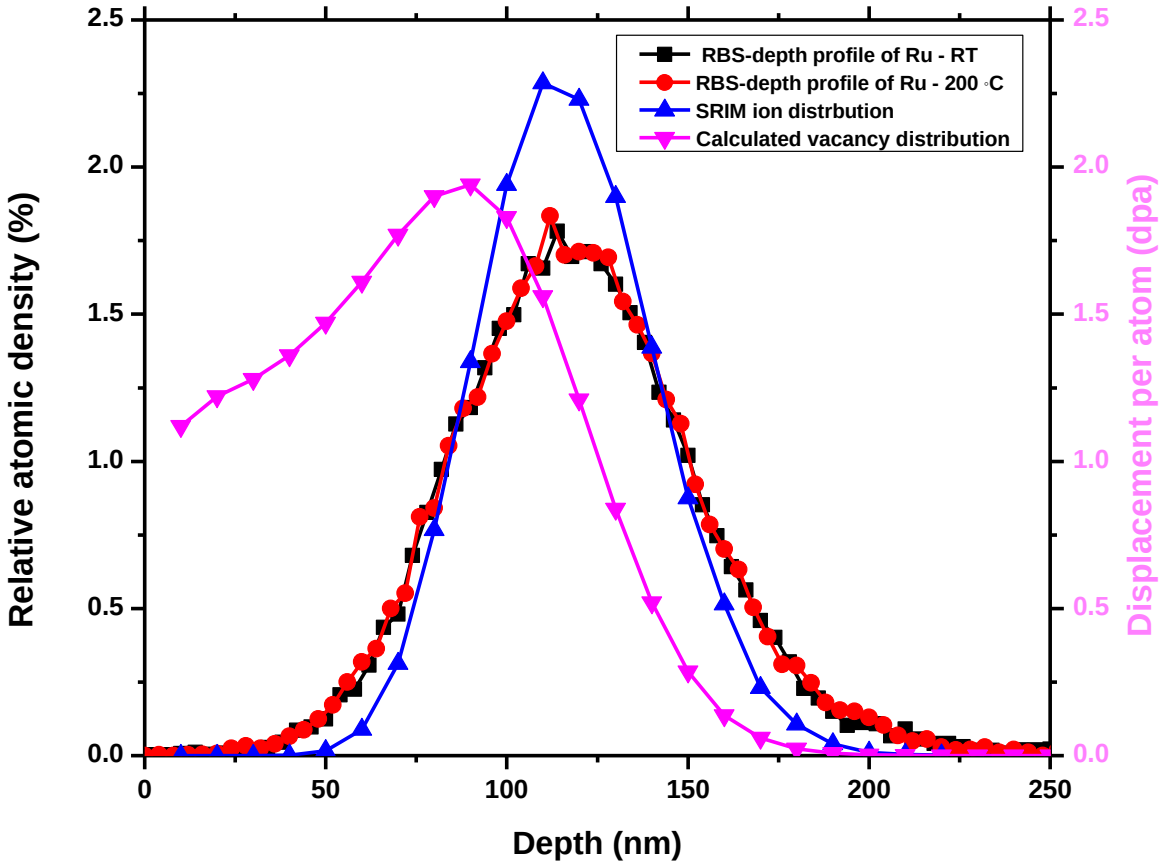

Figure 7.1: *RBS depth profiles of Ru ions implanted in glassy carbon at room temperature and 200 °C compared with TRIM simulation profile. The damage in dpa is also shown (in magenta) using the ions fluence of* $1\times10^{16}cm^{-2}$.

In order to estimate the experimental projected range, R_p, the depth profiles of Ru in glassy carbon were fitted with a Gaussian equation. According to our experimental results, Ru implanted at room temperature and 200°C exhibit depth profiles with R_p values of 116.5±1 and 116±1 nm, respectively. These values are comparable with the 115 nm of the TRIM results. However, the difference between the range straggling, ΔR_p, obtained from RBS (31.2±1 nm) and TRIM (24.4 nm) is about 24.5%, which exceeds TRIM accuracy (i.e., 5-10%). This discrepancy in the ΔR_P could be as a result of the trapping of some of the implanted ions in the pores contained within the glassy carbon structure [Odu18]. Furthermore, the discrepancy in the ΔR_P could be due to surface roughness which can lead to a broader ion distribution than suggested by TRIM (i.e., TRIM considers the target as amorphous and having a smooth surface). In addition to this, TRIM does not take into account the dynamic composition changes and the volume density changes in the implanted layer.

As shown in Figure 7.1, the maximum damage level is 1.9 dpa obtained from TRIM simulations and equation 7.1. This is significantly higher than the critical displacement per atom (dpa) value of 0.2 dpa required to amorphize glassy carbon [McC94]. This would imply that the simulation of Ru in the glassy carbon (at the ion fluence of 1×10^{16} cm^{-2}) resulted in an amorphization thickness of about 155 nm in the glassy carbon substrate – see Figure 7.1. Moreover, comparing the damage profile with the implanted Ru distribution profile, the damage profile is closer to the surface (it has a maximum at 90 nm). This indicates that many atoms near the glassy carbon surface have been displaced. In previous studies, it was found that Se and Cd implanted into glassy carbon were trapped by the concentrated damage near the surface of glassy carbon [Ade22, Hal17]. In this study, due to the concentration of damage near the glassy carbon surface, Ru is expected to be trapped in the near surface region. The results obtained confirm this speculation.

Figure 7.2 shows the SIMS depth profiles of Ru that were compared with the theoretical spectra. According to the experimental results, the Ru depth profiles have an R_p value of 115±1 nm for both room temperature and 200°C implanted samples. This value is comparable with TRIM results which showed a R_p value of 115 nm. Moreover., TRIM results showed that the ΔR_p value equal to 24.4 nm, while the values obtained from SIMS is equal to 23.9±1 nm for both samples implanted at room temperature and 200 °C. The discrepancy in the ΔR_p values between SIMS and TRIM is significantly smaller than the discrepancy between RBS results and TRIM. This agrees with the assumption that RBS has generally lower sensitivity and depth resolution compared to SIMS [Www1].

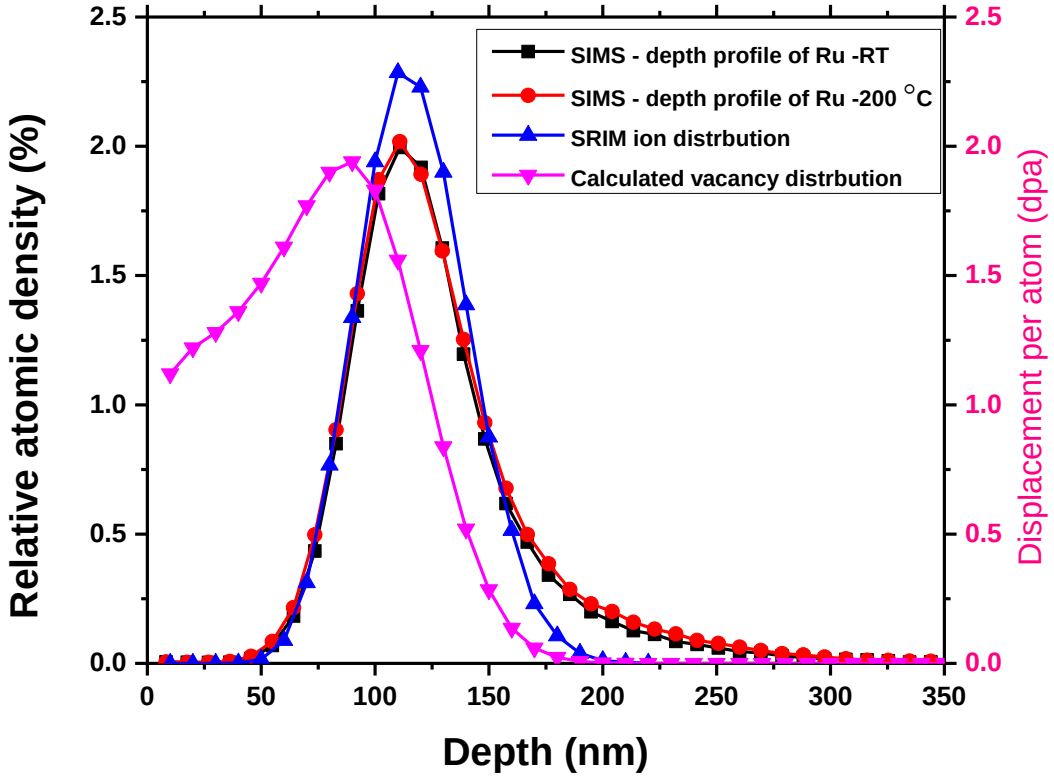

Figure 7.2: *SIMS depth profiles of Ru ions implanted in glassy carbon at room temperature and 200 °C compared with TRIM simulation profile. The damage in dpa is also shown (in magenta) using the ions fluence of* $1\times10^{16}cm^{-2}$.

7.2 Effects of thermal annealing on migration and structure of Ru implanted glassy carbon

7.2.1 Raman results

Raman spectroscopy was used to monitor structural changes in glassy carbon caused by Ru implantation (at room temperature and 200 °C) and heat treatment. Figure 7.3 compares the Raman spectrum of virgin glassy carbon with that of implanted glassy carbon with Ru. Using a linear background correction, the baseline of the Raman spectra lines was corrected in order to analyse the data obtained. Then, the spectra were fitted using a Gaussian function and a Breit-Winger-Fano (BWF) function. These fittings were done to enable us to obtain information such as the area under peak, peak intensity, full width at half maximum (FWHM) and peak position. Using Raman band intensity, position, and FWHM, glassy carbon structures can be analysed based on their defects, crystal size, and residual stress.

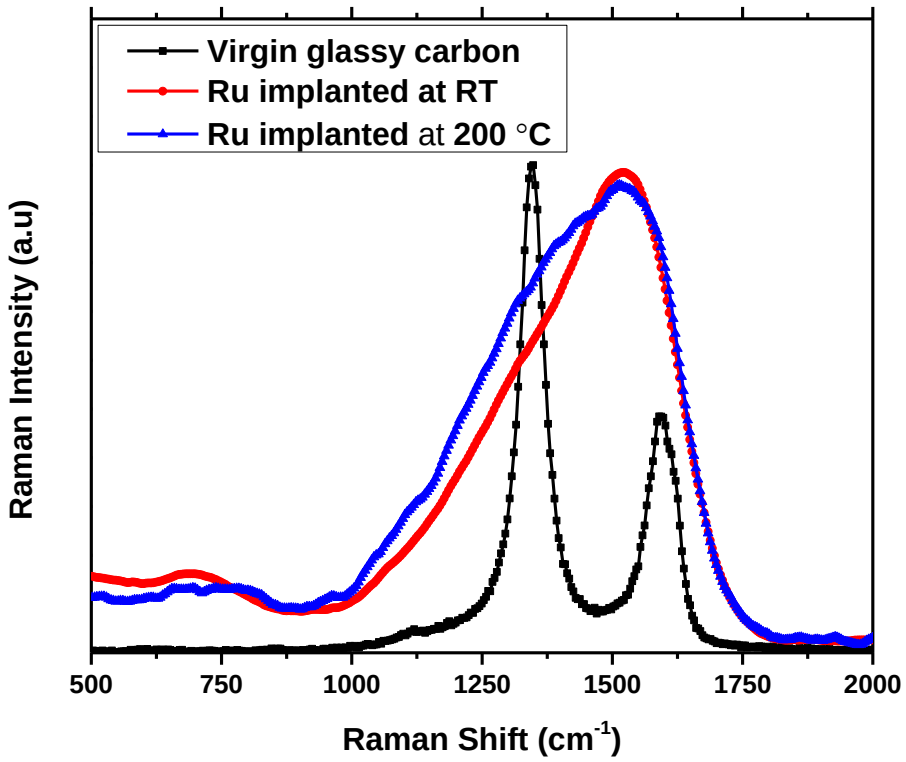

Figure 7.3: *Raman spectra of glassy carbon before and after ruthenium implantation at room temperature and 200 °C.*

Raman spectrum of virgin glassy carbon sample shows the D and G characteristic bands at positions 1346 cm^{-1} and 1587 cm^{-1}, respectively. The D and G peaks originate from the disordered sp^3 bonds and sp^2 vibrations of graphite, respectively [Orl21]. These two peaks of the glassy carbon indicate the presence of small graphitic crystallites (ribbons) imbedded in the amorphous matrix [Ism18]. The D and G peaks merged into a single broadband after implantation at room temperature and 200 °C. Only amorphous carbon structures have Raman spectra similar to those obtained from the as-implanted glassy carbon [Sil03, Fer00, Yos88, McC94, McC95]. This indicates the amorphization of the graphitic crystallites in the implanted glassy carbon samples [Ism18, Orl21]. However, a broader peak was present in the Raman spectrum of the as-implanted samples at 200 °C compared to those implanted at room temperature – see Figure 7.3. Adeojo *et al.* [Ade22] also presented similar results, concluding that the magnitude of radiation damage in the room temperature implanted sample is greater than that in the 200 °C implanted sample. McCulloch *et al*. [McC95] explained this phenomenon and the connections between implantation temperature and glassy carbon

structure. They found that structural changes in glassy carbon occur as a result of defect motion (in glassy carbon) during irradiation. If the irradiation is performed at RT, the defect motion during irradiation is suppressed. Thus, implantation at room temperature would easily amorphized glassy carbon. However, if the implantation temperature is higher than room temperature but lower than 320 °C, the mobility of C interstitials during irradiation results in dynamic annealing which prevents amorphization, with the result that ion irradiation creates highly disordered, but essentially graphitically bonded carbon [McC95]. Similar results from several studies [Ade20, Ade22, Njo21, Njo17, Odu18, and Ism21] also showed that implantation of fission products into glassy carbon at room temperature amorphized the material, while implantation at higher temperatures showed fewer defects in the structure. Moreover, the Raman data correlate with the TRIM simulation data presented in Figure 7.1, which showed that implantation of Ru in the glassy carbon (at ions fluence of 1×10^{16} cm^{-2}) resulted in an amorphization thickness of about 155 nm in the glassy carbon substrate.

Raman spectra of virgin glassy carbon samples, as-implanted at room temperature and 200 °C, and annealed samples at temperatures from 500 to 1000 °C are shown in Figures 7.4 and 7.5. Initial annealing at 500 °C showed broad D and G peaks, indicating partial recrystallization of glassy carbon after annealing. The observed intensity of the re-grown G peak is higher than that of the D peak. This was more apparent in the implanted samples at RT- see Figure 7.4. However, further annealing from 600 °C to 1000 °C resulted in the enhancement of the D peak intensity and a reduction in the G peak width. This indicates that some recovery of the glassy carbon structure increased with the increasing annealing temperature [Ade20, Ade22, Njo21, Njo17, Odu18, and Ism21]. Moreover, at 1000 °C, the intensity of the D and G peak appears to be the same. It is noteworthy that this is in contrast to the Raman spectrum obtained for virgin glassy carbon, which shows a more distinct D peak. This is proof that annealing at 1000 °C did not completely remove all the damage (in glassy carbon) introduced by Ru ion implantation.

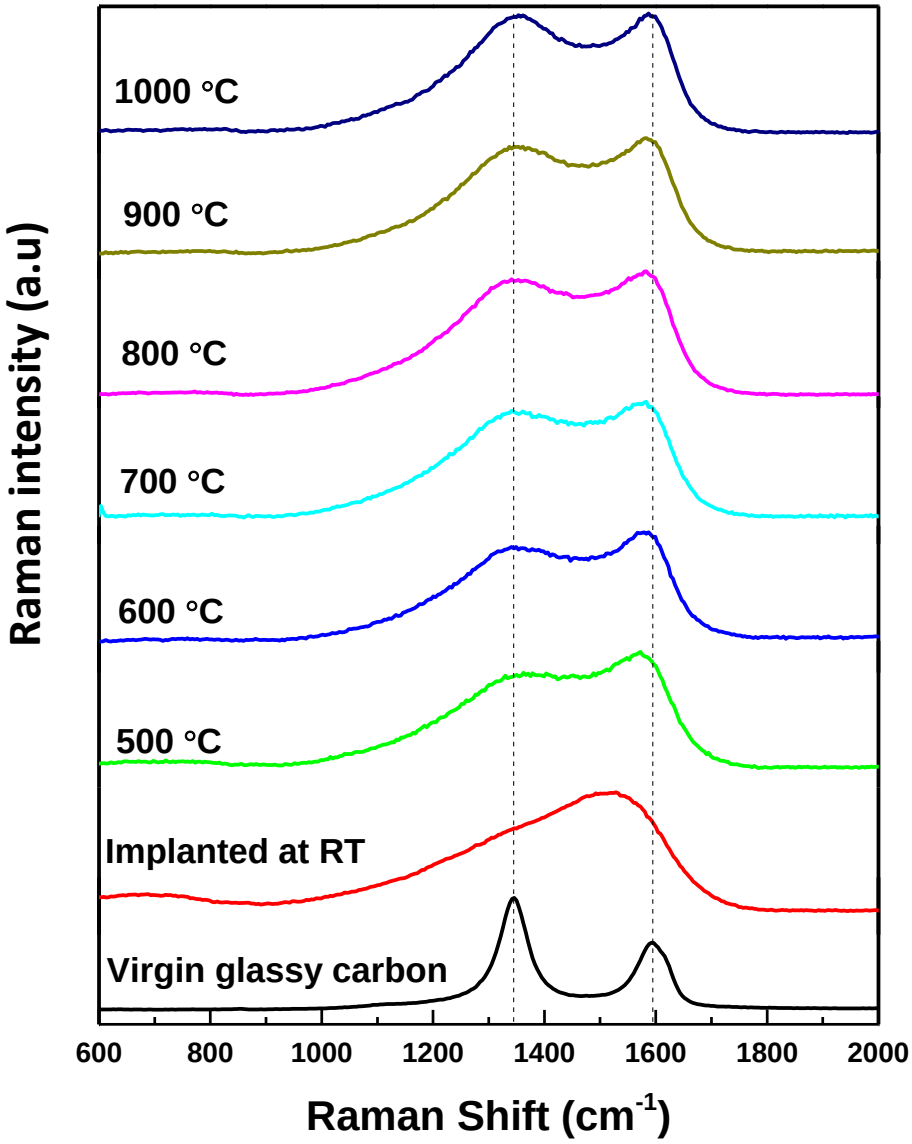

Figure 7.4: *Raman spectra of glassy carbon before and after Ru implantation at room temperature and annealing the implanted glassy carbon samples from 500 to 1000 °C.*

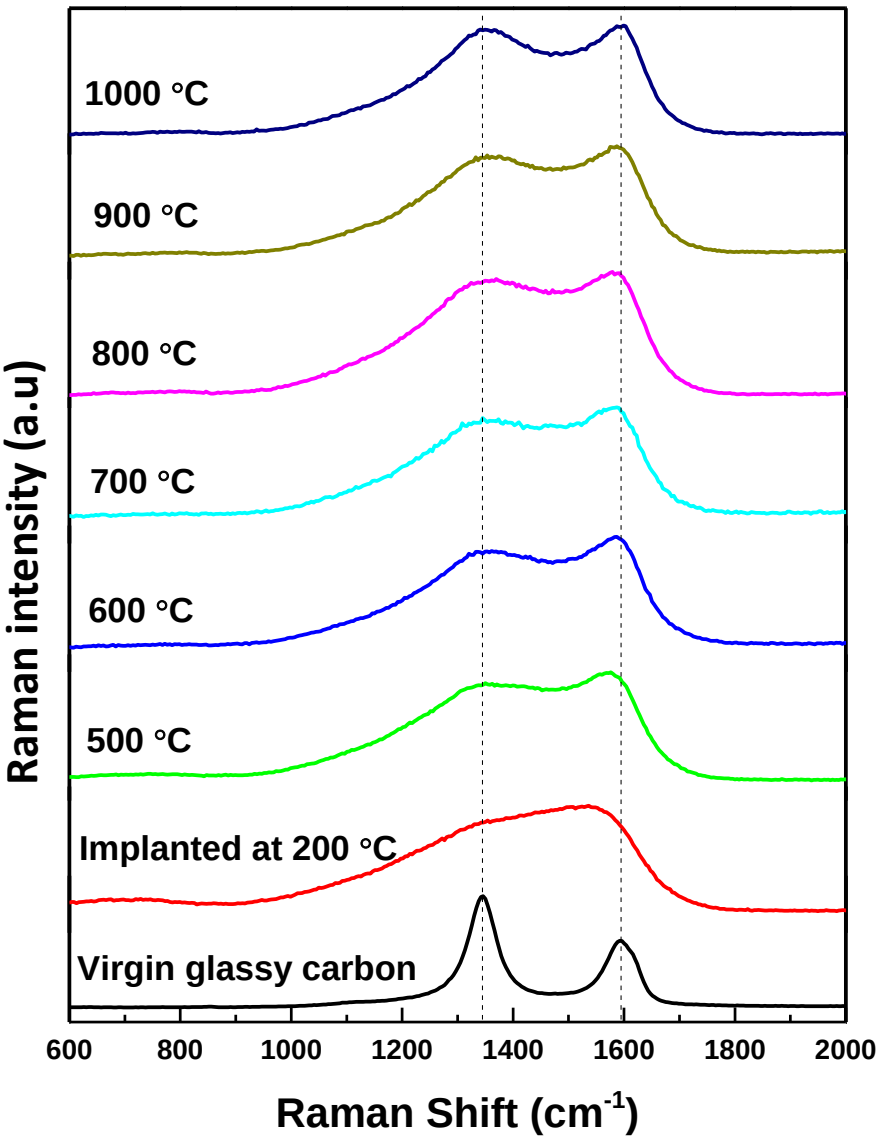

Figure 7.5: *Raman spectra of glassy carbon before and after Ru implantation at 200 °C and annealing the implanted glassy carbon samples from 500 to 1000 °C.*

Figure 7.6 shows the FWHMs of the G peaks of the acquired spectra before and after annealing of the glassy carbon samples implanted with Ru at room temperature and 200 °C. From Figure 7.6, the FWHM value of the G peak increased from 31±2 cm^{-1} (virgin glassy carbon) to 155±2 cm^{-1} and 136±2 cm^{-1} after implantation with Ru at room temperature and 200 °C, respectively. This broadening is due to the introduction of disorder (point defects) within the glassy carbon structure [Ism18, Odu16, Orl21, and Niw95]. However, the G peak in room temperature implanted samples is broader than that in 200 °C implanted samples. This indicates that samples implanted at room temperature have more defects than those implanted at 200 °C

[Ade22]. Annealing from 500 to 1000 °C resulted in a decrease in FWHM in all samples. The decrease in FWHM was an indication of the removal of some defects (annealing of radiation damage introduced by Ru ion bombardment) [Jaf23, Ism18 and Odu16]. However, samples implanted at room temperature still contained higher defects than samples implanted at 200 °C and annealed under the same conditions – see Figure 7.6. Moreover, at 1000 °C, FWHM values are 93±2 and 80±2 cm^{-1} for room temperature and 200 °C implanted samples respectively. These values are higher than 31±2 cm^{-1} for virgin glassy carbon. This is further proof that annealing did not completely remove all the damage introduced by the Ru ion bombardment [Mal18].

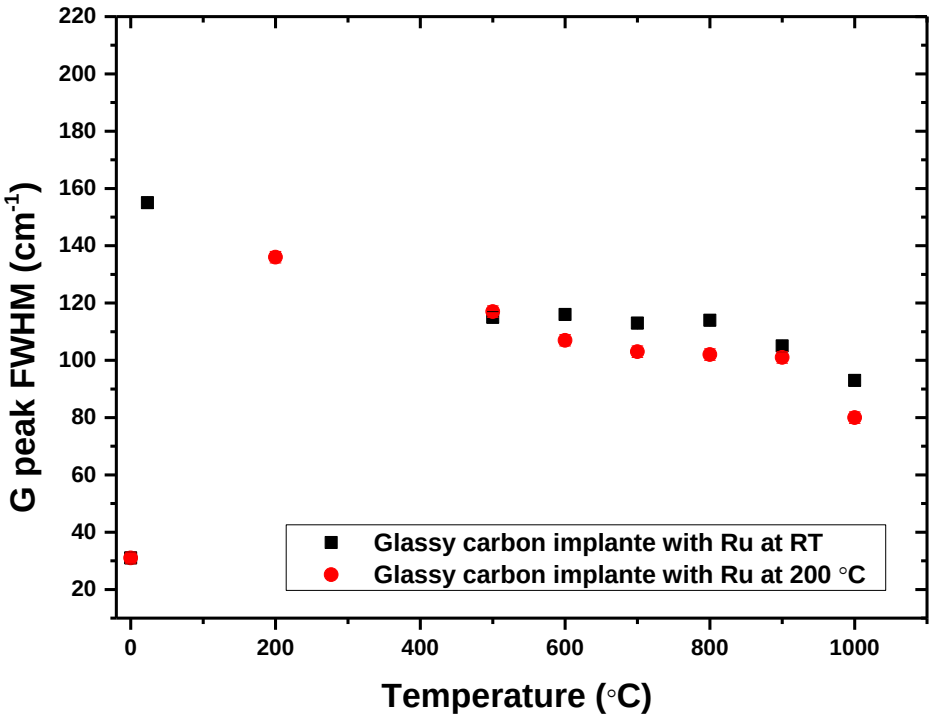

Figure 7.6: *The effect of Ru ions bombardment temperature (23˚C and 200 ˚C) and heat treatment on the FWHM values of the G peak acquired after fitting the spectra with the BWF function. The position of virgin glassy carbon is shown at 0 ˚C. Although error bars were included, their values are small to be clearly visible.*

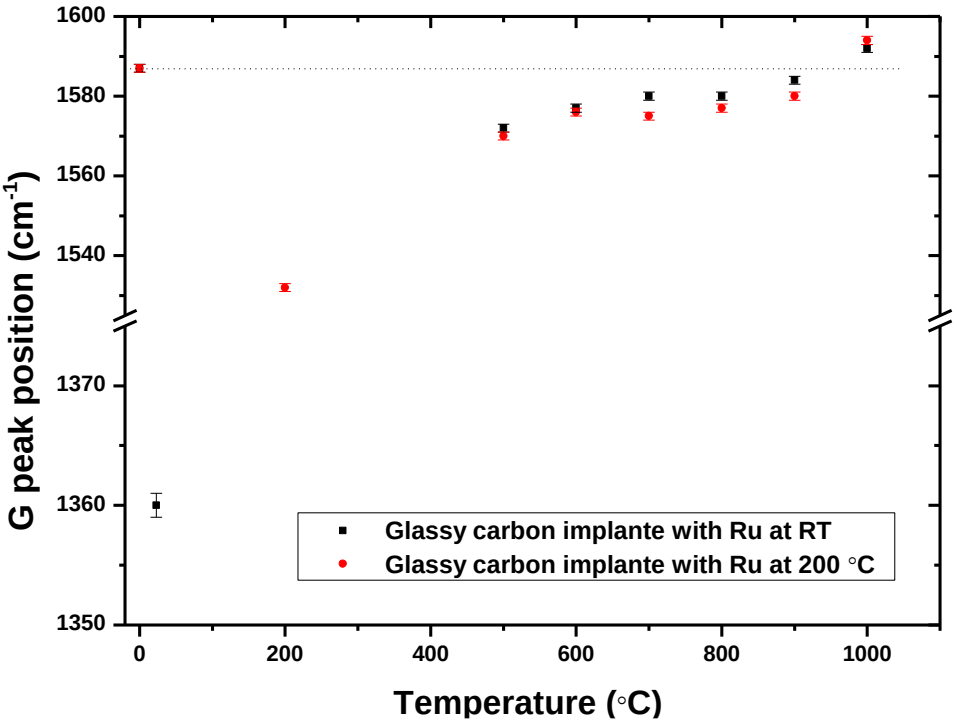

Figure 7.7: *The G peak position of the acquired spectra after Ru ions bombardment and heat treatment. The position of the G peak of virgin glassy carbon is shown at 0 ˚C. Although error bars were included, their values are small to be clearly visible.*

Figure 7.7 shows the positions of the G peaks of the acquired spectra before and after annealing of the glassy carbon samples implanted with Ru at room temperature and 200 °C. The G peak of virgin glassy carbon is located at 0 ˚C. After Ru ion bombardment, the G peak position shifted to a lower wavenumber. The shift of the Raman peak to a higher or lower wavenumber can be attributed to stress [Wen12]. The type of residual stress associated with the Raman peak shift to a lower wavenumber (compared to the G peak of virgin glassy carbon) is tensile stress [Wen12]. Which means the as-implanted samples were under tensile stress due to ion bombardment. Samples implanted at room temperature exhibit more shifts to a lower wavenumber than for samples implanted at 200 °C. Several factors influence residual stress in materials, including heat, implantation, and crystal growth. However, several studies by McCulloch *et al.* [McC94, McC95, McC95'] found that an increase in the density of virgin glassy carbon after ion implantation at room temperature leads to the introduction of tensile stress in the glassy carbon. McCulloch *et al.* [McC94, McC95, McC95'] mentioned that the increase in the density of the implanted glassy carbon will require a smaller volume (since

density = mass/volume), then glassy carbon tends to contract, however, is prevented from doing so in the plane of the substrate, giving rise to a tensile biaxial stress.

Annealing the as-implanted samples from 500 to 900 °C showed a significant shift of the G peak towards the higher wavenumber, but did not exceed the position of the G peak of virgin glassy carbon. This indicates the reduction of tensile stress in glassy carbon after annealing up to 900 °C. However, annealing up to 1000 °C showed an increased shift of the G peak towards a wavenumber higher than the position of the G of virgin glassy carbon – see Figure 7.7. The shift to higher wavenumber indicates the presence of the compressive stress [Wen12]. An earlier study [Ism19] found similar results, where Xe implantation into glassy carbon introduced tensile stress while sequential annealing from 500 to 900 °C reduced the tensile stress. However, they found that sequential annealing up to 1000 °C induced compressive stress [Ism19]. The difference in stress between as-implanted and annealed samples at 900 and 1000 °C could be due to differences in the glassy carbon density. McCulloch *et al.* [McC95] and Zhang *et al.* [Zha11] found that annealing glassy carbon at temperatures around 1000 °C reduces the density of glassy carbon due to structural rearrangement formation. Reducing the density of the implanted glassy carbon after annealing will result in compressive stress [McC95']. McCulloch *et al.* [McC95'] mentioned that the decrease in the density will require a larger volume, thus glassy carbon will tend to expand, however, is prevented from doing so in the plane of the substrate, giving rise to a compressive biaxial stress. This agrees with the result presented in this study, where compressive stress was observed after annealing at 1000 °C.

Figure 7.8 and 7.9 shows Raman spectra of Ru implanted glassy carbon at room temperature and 200 °C and annealed at high temperatures (sequentially from 1000 to 1300 °C), respectively. From Figure 7.8 and 7.9, the re-growth of the Raman D and G peaks after annealing of the as-implanted glassy carbon samples at temperatures from 1000 to 1300 °C indicates the recrystallization of glassy carbon. However, the structure did not return to its original state of virgin glassy carbon even after annealing at 1300 °C – see Figures 7.8 and 7.9.

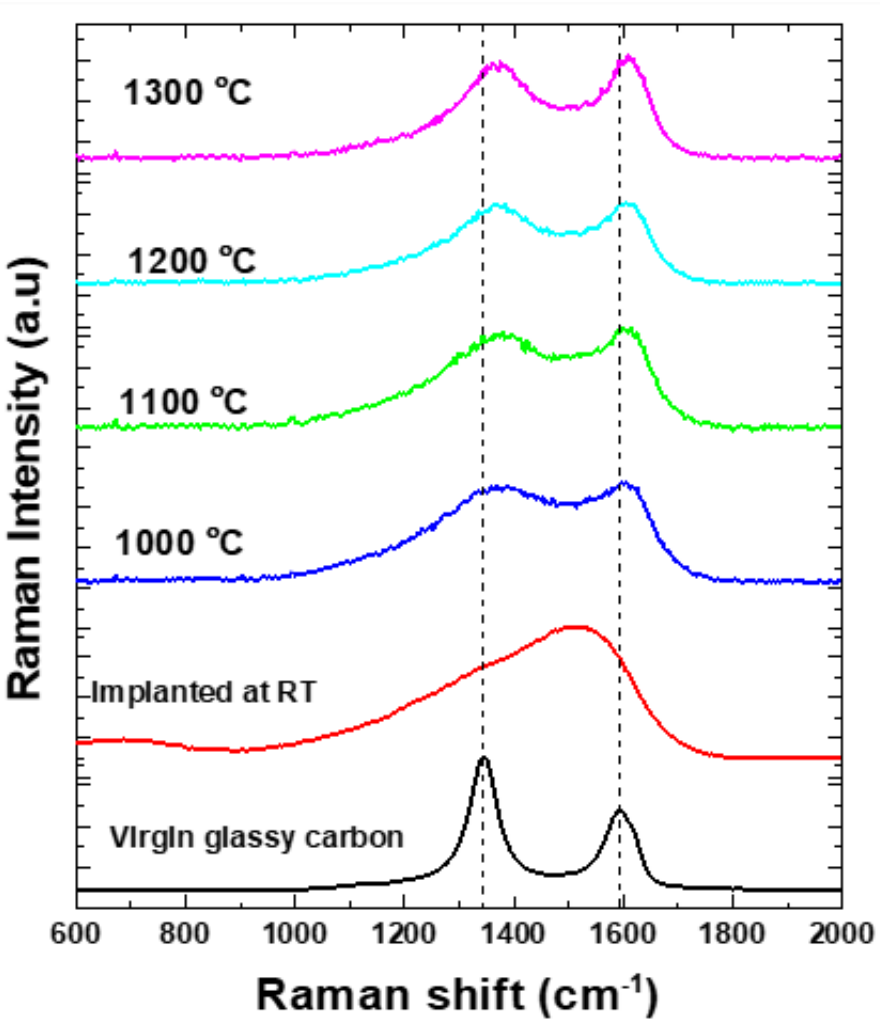

Figure 7.8: *Raman spectra of glassy carbon before and after Ru implantation at room temperature and after annealing the implanted glassy carbon samples from 1000 to 1300 °C.*

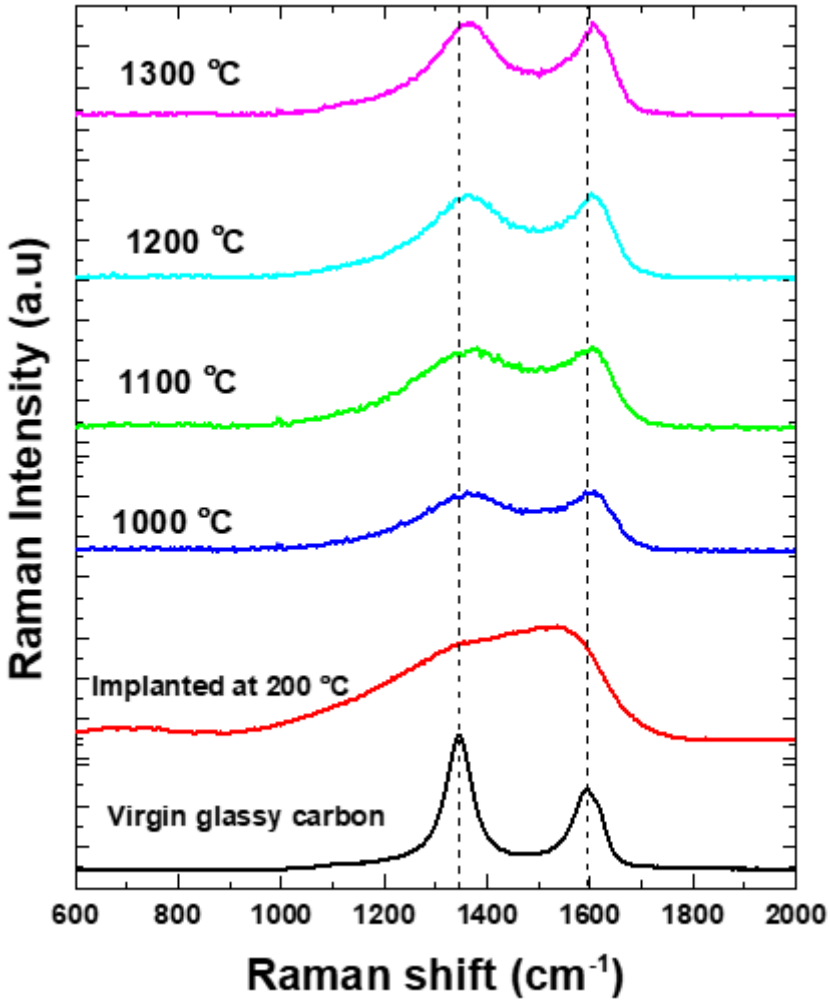

Figure 7.9: *Raman spectra of glassy carbon before and after Ru implantation at 200 °C and after annealing the implanted glassy carbon samples from 1000 to 1300 °C.*

Figure 7.10 shows the FWHMs of the G peaks of virgin, as-implanted and annealed glassy carbon at high temperatures. As mentioned above, an increase in the FWHM value of the G peak after implantation indicates the introduction of disorder within the glassy carbon structure, while a decrease in the FWHM value of the G peak after annealing indicates the recrystallization of glassy carbon. Annealing from 1000 to 1300 °C caused more decreases in the FWHMs for samples implanted at 200 °C compared to samples implanted at room temperature and annealed under the same conditions – see Figure 7.10. This indicates that samples implanted at 200 °C have less defects than samples implanted at RT, all annealed from 1000 to 1300 °C. This could be due to the initial number of defects in glassy carbon introduced by the ion implantation process (where implantation at room temperature caused more radiation

damage/defects than those implanted at 200 °C). Figure 7.10 includes error bars, but they cannot be clearly seen because their values are small (±2 cm^{-1}).

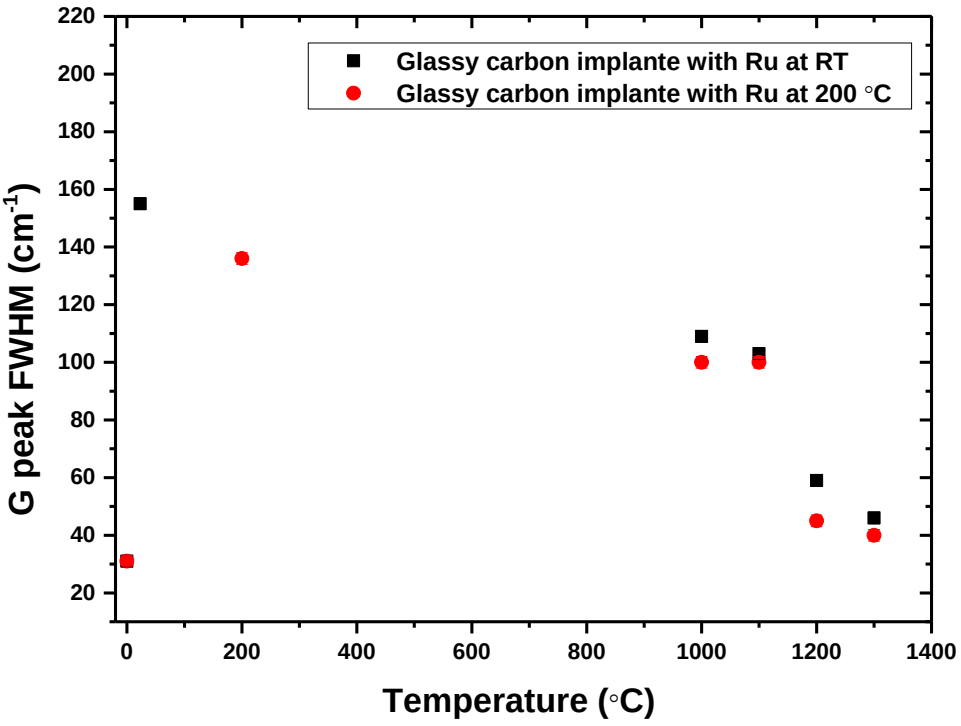

Figure 7.10: *The effect of Ru ions bombardment temperature (23˚C and 200 ˚C) and heat treatment on the FWHM values of the G peak acquired after fitting the spectra with the BWF function. The position of virgin glassy carbon is shown at 0 ˚C.*

Comparing Figure 7.10 with Figure 7.6, it is clear that annealing at high temperatures caused more recrystallization in as-implanted glassy carbon than those annealed at low temperatures. However, the FWHM values obtained at the highest annealing temperature (40 cm^{-1} at 1300 °C) is still greater than that of virgin glassy carbon (31 cm^{-1}), indicating that annealing did not fully remove the damage caused by Ru ions bombardment [Mal18]. Moreover, comparison of Figures 7.10 and 7.6 also reveals that samples annealed at 1000 °C exhibit a wider FWHM than those samples annealed sequentially up to 1000 °C. This indicates that samples annealed at 1000 °C have more defects than samples annealed sequentially up to 1000 °C, where sequential annealing from 500 to 900 °C caused partial removal of the defects. Ru migration in glassy carbon is influenced by defects in these samples, as will be discussed later.

Figure 7.11 shows a comparison of G peak positions of virgin glassy carbon, as-implanted and annealed samples at high temperatures. As mentioned above, after implantation, G peak positions shift to lower wavenumbers, indicating implantation-induced tensile stress in the as-implanted samples; however, shifts to higher wavenumbers after annealing indicate compressive stress [Wen12]. From Figure 7.11, annealing the as-implanted samples from 1000 to 1300 °C showed a significant shift of the G peak towards the higher wavenumber which can be attributed to the presence of the compressive stress [Wen12]. It is applicable here to use the same explanation for compressive stress that might be induced by a reduction in the density of glassy carbon after annealing at high temperatures as described above for samples that were annealed sequentially up to 1000 °C.

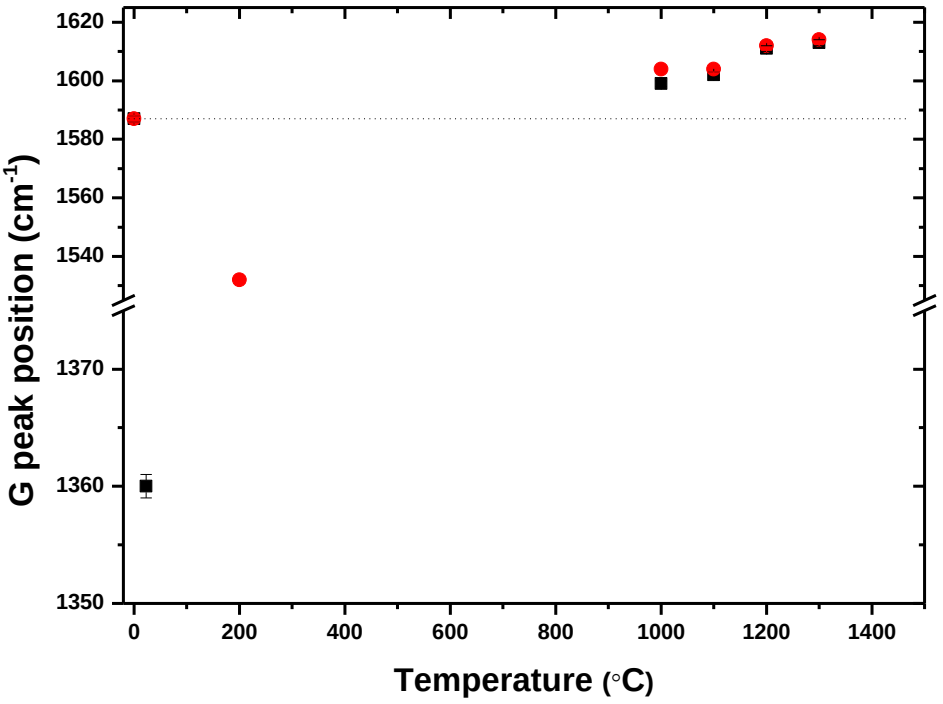

Figure 7.11: *The G peak position of the acquired spectra after Ru ions bombardment and heat treatment. The position of the G peak of virgin GC is shown at 0 ˚C. Although error bars were included, their values are small to be clearly visible.*

7.2.2 XRD results

Figure 7.12 shows the XRD diffractograms for virgin and as-implanted glassy carbon at room temperature and 200 °C. For virgin glassy carbon, the XRD reflections at 2θ = 25.3° and 43.4° correspond to a turbostratic carbon structure [Man19, Mor06]. The reflections at 2θ =

53.92° and 80.5° correspond to hexagonal and orthorhombic graphite, respectively. The XRD result, therefore, indicates that virgin glassy carbon contains amorphous carbon and graphite lattice structures. TEM studies [Ism19, Mal18] has shown that this is indeed the microstructure of glassy carbon. This XRD result is in good agreement with the Raman result of virgin glassy carbon in Figure 7.3, where the D and G peaks of the virgin glassy carbon indicate the presence of small graphitic crystallites embedded in the amorphous matrix. From Figure 7.12, implantation of the glassy carbon with Ru ions at room temperature and 200 °C resulted in a slight peak shift to a lower 2θ position and a decrease in XRD peaks intensities accompanied by an increase in their FWHM. This indicates that Ru ions implantation introduced lattice disorder and strain in the glassy carbon crystal structure [Pra20, Jue90].

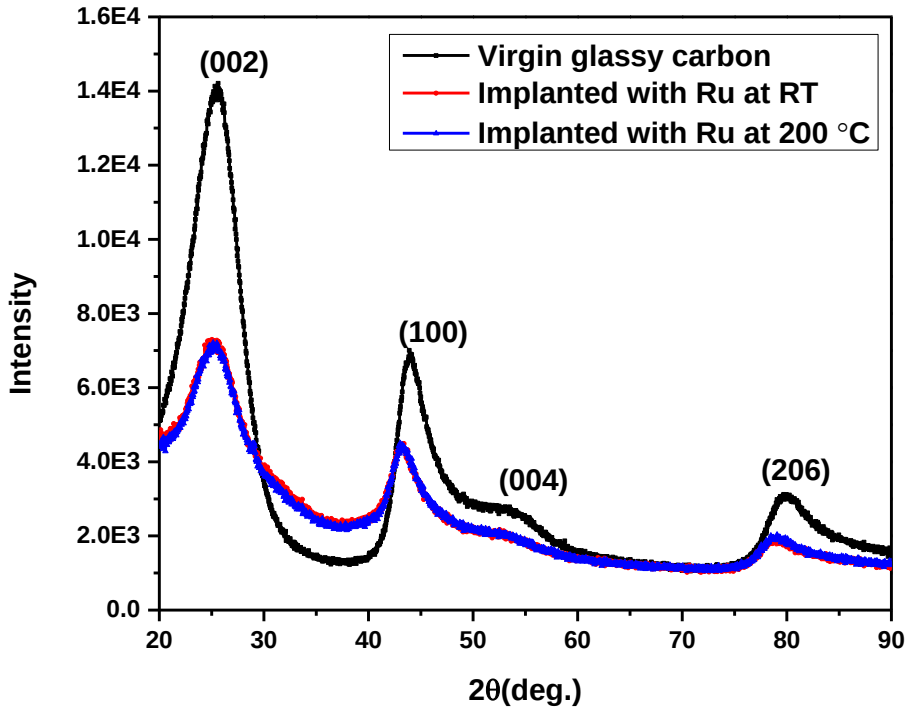

Figure 7.12: *The XRD diffractograms of virgin glassy carbon before and after Ru implantation at RT and 200 ˚C.*

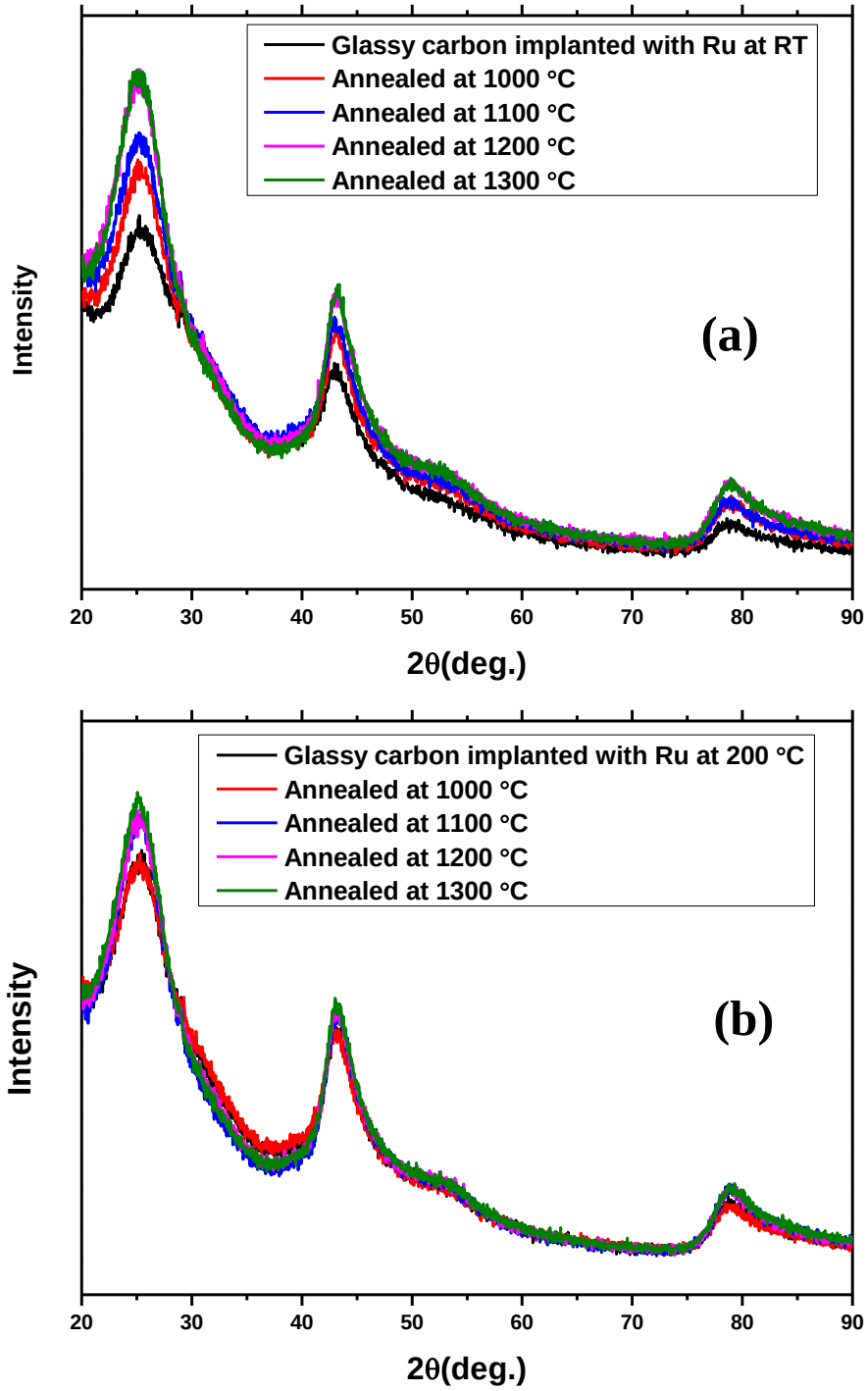

Figure 7.13: *The XRD diffractograms of as-implanted glassy carbon at (a) RT and (b) 200 C after sequentially annealed at temperatures ranging from 1000 ˚C to 1300 ˚C for 5 h at each temperature.*

Figure 7.13 (a) and (b), shows the XRD diffractograms for the as-implanted glassy carbon samples at room temperature and 200 ˚C and annealed at high temperatures (from 1000

to 1300 ˚C). The as-implanted glassy carbon showed broader lower-intensity XRD peaks, compared to the intensities of the peaks of the annealed samples. As mentioned before, the intensity of the individual diffraction peaks depends on the defects of the crystal structure as well as the internal strain of the sample [Ram09]. The internal strain of the virgin, as-implanted and annealed glassy carbon was estimated from XRD patterns using the William-Hall equation, see section 5.4.1, and shown in Figure 7.14.

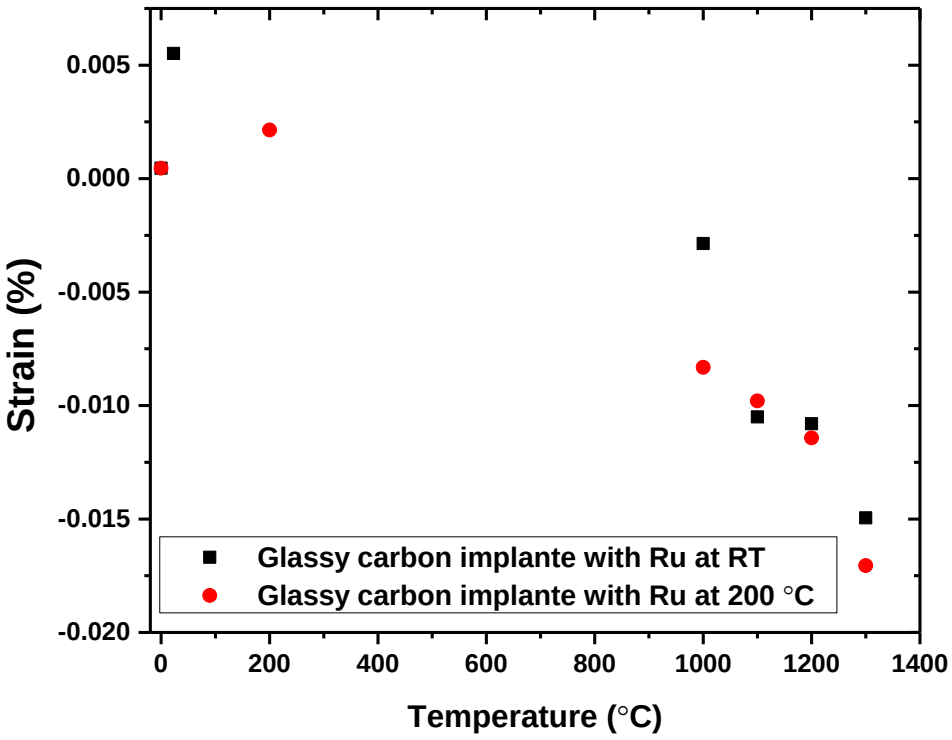

Figure 7.14: *Residual strain in virgin glassy carbon (at 0 ˚C) after implantation (at room temperature, i.e., 23˚ C, and 200 ˚C) and annealing obtained from XRD data.*

The amount of strain in virgin glassy carbon increased from 4.5×10^{-4} to 0.002 and 0.0054 after ion implantation at 200 °C and RT, respectively, indicating that ion bombardment caused radiation damage (i.e., disorder within the graphitic crystallites in the glassy carbon structure) [Khm13]. However, the strain in annealed samples has negative values – see Figure 7.14. The minus sign or plus sign in the amount of strain indicates the type of strain: the minus sign indicates compressive strain, while the plus sign indicates tensile strain [Jan07]. Therefore, as seen in Figure 7.14, implantation of Ru in glassy carbon produced tensile strain, while annealing the as-implanted samples introduced compressive strain in the glassy carbon. This is

in good agreement with Raman results in the above section, where the G peak position of virgin glassy carbon shifted to a lower wavenumber after implantation, indicating the presence of the tensile strain. However, the G peaks shift to a higher wave number after annealing from 1000 to 1300 ˚C, which indicates the presence of compressive strain. As mentioned above, the difference in strain/stress between as-implanted and annealed samples could be due to differences in the glassy carbon density after implantation and annealing. Since implantation at room temperature increases the density of virgin glassy carbon [Ade20, McC94, McC95, McC95'], the implanted region of glassy carbon will require a smaller volume, then glassy carbon tends to contract, however, it is prevented from doing so in the substrate plane, giving rise to a tensile biaxial stress [McC94, McC95, McC95']. Moreover, annealing reduces the density of the implanted glassy carbon [McC95']. Reducing the density of the implanted glassy carbon after annealing will require a larger volume, meaning that the glassy carbon will tend to expand, however, is prevented from doing so in the plane of the substrate, giving rise to a compressive biaxial stress [McC95'].

7.2.3 RBS results

The glassy carbon samples implanted with Ru were annealed at two temperature regimes (from 500 to 1000 °C and from 1000 to 1300 °C -in steps of 100 °C) for 5 hours under vacuum. The implanted Ru depth profiles after annealing at low temperatures (i.e., from 500 to 1000 °C) is shown in Figure 7.15. These depth profiles were fitted with an in-house program to obtain the projected range, R_p and the full width at half maximum FWHM [Mal17], which is shown in Figures 7.16 and 7.17, respectively. From Figure 7.15, annealing from 500 to 800 °C showed no noticeable change in Ru depth profiles as compared to the as-implanted depth profile, which indicates the non-diffusivity of Ru in glassy carbon after annealing at these temperatures. However, annealing at 900 °C and 1000 °C caused a significant change in R_p and FWHM of ruthenium depth profiles as shown in Figures 7.16 and 7.17. At 900 °C and 1000 °C, an increase in the maximum of the depth profiles peaks was observed, accompanied by a shift toward the surface and a decrease in the FWHM. This indicates that the Ru atoms aggregate (i.e., high Ru concentration) in a smaller region (i.e., narrower FWHM) after annealing at 900 °C and 1000 °C as compared to the distribution of Ru atoms before and after annealing from 500 to 800 °C. Usually, the aggregation of atoms occurs due to cohesive forces between the atoms themselves, which leads to the formation of a cluster or particle [Len37].

Ru atoms have strong cohesive forces (6.74 eV/atom) [Kax03]; thus, the Ru atoms may easily tend to aggregate into “nanoparticles” in the glassy carbon. Several studies have shown that, during annealing, the metal atoms implanted into the substrate will aggregate to form metal nanoparticles inside the substrate [Len37, Arn77, Wod93, Mio01, and Res14].

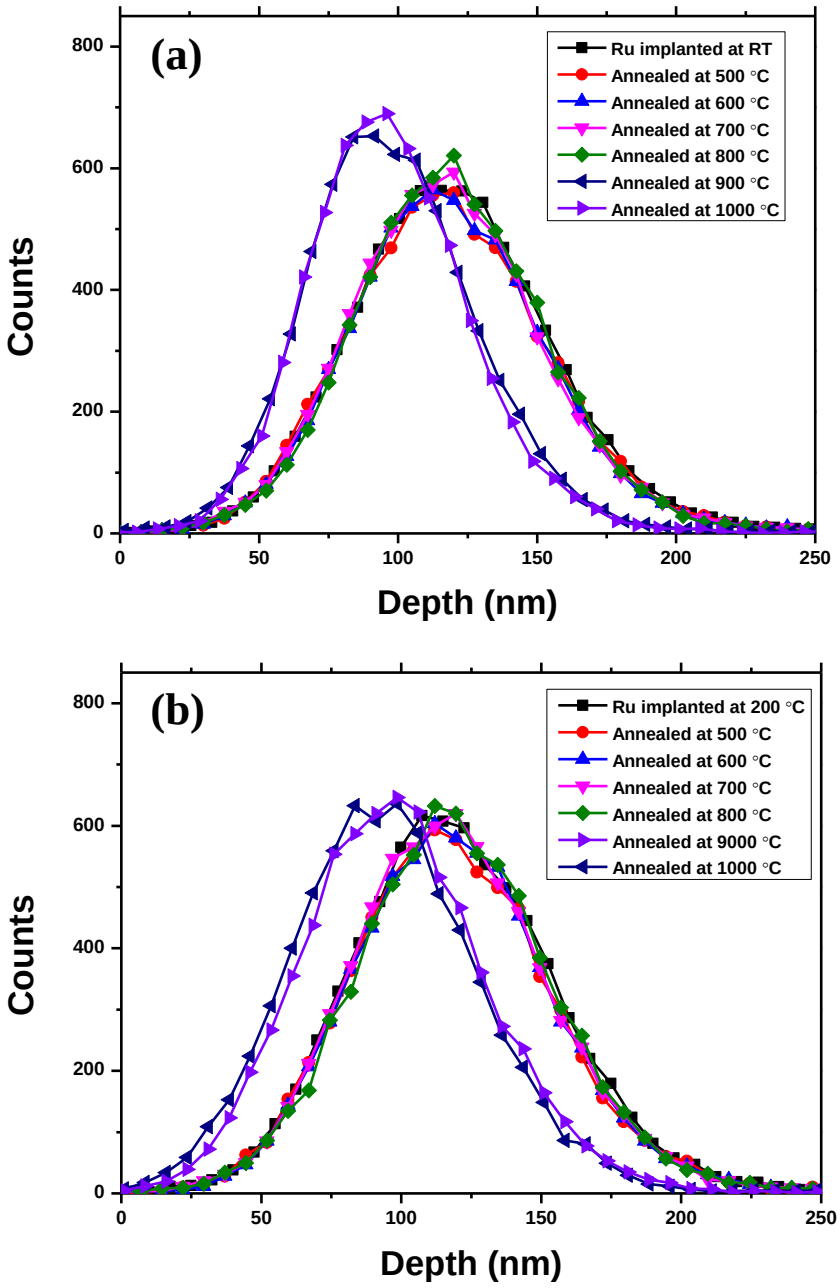

Figure 7.15: *Depth profiles of Ru implanted at (a) RT and (b) 200 ˚C, showing the effect of annealing at low temperature (500 – 1000 ˚C) on the migration behaviour.*

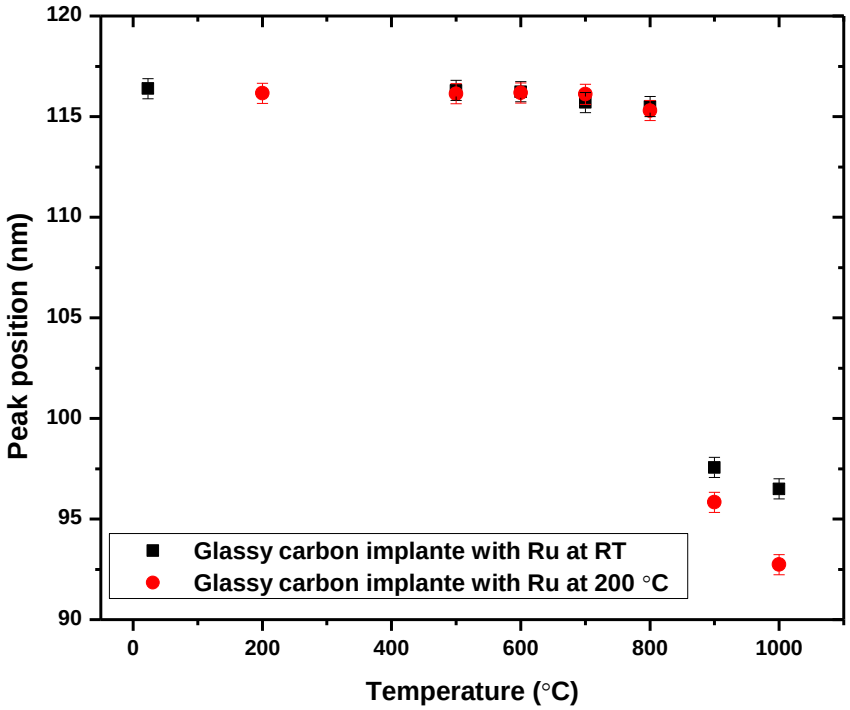

Figure 7.16: *Peak positions of Ru depth profiles (implanted at RT and 200 °C), then sequentially annealed from 500 °C to 1000 °C for 5 h.*

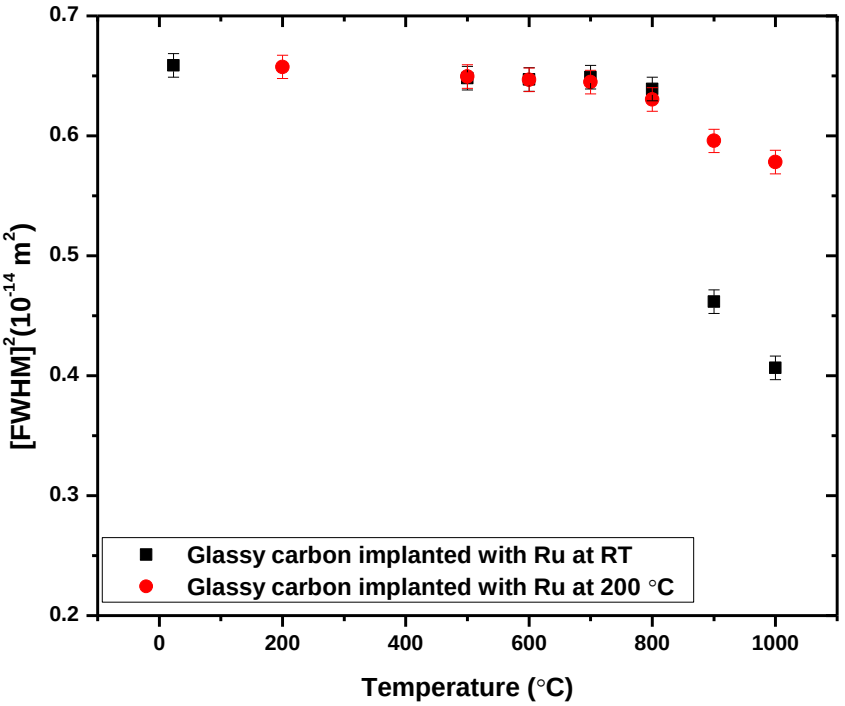

Figure 7.17: *FWHMs of Ru depth profiles (implanted at RT and 200 °C), then sequentially annealed from 500 °C to 1000 °C for 5 h.*

From Figure 7.15 (a) and (b), more Ru aggregation was observed in room temperature implanted samples compared to 200 °C implanted samples, all annealed at 900 °C and 1000 °C. This could be due to the higher concentration of defects in room temperature implanted samples (as discussed in Raman results, section 7.2.1), where defects in glassy carbon may lead to increased Ru aggregation and formation of clusters. It is consistent with the assumption that impurity clusters are more likely to form in regions with high defect concentrations (in the substrate) [Koz73].

Moreover, Ru aggregation was accompanied by a peak shift toward the surface – see Figure 7.16. This behavior is not uncommon in other systems (e.g. see [Mal13] for examples in SiC) and depends on changes in the surface microstructure (for example, thermal etching) of the substrate in which diffusion occurs. However, the shifting of the profiles towards the surface of glassy carbon is much more problematic to explain, as glassy carbon is thermally stable up to 2000 °C (i.e., with no thermal etching) [Usk21]. The peak shift toward the surface is probably due to a stress field leading to a migration of the profile as a whole [Nse14]. The Raman and XRD results showed that Ru implantation and annealing introduced high levels of stress in the implanted region (see sections 7.2.1 and 7.2.2), which could cause Ru inclusions to drift towards the glassy carbon surface. Moreover, the Ru peak shift toward the surface was lower in the room temperature implanted samples than in the 200 °C implanted samples, all annealed at 900 °C and 1000 °C – see Figures 7.15 and 7.16. This might be due to increased Ru aggregation within the room temperature implanted samples (see Figure 7.17) which can cause Ru clusters to grow larger, causing Ru to migrate more slowly toward the surface compared to the 200 °C implanted samples which showed less Ru aggregation. Another explanation is that the high concentration of defects in the room temperature implanted sample (compared to 200 °C implanted samples) can play a role in trapping the majority of the Ru atoms in the high radiation damage region which restricts its migration towards the surface. Similar results were found in a previous study [Ade22], where Se atoms implanted in glassy carbon at room temperature showed less migration towards the surface after annealing, compared to those implanted at 200 °C and annealed under the same conditions. This was explained by the higher radiation damage in room temperature implanted samples, which trapped the Se atoms [Ade22].

In Figure 7.18, the implanted Ru depth profiles are compared before and after annealing at high temperatures (1000 to 1300 °C). Furthermore, Figures 7.19 and 7.20 show the changes in peak positions and FWHMs of depth profiles due to annealing. The depth profiles peak maximum was increased after annealing at 1000 °C (compared to the as-implanted depth profile), but the FWHM decreased – see Figures 7.18 and 7.20. This indicates annealing at 1000 °C caused aggregation of Ru. This was expected since Ru atoms tend to aggregate in glassy carbon at temperatures over 800 °C. From Figure 7.18 (a) and (b), more Ru aggregation was observed in room temperature implanted samples compared to 200 °C implanted samples, all annealed at 1000 °C. As mentioned above, this due to the higher concentration of defects in room temperature implanted samples (as discussed in Raman results, section 7.2.1), where defects in glassy carbon may lead to increased Ru aggregation and formation of clusters. Ru aggregation was accompanied by a shift in depth profile peak towards the glassy carbon surface (see Figures 7.19). As with the samples annealed at low temperatures, surface stress can play a role in Ru peak shift. After further annealing at 1100, 1200 and 1300 °C, no noticeable Ru peak shift was seen in room temperature implanted samples. While a significant peak shift for Ru depth profiles was observed in 200 °C implanted samples after further annealing at 1100, 1200 and 1300 °C – see Figure 7.19. This is due to the high concentration of defects in the room temperature implanted sample which can trap the majority of Ru atoms in the high radiation damage region and lead to Ru aggregation and forming larger Ru clusters, causing Ru to migrate slower than in 200 °C implanted samples which showed less Ru aggregation.

Another important aspect is that the FWHM of Ru depth profile for sample annealed at 1000 °C (see Figure 7.20) is narrower than that of Ru depth profile for sample annealed sequentially up to 1000 °C (Figure 7.17). This demonstrates that glassy carbon samples annealed at 1000 °C have higher Ru aggregations than samples sequentially annealed up to 1000 °C. It is possible that the reduction in Ru aggregation in the samples sequentially annealed up to 1000 °C can be attributed to the partial removal of defects after sequential annealing from 500 to 900 °C (see Raman results – Figures 7.6 and 7.10). Therefore, defects in glassy carbon contribute significantly to Ru aggregation. Moreover, glassy carbon samples annealed at 1000 °C exhibit more aggregation and lower Ru peak shift toward the surface compared to those samples annealed sequentially up to 1000 °C – see Figures 7.16, 7.17, 7.19 and 7.20. Consequently, Ru aggregation may affect Ru migration toward the surface, where large aggregation may inhibit Ru migration.

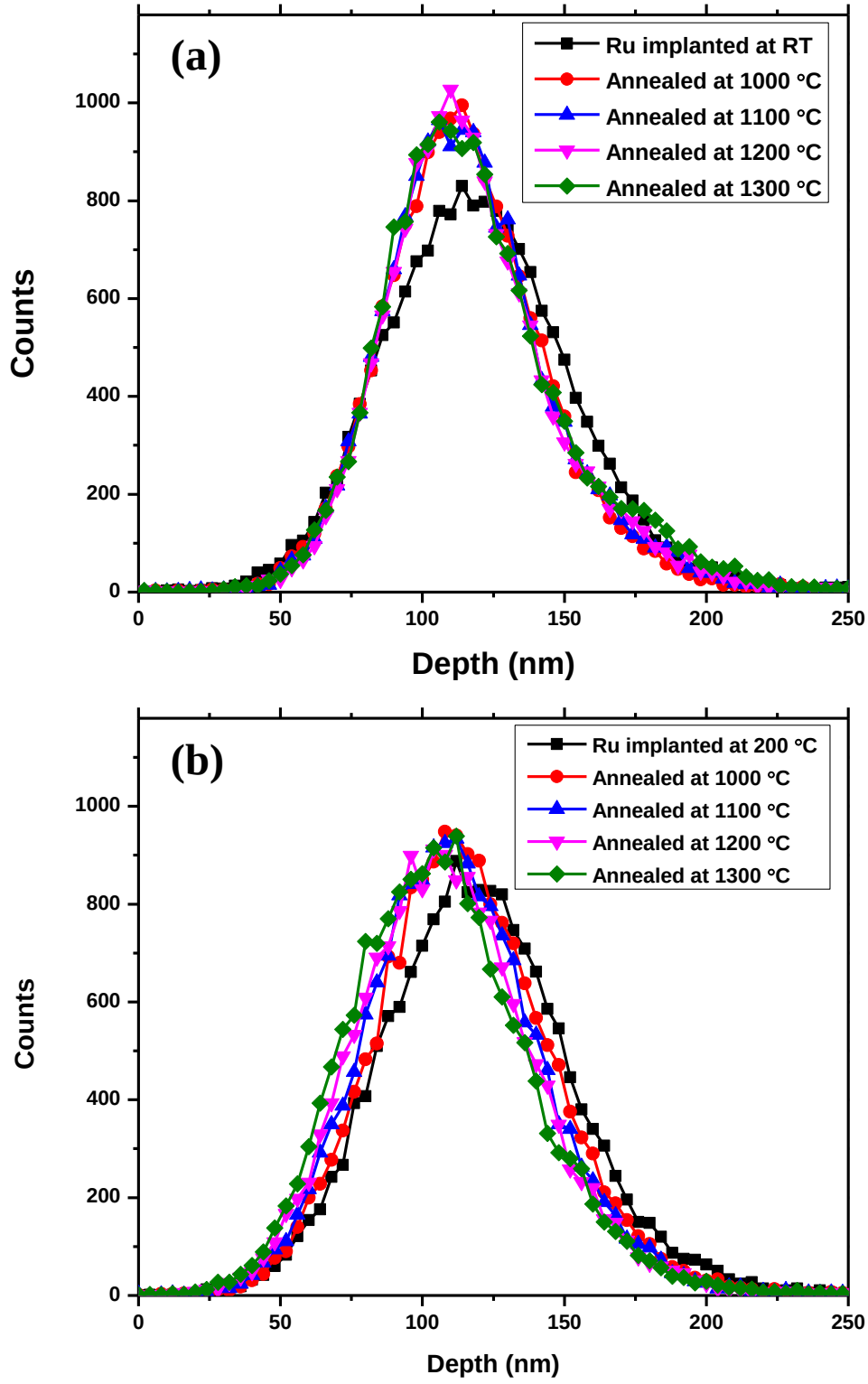

Figure 7.18: *Depth profiles of Ru implanted at (a) RT and (b) 200 ˚C, showing the effect of annealing at high temperature (1000 – 1300 ˚C) on the migration behavior of Ru.*

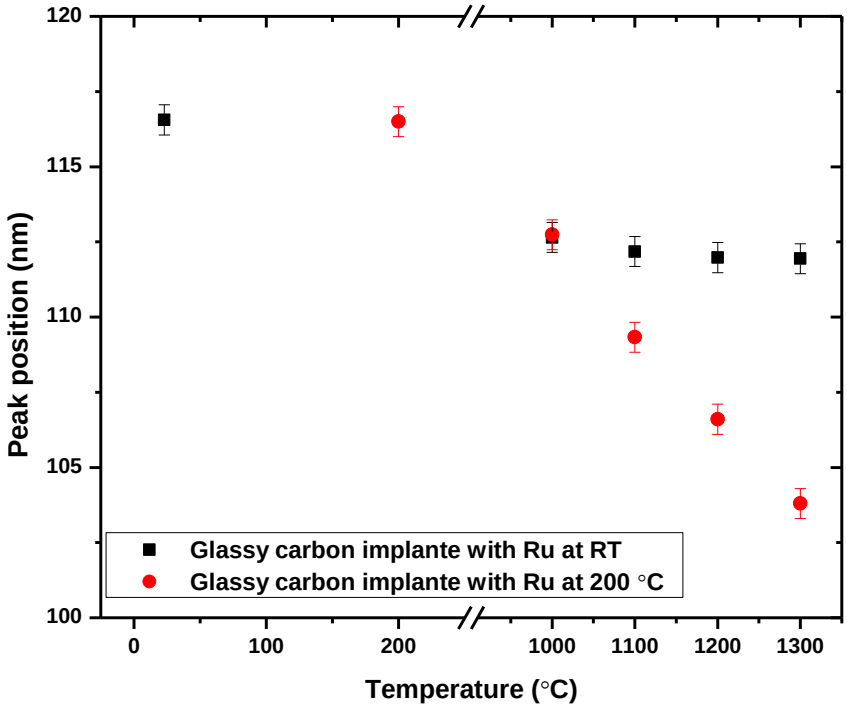

Figure 7.19: *Peak positions of Ru depth profiles (implanted at RT and 200 °C), then sequentially annealed from 1000 °C to 1300 °C for 5 h.*

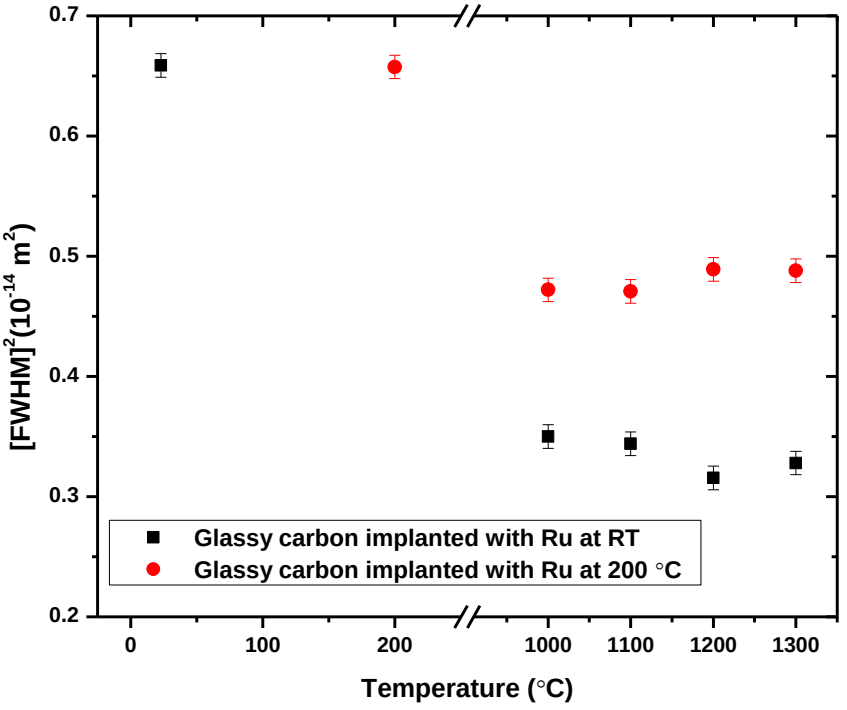

Figure 7.20: *FWHMs of Ru depth profiles (implanted at RT and 200 °C), then sequentially annealed from 1000 °C to 1300 °C for 5 h.*

From Figure 7.18 (a), a bimodal distribution of Ru after annealing at 1300 °C indicates the small segregation of Ru atoms at a depth of 175 nm below the surface. However, SIMS results presented in our previous study [Jaf23] show that the segregation of Ru atoms occurred at a depth of 155 nm below the surface, which is the interface between the glassy carbon and the bombardment-induced amorphous region (see Figure 7.1). The sizes of Ru and carbon atoms are 130 and 70 pm, respectively [Sla64]. The significantly larger size of the Ru atom means that a stress field will be created in the surrounding glassy carbon matrix. This stress field will be the cause of the segregation of Ru atoms to the interface where the stress is less.

Figure 7.21 shows the retained ratio of Ru in glassy carbon that was calculated from the total counts/yield of Ru after annealing, divided by the counts of the as-implanted sample. The retention ratios of Ru in glassy carbon before and after annealing at low and high temperatures are shown in Figures 7.21 (a) and (b), respectively. Annealing at low and high temperatures did not result in any noticeable loss of the Ru implanted in glassy carbon. This is also due to Ru aggregation forming Ru clusters inside glassy carbon, which prevents Ru out-surface diffusion.

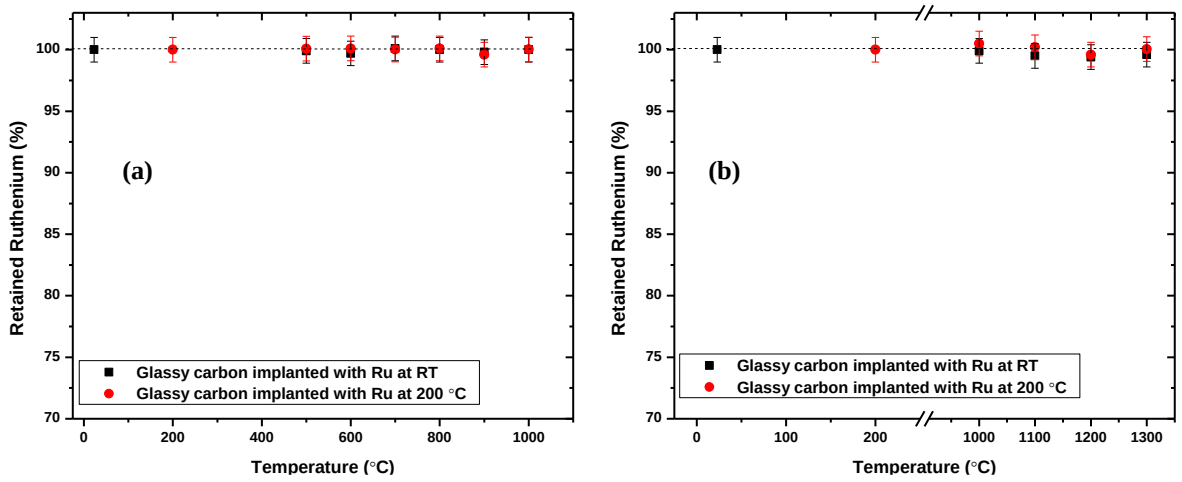

Figure 7.21: *The amount of Ru retained within the damaged region annealed from (a) 500 to 1000 ˚C and from (b) 1000 to 1300 ˚C.*

7.2.4 AFM and SEM results

SEM and AFM analyses were used to investigate changes in surface topography and roughness of the glassy carbon substrate after Ru implantation and heat treatment. The surface roughness of virgin and as-implanted glassy carbon was evaluated by the AFM images (in Figure 7.22) and by measuring the R_q (root mean square roughness) using the Nanoscope software [Nan04]. The R_q value obtained for virgin glassy carbon is 1.45±0.1 nm. This value decreased to 0.40±0.05nm and 0.37±0.05 nm after implantation of Ru at room temperature and 200 °C, respectively. In fact, the surface roughness of as-implanted glassy carbon at room temperature is no different from the surface roughness of samples implanted at 200 ˚C, which falls within measurement error. A reduction in surface roughness of virgin glassy carbon may be attributed to the Ru bombardment. It is widely known that ion bombardment often reduces the surface roughness of an initially rough surface [Mak02]. On the other hand, depending on the substrate material, ion bombardment can increase the surface roughness of an initially smooth surface [Odu18, Cha11, Bar95]. In this study, the surface of the initial glassy carbon substrate was rough (i.e., 1.45±0.1 nm), and decreased after bombardment by Ru ions (as rough surfaces become smoother by sputtering [Wag22]), indicating that Ru bombardment reduced the surface roughness which is consistent with the above statement [Mak02].

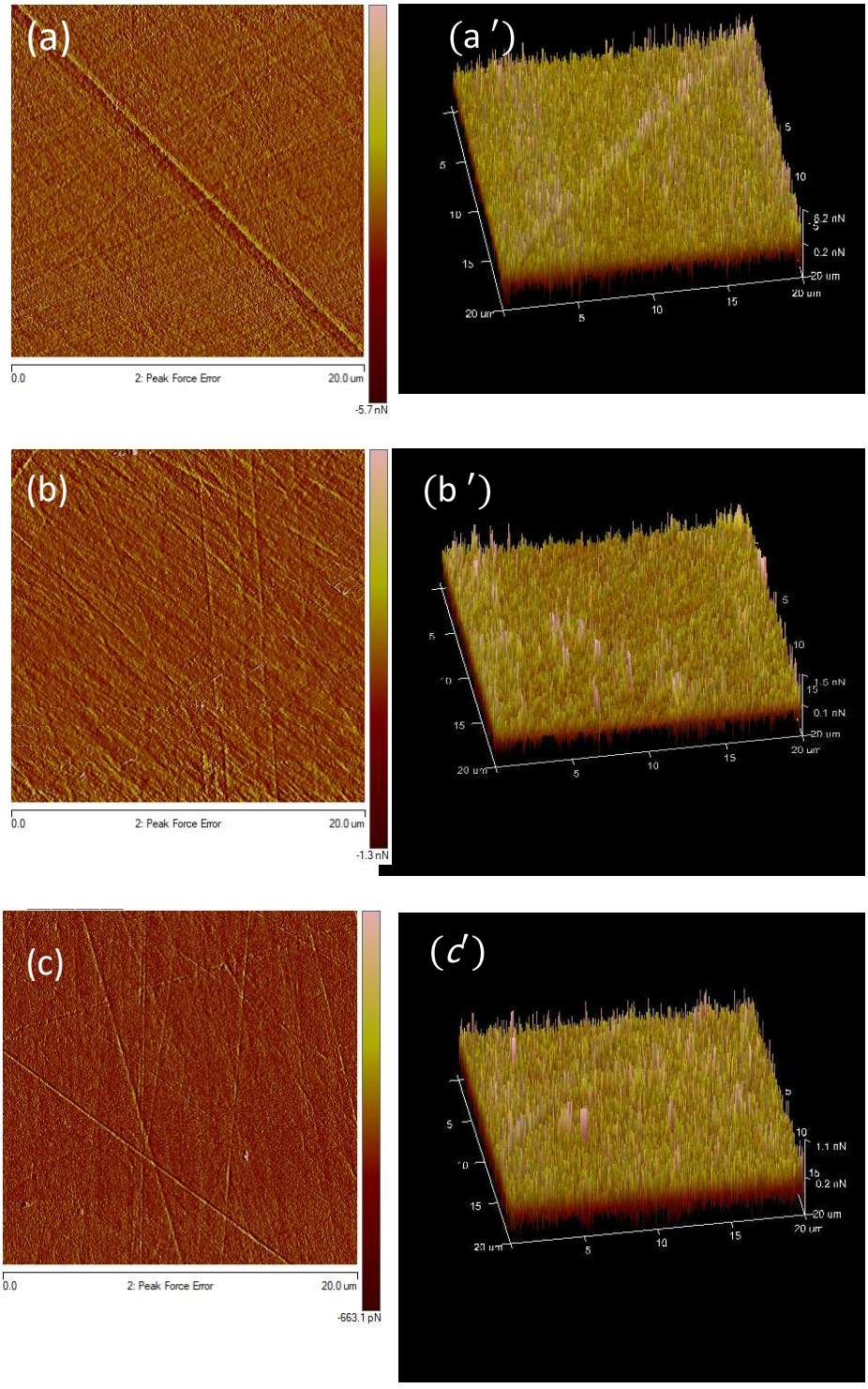

Figure 7.22:*AFM images of (a) virgin glassy carbon and after Ru implantation at (b) RT and (c) 200 ˚C. (a'), (b') and (c') are the 3D of height image.*

Figure 7.23 shows the SEM images for the virgin and as-implanted glassy carbon, which were found to be compatible with the AFM images in Figure 7.22. Figure 7.23 (a) shows virgin glassy carbon with polishing marks that become more apparent after Ru bombardment at room temperature and 200 °C (Figures 7.23 (b) and (c)). Polishing marks appear more prominent after Ru implantation due to increased sputtering of carbon atoms in the vicinity of the polishing marks. Since the surface atoms in these scratched regions have less binding energies compared to the atoms in the unscratched surface regions, they sputter more easily and expose the polishing lines [Ism18, Odu18].

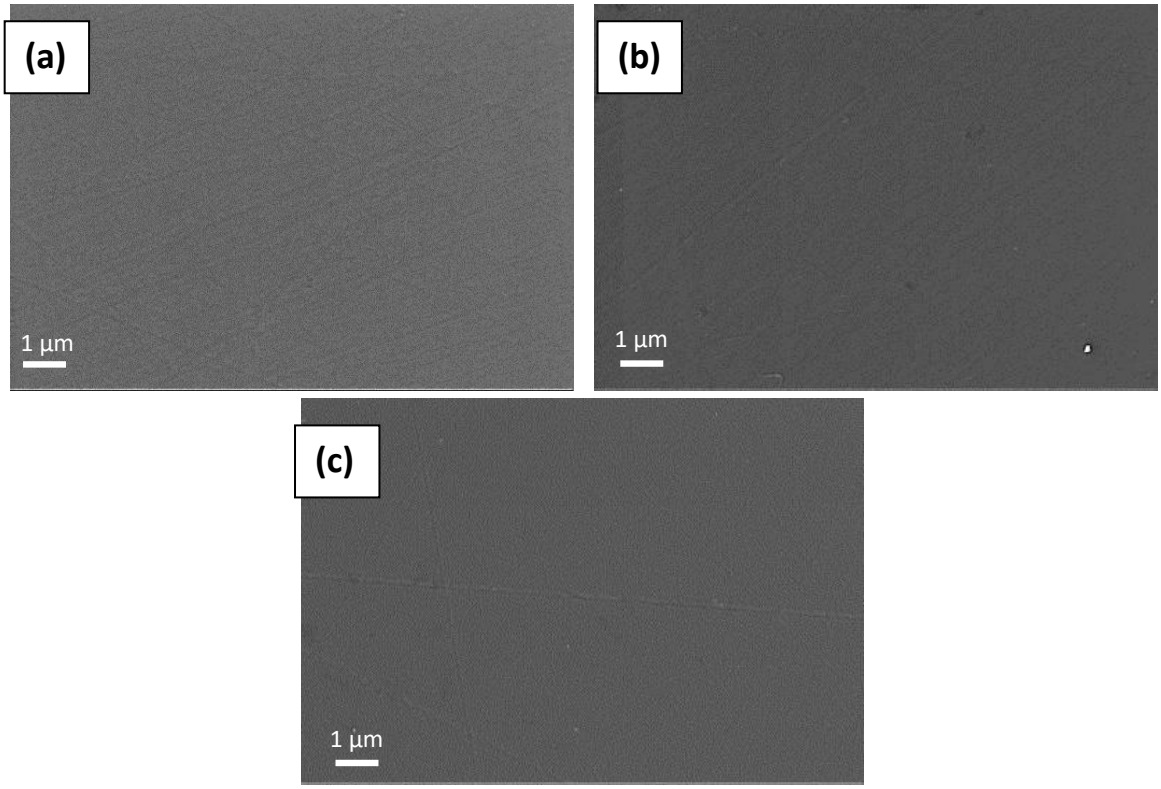

Figure 7.23: *SEM micrographs of glassy carbon obtained (a) before and after Ru implantation at (a) RT and (c) 200 ˚C.*

AFM images of the samples annealed at 1000 °C are shown in Figure 7.24. As a result of annealing at 1000°C, the surface roughness significantly increased, reaching 1.10±0.12 nm for the 200°C implanted samples and 1.15±0.12 nm for the room temperature implanted samples – see Figure 7.25. Aggregation of ruthenium atoms at 1000 °C (see Figure 7.18) can lead to the formation of some ruthenium nanoparticles in the near-surface region, thus, increasing the surface roughness of glassy carbon. Naidoo *et al.* [Nai19] found similar results,

where the implantation of Ag in amorphous carbon increased the surface roughness due to the formation of Ag nanoparticles in the near surface region.

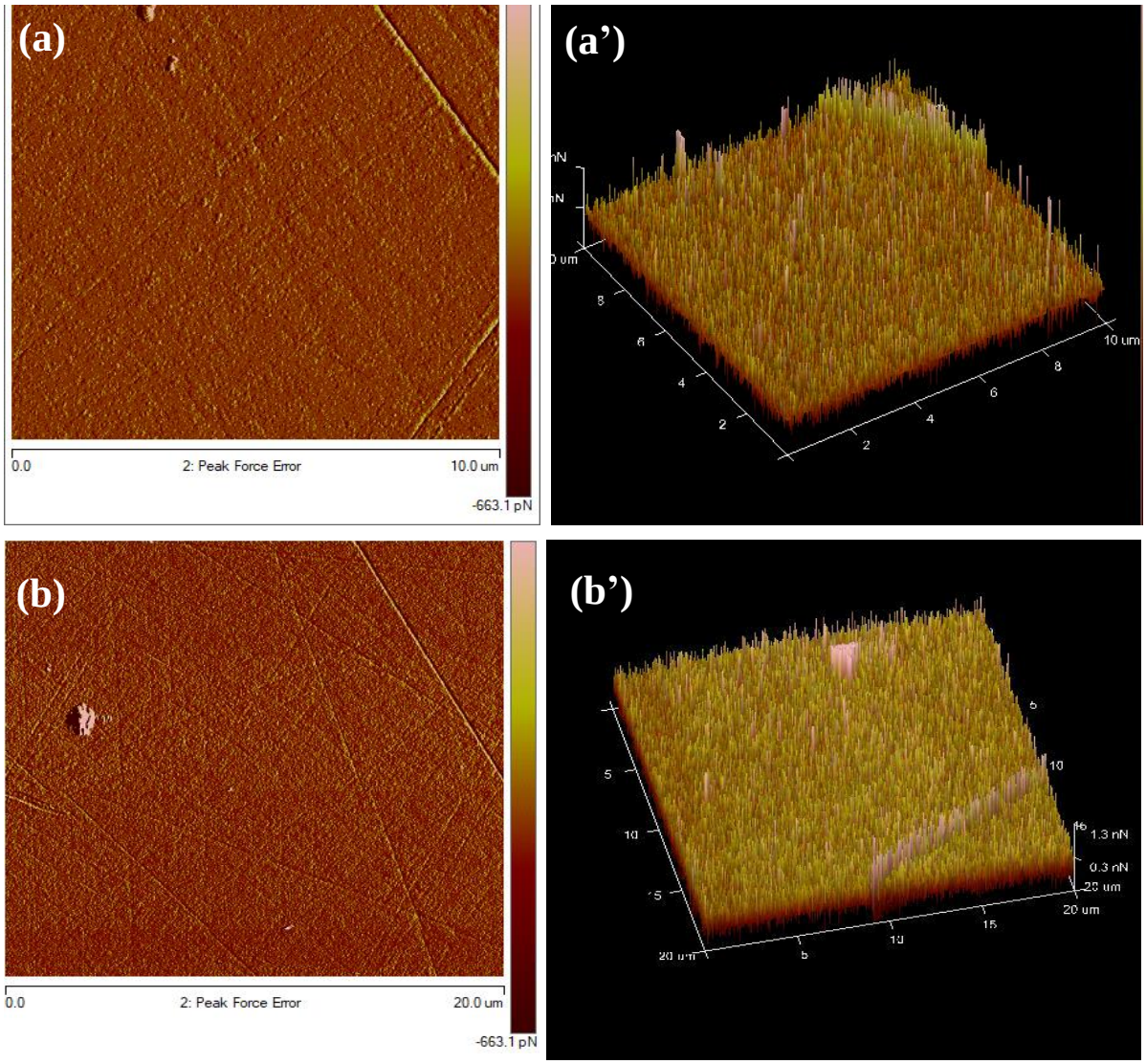

Figure 7.24: *AFM images were obtained for the (a) RT and (b) 200 °C implanted samples annealed at 1000 ˚C. (a'), (b'), (c') and (d') are the 3D of height image.*

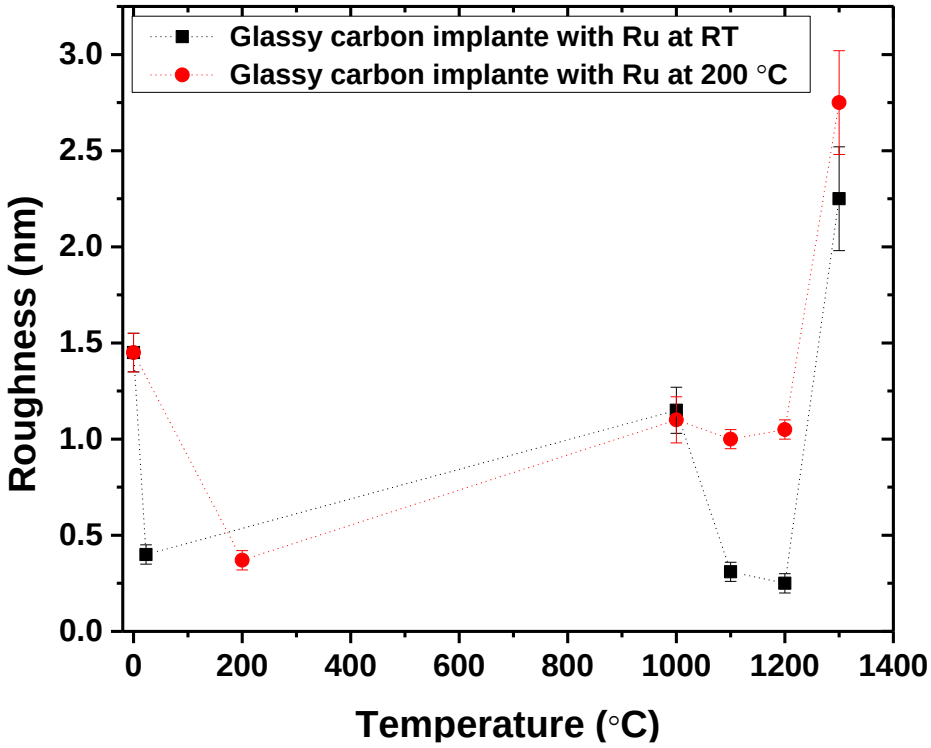

Figure 7.25: *Graph showing the effect of ruthenium bombardment at room temperature (i.e., 23 °C) and 200 °C and annealing on the surface roughness of virgin glassy carbon (value at 0 °C).*

Figures 7.26 and 7.27 show the AFM images obtained after annealing the room temperature and 200 °C implanted samples sequentially at temperatures from 1100 to 1300 °C. For room temperature implanted samples, annealing at 1100 and 1200 °C reduced surface roughness to 0.31±0.05 nm and 0.25±0.05 nm respectively – see Figure 7.25. Since there is no further aggregation or migration of Ru after annealing the room temperature implanted glassy carbon samples at 1100 and 1200 °C (see Figure 7.18 (a)), the effect of Ru migration on the surface roughness is negligible. However, annealing reduces the surface roughness (see Figure 7.25) due to the surface diffusion of the substrate atoms at the peaks of the sputter roughened surface to valley positions. Consequently, polishing marks were less pronounced after annealing as shown in AFM images in Figure 7.26 (a) and (b). However, annealing the 200 °C implanted samples at 1100 and 1200 °C resulted in no change in surface roughness. This could be due to the further shift of the depth profile toward the surface at 1100 and 1200 °C (see Figure 7.18 (b)) resulting in an increase in surface roughness, however, annealing at 1100 and

1200 °C reduces the surface roughness, which results in competing with each another and leaving the surface roughness unchanged.

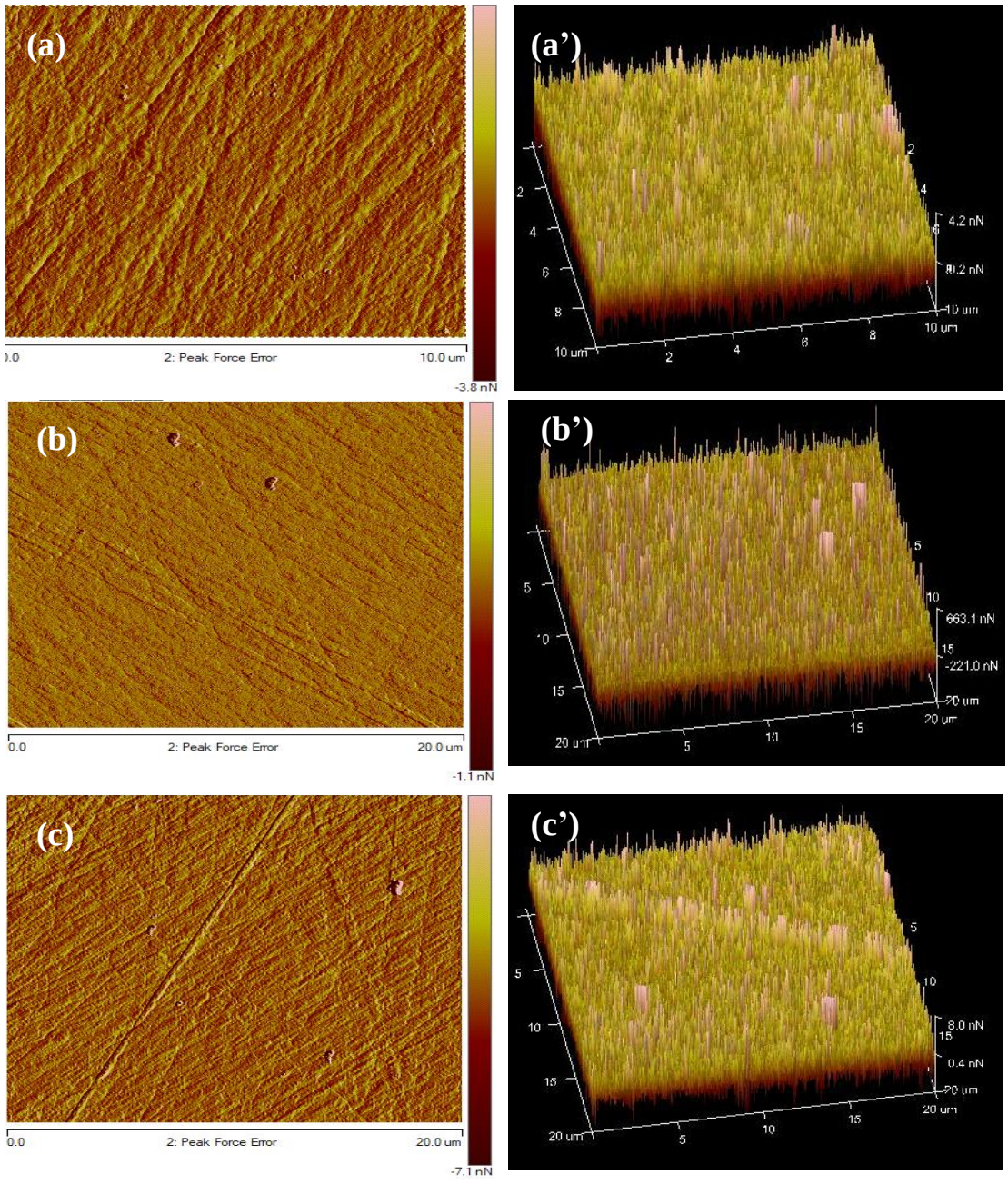

Figure 7.26: *AFM images were obtained for the RT implanted samples annealed at (a) 1100 ˚C, (b) 1200 ˚C and (c) 1300 ˚C. (a'), (b') and (c') are the 3D of height image.*

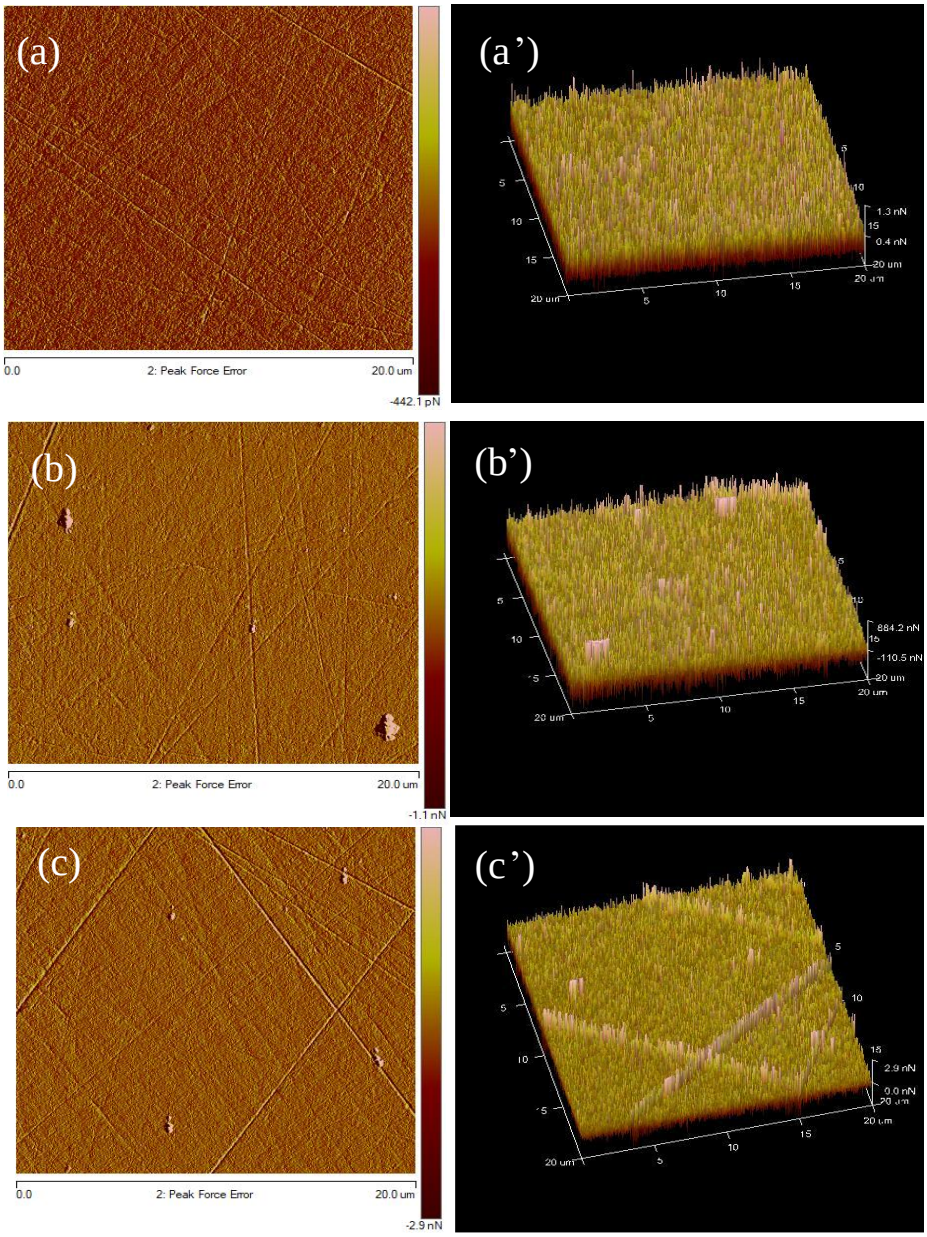

Figure 7.27: *AFM images were obtained for the 200 °C implanted samples annealed at (a) 1100 ˚C, (b) 1200 ˚C and (c) 1300 ˚C. (a'), (b') and (c') are the 3D of height image.*

It was observed that annealing at 1300 °C (see Figure 7.25) resulted in an increase in the roughness values, which became 2.25±0.27 nm for the room temperature implanted samples and 2.75±0.27 nm for the 200 °C implanted samples. An increase in roughness could be due to the large island clusters formed on the surface of glassy carbon after annealing at 1300 °C. The results obtained from SEM images after annealing from 1000 °C to 1300 °C (as shown in Figures 7.28 and 7.29) confirmed these findings where the grains became larger and the surface

became rougher at 1300 °C, compared to the samples annealed at 1000 °C. As the annealing temperature increased, the quantity of these clusters increased. This could be attributed to the aggregation of surface granules into large clusters at high temperatures. Surface morphology was observed to be affected by cluster size, namely, as cluster size and the number of clusters increased, the surface appeared rougher. The increase in cluster size was also accompanied by a reappearance of polishing marks, especially in the 200 °C implanted samples that exhibit higher roughness than the room temperature implanted samples annealed under the same conditions. This could be due to Ru migrating toward the surface in the 200 °C implanted samples annealed at 1300 °C, while no noticeable Ru migration was observed in the room temperature implanted samples - see Figure 7.18. It can be deduced that the physical appearance of the surface topography is greatly dependent on heat treatment or the migration and aggregation of implanted Ru.

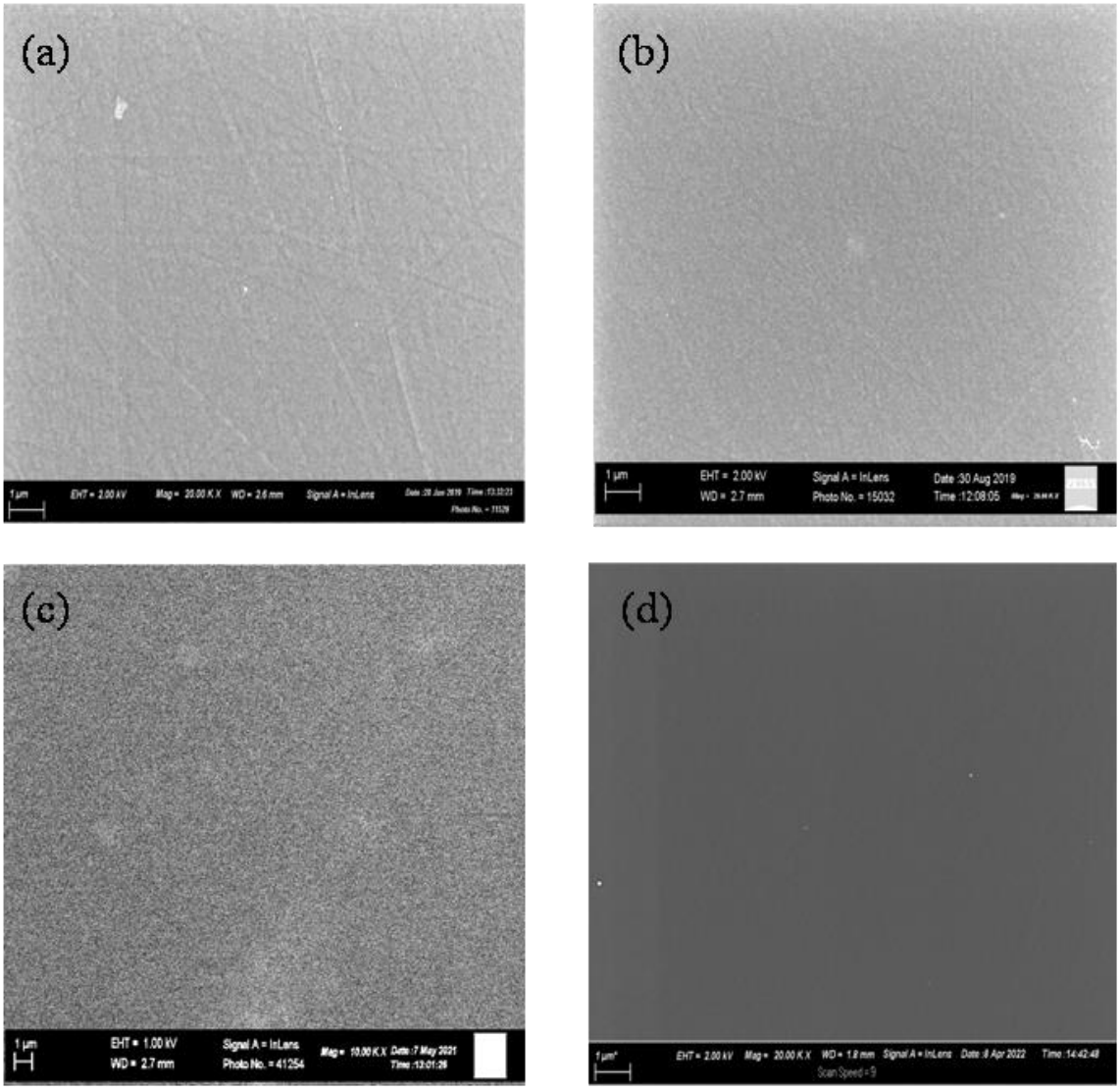

Figure 7.28: *SEM micrographs of Ru implanted into glassy carbon at RT and annealed at (a) 1000 ˚C, (b) 1100 ˚C, (c) 1200 ˚C and (d) 1300 ˚C.*

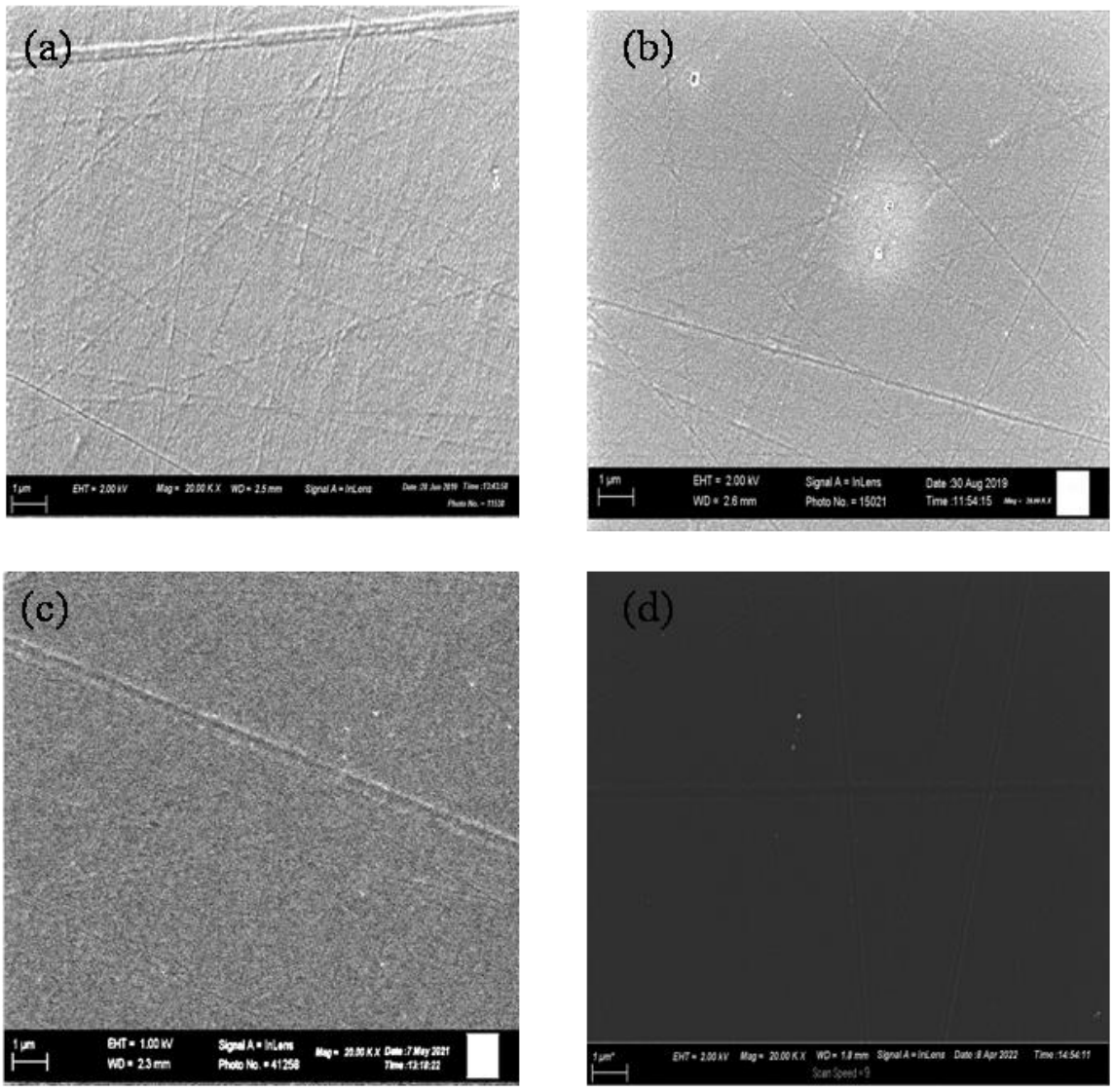

Figure 7.29: *SEM micrographs of ruthenium implanted into glassy carbon at 200 ˚C and annealed at (a) 1000 ˚C, (b) 1100 ˚C, (c) 1200 ˚C and (d) 1300 ˚C.*

All the results above indicate that the observed strain in the annealed glassy carbon samples, as revealed by Raman and XRD analyses, prompted Ru migration towards the glassy carbon surface. Additionally, the strain induced Ru segregation at the interface between the glassy carbon and the bombardment-induced amorphous region, at a depth of 150 nm below

the surface. In contrast, the high aggregation of Ru in room temperature implanted samples hindered Ru migration. RBS, AFM, and SEM results revealed that Ru migration and aggregation contributed to an increase in surface roughness, attributed to the formation of Ru nanoparticles in the near-surface region. In summary, the strain in the glassy carbon samples played a pivotal role in directing Ru migration towards the glassy carbon surface, thereby resulting in increased surface roughness.

References

[Ade20] S.A. Adeojo, J.B. Malherbe, E.G. Njoroge, M. Mlambo, O.S. Odutemowo, T.T. Thabethe, Z.A.Y. Abdalla, T.T. Hlatshwayo, *Effect of sequential isochronal annealing on the structure and migration behaviour of selenium-ion implanted in glassy carbon*, Vacuum 182 (2020) 109689.

[Ade22] S. Adeojo, J. Malherbe, A. Azarov, O. Odutemowo, E. Njoroge, H. Abdelbagi, S. Mpelane, T. Hlatshwayo, *Effects of implantation temperature and annealing on structural evolution and migration of Se into glassy carbon*, Solid State Sci. 129 (2022) 106914.

[Arn77] G.W. Arnold, J.A. Borders, *Aggregation and migration of ion implanted silver in lithia-alumina-silica Glass*, J. Appl. Phys. 48 (1977) 1488–1496.

[Bar95] A.L. Barabasi, H.E. Stanley (Eds.), *Fractal Concepts in Surface Growth*, Cambridge University Press, 1995.

[Cha11] Y.Y. Chang, Y.N. Shieh, H.Y. Kao, *Optical properties of TiO_2 thin films after Ag ion implantation*, Thin Solid Films 519 (2011) 6935–6939.

[Fer00] A.C. Ferrari, J. Robertson, *Interpretation of Raman spectra of disordered and amorphous carbon*, Physical Review B 61 (2000) 14095 – 14107.

[Ism18] M.Y.A. Ismail, J.B. Malherbe, O.S. Odutemowo, E.G. Njoroge, T.T. Hlatshwayo, M. Mlambo, E. Wendler, *Investigating the effect of heat treatment on the diffusion behaviour of xenon implanted in glassy carbon*, Vacuum 149 (2018) 74–78.

[Ism21] M.Y.A. Ismail, Z.A.Y. Abdalla, E.G. Njoroge, O.S. Odutemowo, T.T. Hlatshwayo, *Effect of high temperature annealing and SHI irradiation on the migration behaviour of Xe implanted into glassy carbon*, Nucl. Instrum. Methods Phys. Res. B. 489 (2021) 11–19.

[Ism19] M.Y.A. Ismail, *The migration behaviour of xenon implanted into glassy carbon*. Diss. University of Pretoria, 2019.

[Jaf23] T.A.O. Jafer, T.T. Thabethe, O.S. Odutemowo, S.A. Adeojo, H.A.A. Abdelbagi, A. Azarov, J.B. Malherbe, *Ruthenium ion modification of glassy carbon: Implication on the*

structural evolution and migration behaviour of implanted Ru atoms, Nucl. Instr. Methods. Phys. Res. B 534 (2023) 72-80.

[Jan07] G.C.A.M. Janssen, *Stress and strain in polycrystalline thin films, Stress and strain in polycrystalline thin films*, Thin solid films. 515 (2007) 6654–6664.

[Jue90] J.F. Jue, A.V. Virkar, Fabrication, *Microstructural Characterization, and Mechanical Properties of Polycrystalline t'-Zirconia*, J. Am. Ceram. SOC. 73 (1990) 3650–3657.

[Kax03] E. Kaxiras (Ed.), *Atomic and Electronic Structure of Solids*, Cambridge University Press, 2003.

[Khm13] R.A. Khmelnitsky, V.A. Dravin, A.A. Tal, M.I. Latushko, A.A. Khomich, A.V. Khomich, A.S. Trushina, A.A. Alekseev, S.A. Terentiev, *Mechanical stresses and amorphization of ion-implanted diamond*, Nucl. Instrum. Meth. Phys. Res. B 304 (2013) 5–10.

[Koz73] V.N. Kozyrenko, I.D. Mikhailov, *The effect of the impurity cluster on the vibrational spectrum of a one-dimensional crystal*, physica status solidi (b) 59 (1973) 13-16.

[Len37] J.E. Lennard-Jones, *The migration and aggregation of atoms on solid surfaces*, Proc. Phys. Soc. 49 (1937) 140–150.

[Mak02] M.A. Makeev, R. Cuerno, A.L. Barabasi, *Morphology of ion sputtered surfaces*, Nucl. Instr. and Meth. in Phys. Res. B 197 (3-4) (2002) 185–227.

[Mio01] A. Miotello, G.D. Marchi, G. Mattei, P. Mazzoldi, C. Sada, *Clustering of gold atoms in ion-implanted silica after thermal annealing in different atmospheres*, Phys. Rev. B 63 (2001), 075409.

[Mal13] J.B. Malherbe, *Diffusion of fission products and radiation damage in SiC*, Journal of Physics D: Applied Physics, 46 (2013) 473001.

[Mal17] J.B. Malherbe, P.A. Selyshchev, O.S. Odutemowo, C.C. Theron, E.G. Njoroge, D.F. Langa, T.T. Hlatshwayo, *Diffusion of a mono-energetic implanted species with a Gaussian profile*, Nucl. Instrum. Meth. Phys. Res. B 406 (2017) 708 – 713.

[Mal18] J. B. Malherbe, O.S. Odutemowo, E. G. Njoroge, D.F. Langa, T.T. Hlatshwayo, C.C. Theron, *Ion bombardment of glassy carbon*, Vacuum 149 (2018) 19 – 22.

[Man19] S. Manavalan, P. Veerakumar, S. Chen, K. Murugan, K. Lin, *Binder-free modification of a glassy carbon electrode by using porous carbon for voltammetric determination of Nitro Isomers*, ACS Omega 4 (2019) 8907–8918.

[McC94] D.G. McCulloch, S. Prawer, A. Hoffman, *Structural investigation of xenon-ion-beam-irradiated glassy carbon*, Physical Review B 50 (1994) 5905 – 5917.

[McC95] D.G. McCulloch, S. Prawer, *The effect of annealing and implantation temperature on the structure of C ion beam irradiated glassy carbon*, J. Appl. Phys. 78 (1995) 3040–3047.

[McC95'] D.G. McCulloch, R. Mc Kenzie, S. Prawer, *Compressive stress induced formation of preferred orientation in glassy carbon following high-dose C^+ implantation*, Philos. Mag. A 72 (4) (1995) 1031–1041.

[Mor06] R.B. More, J.C. Bokros, *Biomaterials: carbon*, Encyclopedia of medical devices and instrumentation (2006).

[Nai19] S.R. Naidoo, A. Ismaila, *Fluence enhanced optical response of Ag implanted amorphous carbon thin films*, C. 5 (2019) 45.

[Nan04] NanoScope Command Reference Manual (2004) Digital Instruments, Version 6.13.

[Njo17] E.G. Njoroge, L.D. Sebitla, C.C. Theron, M. Mlambo, T.T. Hlatshwayo, O.S. Odutemowo, V.A. Skuratov, E. Wendler, J.B. Malherbe, *Structural modification of indium implanted glassy carbon by thermal annealing and SHI irradiation*, Vacuum 144 (2017) 63–71.

[Njo21] E.G. Njoroge, T.T. Hlatshwayo, M. Mlambo, O. Odutemowo, K.A. Annan, A. Skuratov, M. Ismail, J.B. Malherbe, *Effect of thermal annealing on SHI irradiated indium implanted glassy carbon*, Nucl. Instrum. Methods Phys. Res. B. 502 (2021) 66–72.

[Niw95] K. Niwase, *Irradiation-induced amorphization of graphite*, Phys. Rev. B 52 (1995) 15785–15798.

[Nse14] S. Nsengiyumva, A.T. Raji, J.P. Riviere, D.T. Britton, M. Harting, *Stress enhanced diffusion of krypton ions in polycrystalline titanium*, Journal of Applied Physics, 116 (2014) 023513.

[Odu16] O.S. Odutemowo, J.B. Malherbe, L. Prinsloo, D.F. Langa, E. Wendler, *High temperature annealing studies of strontium ion implanted glassy carbon*, Nucl. Instrum. Methods Phys. Res. B. 371 (2016) 332–335.

[Odu18] O.S. Odutemowo, J.B. Malherbe, L.C. Prinsloo, E.G. Njoroge, R. Erasmus, E. Wendler, A. Undisz, M. Rettenmayr, *Structural and surface changes in glassy carbon due to strontium implantation and heat treatment*, J. Nucl. Mater. 498 (2018) 103–116.

[Orl21] A. Orlando, F. Franceschini, C. Muscas, S. Pidkova, M. Bartoli, M. Rovere, A. Tagliaferro, *A comprehensive review on Raman spectroscopy applications*, Chemosensors 9 (2021) 262.

[Pra20] A.D. Prasetya, M. Rifai, Mujamilah, H. Miyamoto, *X-ray diffraction (XRD) profile analysis of pure ECAP-annealing Nickel samples*, J. Phys.: Conf. Ser. 1436 (2020) 012113.

[Ram09] A.A. Ramadan, A.A. Abd El-Mongy, A.M. El-Shabiny, A.T. Mater, S.H. Mostafa, E. A. El-Sheheedy, H.M. Hashem, *Addressing difficulties in using XRD intensity for structural study of thin films*, Crystal Res. Technol. J. Experiment. Indust. Crystallogr. 44 (2009) 111–116.

[Res14] V. Resta, G. Quarta, L. Maruccio, L. Calcagnile, *Copper ion implantation of polycarbonate matrices: Morphological and structural properties*, Nucl. Instrum. Meth. Phys. Res. B 331 (2014) 187–190.

[Sil03] S.R.P. Silva, *Properties of Amorphous Carbon*, INSPEC, London, UK, 2003.

[Sla64] J.C. Slater, *Atomic radii in crystals*, J. Chem. Phys. 41 (1964) 3199–3204.

[Usk21] V. Uskokovic, *A historical review of glassy carbon: Synthesis, structure, properties and applications*, Carbon Trends 5 (2021) 100116.

[Wag22] M. Wagner, M. Mayer, U. von Toussaint, A. Mutzke, A, Simulation of the evolution of rough surfaces by sputtering using the binary collision approximation, Radiation Effects and Defects in Solids, 177 (2022) 1019-1032.

[Wen12] E. Wendler, T. Bierschenk, F. Felgentrager, J. Sommerfeld, W. Wesch, D. Alber, G. Bukalis, L.C. Prinsloo, N. van der Berg, E. Friedland, J.B. Malherbe, *Damage formation and optical absorption in neutron irradiated SiC*, Nucl. Instrum. Methods Phys. Res. B 286 (2012) 97–101.

[Wil53] G.K. Williamson, W.H. Hall, *X-ray line broadening from filed aluminium and wolfram*, Acta metallurgica. 1 (1953) 22-31.

[Wod93] R.A. Wood, P.D. Townsend, N.D. Skelland, D.E. Hole, J. Barton, C.N. Afonso, *Annealing of ion implanted silver colloids in glass*, J. Appl. Phys. 74 (1993) 5754–5756.

[Www1] https://www.sciencedirect.com/topics/medicine-and-dentistry/rutherford-backscattering-spectrometry.

[Yos88] M. Yoshikawa, G. Katagiri, H. Ishida, A. Ishitani, T. Akamatsu, *Raman spectra of diamond-like amorphous carbon films*, Journal of Applied Physics 64 (1988) 6464 – 6468.

[Zha11] Z.I. Zhang, R. Brydson, Z. Aslam, S. Reddy, A. Brown, A. Westwood, B. Rand, *Investigating the structure of non-graphitising carbons using electron energy loss spectroscopy in the transmission electron microscope*, Carbon 49 (2011) 5049–5063.

[Zie13] J.F. Ziegler, www.SRIM.org, USA, 2013.

CHAPTER 8

CONCLUSION

This study investigated the effect of implantation and annealing temperatures on the microstructure and migration behaviour of implanted Ru in glassy carbon. The purpose of this study was to determine if glassy carbon would be an effective diffusion barrier for Ru fission product. Raman spectroscopy and XRD were used to monitor the structural changes in glassy carbon after Ru ion bombardment and heat treatment. The migration behaviour of implanted Ru in glassy carbon due to annealing was investigated by RBS and SIMS. AFM and SEM were also used to investigate the surface morphology of glassy carbon due to ion bombardment and annealing. These investigations have led to the following conclusions.

8.1 Structural Changes in Glassy Carbon

The Raman results of glassy carbon samples subjected to ion implantation and subsequent annealing revealed significant insights into structural changes and stress evolution in the material. The initial Raman spectra of virgin glassy carbon exhibited characteristic D and G peaks, indicating the presence of small graphitic crystallites within the amorphous matrix. Upon Ru implantation at room temperature (RT) and 200 °C, the D and G peaks merged into a single broadband, signifying the amorphization of the graphitic crystallites. However, a narrower G peak was observed in the Raman spectrum of the 200°C-implanted samples compared to those implanted at RT, suggesting greater radiation damage in the former.

The annealing of the as-implanted samples at temperatures ranging from 500 to 1300 °C led to the partial reappearance of the characteristic D and G peaks, indicating the reduction of defects and the recrystallization of glassy carbon. At 500°C, the observed intensity of the re-grown G peak was higher than that of the D peak. However, further annealing from 600 °C to 900 °C resulted in an enhancement of D peak intensity and a reduction in G peak width. This indicates that some recovery of the glassy carbon structure increased with increasing annealing temperature. After annealing from 1000 to 1300 °C, the D and G peak intensity appears to be the same. It is noteworthy that this is in contrast to the Raman spectrum obtained for virgin

glassy carbon, which shows a more distinct D peak. This is further proof that annealing at very high temperatures (i.e., from 1000 to 1300 °C) did not completely remove all the damage (in glassy carbon) introduced by Ru ions implantation.

The FWHM value of the G peak increased from 31±2 cm^{-1} (virgin glassy carbon) to 155±2 cm^{-1} and 136±2 cm^{-1} after implantation with Ru at RT and 200 °C, respectively. This indicates that Ru implantation introduced defects in glassy carbon. The FWHM of the G peak revealed that samples implanted at RT had more defects than those implanted at 200 °C, while annealing reduced these defects in all samples (implanted at RT and 200 °C). However, samples implanted at RT still contained higher defects than samples implanted at 200 °C that were annealed under the same conditions. This is due to the initial amount of defects in glassy carbon introduced by the ion implantation process (where implantation at RT caused more radiation damage/defects than those implanted at 200 °C). Moreover, even at the highest annealing temperature of 1300 °C, the FWHM remained wider than that of virgin glassy carbon, indicating that complete recovery had not been achieved.

The shift in the G peak position provided insight into the residual stress within the glassy carbon material. After Ru ion bombardment, the G peak position of virgin glassy carbon shifted to a lower wavenumber indicating tensile stress. Annealing the as-implanted samples from 500 to 900 °C showed a significant shift of the G peak towards the higher wavenumber, but did not exceed the position of the G peak of virgin glassy carbon. This indicates the reduction of tensile stress in glassy carbon after annealing up to 900 °C. However, annealing at temperatures higher than 900 °C (from 1000 to 1300 °C) showed an increased shift of the G peak towards a wavenumber higher than the position of the G peak of virgin glassy carbon indicating compressive stress. This difference in stress between as-implanted and annealed samples from 500 to 900 °C and from 1000 to 1300 °C was attributed to differences in glassy carbon density.

XRD was used to investigate the effect of ruthenium ion bombardment and heat treatment on the glassy carbon structure. The internal strain of virgin, as-implanted and annealed glassy carbon was estimated from XRD patterns using the William-Hall equation. The strain in virgin glassy carbon increased from 4.5×10^{-4} to 0.002 and 0.0054 after Ru implantation at 200 °C and RT, respectively. This indicates that implantation of Ru in glassy carbon produces tensile strain. However, annealing the as-implanted samples from 1000 °C to 1300 °C showed a negative sign for the strain values, which indicates compressive strain. This is in good agreement with Raman results, where the G peak position of virgin glassy carbon shifted to a

lower wavenumber after implantation, indicating the presence of tensile stress. However, the G peaks shift to a higher wavenumber after annealing from 1000 to 1300 °C, which indicates the presence of compressive stress.

8.2 Ru Migration in Glassy Carbon

RBS and SIMS were used to monitor the migration behavior of Ru in glassy carbon after annealing at low (from 500 to 1000 °C) and high (from 1000 to 1300 °C) temperatures. Annealing at temperatures from 500 to 800 °C did not significantly alter the Ru depth profiles, indicating that Ru does not diffuse in glassy carbon at these temperatures. However, annealing at 900 °C and 1000 °C caused notable changes in the Ru depth profiles, with increased aggregation of Ru atoms and a shift of the depth profiles toward the surface. This aggregation occurred due to strong cohesive forces between Ru atoms. Moreover, RT implanted samples exhibited more Ru aggregation than the 200 °C implanted samples when annealed at 900 °C and 1000 °C. This is attributed to the higher concentration of defects in RT implanted samples, which facilitate Ru aggregation. The aggregation was accompanied by a shift of the whole depth profile towards the glassy carbon surface. This was due to the stress field that caused the profile to migrate as a whole. However, the shift of Ru depth profiles toward the surface was less pronounced in the RT implanted samples compared to 200 °C implanted samples, possibly due to the larger Ru clusters formed in these samples, hindering migration toward the surface.

At higher temperatures (from 1000 to 1300 °C), Ru aggregation was clearly observed and accompanied by peak shifts toward the surface. Since Ru atoms aggregate in glassy carbon at temperatures over 800 °C, this was expected. At 1300 °C, Ru atoms tended to segregate at the interface between the glassy carbon and the bombardment-induced amorphous region (i.e., at a depth of 150 nm below the surface) which was due to atom size differences and stress fields. Moreover, remarkably, neither low-temperature nor high-temperature annealing led to significant loss of the implanted Ru from the glassy carbon. This was attributed to the formation of Ru clusters within the material, preventing the outward diffusion of Ru atoms. Therefore, glassy carbon material would be a good storage container for Ru.

8.3 Surface Topography and Roughness

SEM and AFM analyses were used to investigate changes in the surface topography and roughness of the glassy carbon substrate after Ru implantation and heat treatment. The initial R_q (root mean square roughness) of pristine glassy carbon was measured at 1.45±0.1 nm. After Ru implantation at room temperature and 200 °C, R_q surface roughness decreased to 0.40±0.05 nm and 0.37±0.05 nm, respectively. The decrease in surface roughness after Ru implantation was expected, as it is a common effect of ion bombardment.

Annealing at 1000 °C led to an increase in R_q surface roughness, reaching 1.10±0.12 nm for the 200 °C implanted samples and 1.15±0.12 nm for the RT implanted samples. This was due to the aggregation of ruthenium atoms forming nanoparticles near the surface region. Further annealing of the RT implanted samples at 1100 and 1200 °C resulted in reduced surface roughness, measuring 0.31±0.05 nm and 0.25±0.05 nm, respectively. This was attributed to the surface diffusion of the substrate atoms (from the peaks of the sputter roughened surface to valley positions in the surface) which reduced the surface roughness. However, annealing the 200 °C implanted samples under the same conditions showed no change in surface roughness. This was due to the further shift of the depth profile toward the surface at 1100 and 1200 °C resulting in an increase in surface roughness, however, annealing at these temperatures reduces the surface roughness, which results in competing with each another and leaving the surface roughness unchanged. Moreover, annealing at 1300 °C increased the surface roughness, reaching 2.25±0.27 nm for the RT implanted samples and 2.75±0.27 nm for the 200 °C implanted samples, due to the formation of large carbon clusters on the glassy carbon surface.

Therefore, from the above, Ru implantation effectively reduces surface roughness (i.e., R_q values) in glassy carbon, with consistent results at different implantation temperatures. Annealing at 1000 °C leads to increased roughness due to Ru aggregation, while higher-temperature annealing has varying effects, influenced by factors such as surface diffusion, cluster formation and Ru migration.

In summary, this study thoroughly investigated the impact of implantation and annealing temperatures on the microstructure and migration behaviour of Ru implanted in glassy carbon, with a focus on assessing its suitability as a diffusion barrier for Ru fission products. Raman and XRD results revealed amorphization of glassy carbon and structural changes induced by ion bombardment and subsequent annealing, showcasing the transition from tensile to

compressive stress. RBS and SIMS elucidated Ru migration, with notable aggregation and segregation at higher annealing temperatures. Remarkably, both low and high-temperature annealing did not lead to significant Ru loss, affirming glassy carbon's efficacy as a storage container for Ru. Surface analyses through SEM and AFM showed a reduction in roughness post-implantation, while annealing-induced variations in roughness were linked to Ru migration or aggregation, surface diffusion and cluster formation. This comprehensive investigation provides valuable insights into Ru migration in glassy carbon, laying the foundation for its potential application as an effective diffusion barrier for Ru fission products.

8.4 Future Work

In this study, we discovered that Ru atoms tend to aggregate and create clusters within the glassy carbon matrix. However, considering the practical application of glassy carbon as a container for spent nuclear fuel, it would be exposed to a range of fission products in addition to Ru. Understanding the effects of these diverse fission products on the migration behavior of Ru within the glassy carbon is a critical area for further exploration. Therefore, as part of the prospective research, we propose co-implanting Ru ions alongside other fission product into the glassy carbon substrate, followed by controlled annealing processes. This investigation will shed light on the complex dynamics of Ru migration in the presence of various fission products, providing valuable insights into the behaviour of glassy carbon as a nuclear waste containment material under realistic conditions.

Another suggestive study is to critically examine the migration behaviour of palladium in glassy carbon. Palladium is a highly reactive fission product element, therefore, the diffusion and reaction of palladium with glassy carbon must be investigated.

CHAPTER 9

RESEARCH OUTPUTS

The work presented in this thesis has contributed to one publication and one conference presentation. A summary of the outputs is presented below:

9.1 PUBLICATIONS IN PEER- REVIEWED JOURNALS.

[1] T.A.O. Jafer, T.T. Thabethe, O.S. Odutemowo, S.A. Adeojo, H.A.A. Abdelbagi, A. Azarov, J.B. Malherbe, Ruthenium ion modification of glassy carbon: implication on the structural evolution and migration behaviour of implanted Ru atoms. Nucl. Instrum. Methods Phys. Res. B. 534 (2023) 72-80.

[2] T.A.O. Jafer, T.T. Thabethe, O.S. Odutemowo, S.A. Adeojo, H.A.A. Abdelbagi, J.B. Malherbe, The effect of ion implantation and annealing temperatures on the migration behaviour of ruthenium in glassy carbon. In preparation.

9.2 CONFERENCE PRESENTATION

i. 14th International Particle Accelerator Conference that was held in Venice, Italy in 2023 (Poster presentation).